THE UNIVERSITY OF QUEENSLAND

AUSTRALIA

Designer Mesoporous Silica Nano-carriers for Hydrophobic Drug Delivery with Enhanced Bioavailability

Siddharth D Jambhrunkar

A thesis submitted for the degree of Doctor of Philosophy at

The University of Queensland in 2014

Australian Institute for Bioengineering and Nanotechnology

Abstract

Since the discovery of mesoporous silica nanoparticles (MSNs) by Mobil's researchers in 1992, it has aroused keen interest for its application in catalysis, adsorbent, and many more owing to its structural characteristics of high surface area, possibility of surface functionalization and adjustable pore size. It was in the last decade when MSNs were first reported for its application in drug delivery and since then researchers are exploring possibilities of MSNs to resolve the challenges in the pharmaceutical sector.

More than 40% of pharmaceutical drug candidates emerging from high throughput screening process are hydrophobic possessing low aqueous solubility and hence low bioavailability. These drug molecules are highly potent but, cannot be formulated as an effective formulation owing to its low aqueous solubility which hinders its clinical application. This raises a huge challenge for pharmaceutical scientists to enhance the aqueous solubility of hydrophobic drugs. Reducing the drug particle size can enhance the solubility according to the Ostwald–Freundlich equation. However, it has been difficult to downsize the drug particle below 20 nm with the existing technologies, a regime in which a dramatic increase in solubility is expected.

This research work seeks to overcome the limitations by enhancing aqueous solubility of hydrophobic drug molecules using MSNs. A simple and novel method have been developed wherein the pore size of MSNs can be systematically adjusted in a stepwise manner at step precision of angstrom scale to obtain a series of MSNs with controllable pore size (1-10 nm). By loading drug molecules inside the pores of MSNs, the drug particle sizes can be confined to the pore size. We hypothesize that, there exists an optimized pore size for a given hydrophobic drug molecule which would display highest solubility. We successfully demonstrated that there exists an optimized MSN pore size displaying highest aqueous solubility by studying pore size – solubility relationship for a given hydrophobic drug molecule.

In this research work, we attempted to enhance the cytotoxicity of the hydrophobic anticancer drug using MSNs as carrier system. The most preferred strategy for targeting cancer cells and enhancing anticancer drug's cytotoxicity is by designing the carrier system with positive surface charge. Positively charged carrier systems are reported to demonstrate high cellular uptake by cancer cells as cancer cells are negatively charged. However, bare positively charged carriers display toxicity, raising concern for its application.

To understand the parameters influencing the cellular uptake of MSNs in enhancing the anticancer drug's cytotoxicity, we synthesized MSNs with different surface functionalities. Surface functionalization was performed on MSNs to study the effect of surface charge and hydrophobicity by encapsulating anticancer drug in the pores of MSNs. We found that, the negatively charged MSNs have faster drug release and low cellular uptake while positively charged MSNs showed

relatively slower release and high cellular uptake. However, the anticancer activity displayed by negatively charged MSNs is similar to the positively charged MSNs. The similar anticancer activity could be attributed to the effect of cellular uptake and *in vitro* release. The hydrophobic MSNs did not enhance the anticancer activity owing to its hydrophobic surface leading to poor wetting effect. These results were further confirmed by selecting another hydrophobic drug molecule which demonstrated enhancement in drug solubility and drug release by negatively charged MSNs compared to the positively charged MSNs and hydrophobic MSNs. The findings from this work hints towards a new approach in designing carrier system for cancer treatment.

The research work in this thesis contributes to new strategies to achieve solubility enhancement for hydrophobic drugs and designing carrier system to enhance cytotoxicity of hydrophobic anticancer drugs promising their application in the pharmaceutical field.

Declaration by author

This thesis is composed of my original work, and contains no material previously published or written by another person except where due reference has been made in the text. I have clearly stated the contribution by others to jointly-authored works that I have included in my thesis.

I have clearly stated the contribution of others to my thesis as a whole, including statistical assistance, survey design, data analysis, significant technical procedures, professional editorial advice, and any other original research work used or reported in my thesis. The content of my thesis is the result of work I have carried out since the commencement of my research higher degree candidature and does not include a substantial part of work that has been submitted to qualify for the award of any other degree or diploma in any university or other tertiary institution. I have clearly stated which parts of my thesis, if any, have been submitted to qualify for another award.

I acknowledge that an electronic copy of my thesis must be lodged with the University Library and, subject to the General Award Rules of The University of Queensland, immediately made available for research and study in accordance with the *Copyright Act 1968*.

I acknowledge that copyright of all material contained in my thesis resides with the copyright holder(s) of that material. Where appropriate I have obtained copyright permission from the copyright holder to reproduce material in this thesis.

Publications during candidature

Journal Publications Relevant to Thesis

1. **Siddharth Jambhrunkar**, Meihua Yu, Jie Yang, Jun Zhang, Abhijit Shrotri, Liliana Endo-Munoz, Joël Moreau, Gaoqing Lu and Chengzhong Yu. *Stepwise Pore Size Reduction of Ordered Nanoporous Silica Materials at Angstrom Precision*. ***Journal of the American Chemical Society, 2013,*** 135, 8444-8447.
2. **Siddharth Jambhrunkar**[†], Surajit Karmakar[†], Amirali Popat, Meihua Yu and Chengzhong Yu. *Mesoporous Silica Nanoparticles Enhance the Cytotoxicity of Curcumin*. ***RSC Advances, 2014,*** 4(2), 709-712.
3. **Siddharth Jambhrunkar**, Zhi Qu, Amirali Popat, Jie Yang, Owen Noonan, Luiz Acauan, Yusilawati Ahmad Nor, Chengzhong Yu , Surajit Karmakar. *Effect of Surface Functionality of Silica Nanoparticles on Cellular Uptake and Cytotoxicity*. ***Molecular Pharmaceutics, 2014,*** 11(10), 3642-3655.
4. **Siddharth Jambhrunkar**, Zhi Qu, Amirali Popat, Surajit Karmakar, Chun Xu, Chengzhong Yu. *Modulating in vitro Release and Solubility of Griseofulvin Using Functionalised Mesoporous Silica Nanoparticles*. Submitted to ***Journal of Colloid and Interface Science, 2014***, 434, 218-225.

Additional Journal Publication

1. Meihua Yu, **Siddharth Jambhrunkar**, Peter Thorn, Jiezhong Chen, Wenyi Gu and Chengzhong Yu. *Hyaluronic acid modified mesoporous silica nanoparticles for targeted drug delivery to CD44-overexpressing cancer cells*. ***Nanoscale, 2013***, 5 (1), 178-183.
2. Amirali Popat, Benjamin P. Ross, Jian Liu, **Siddharth Jambhrunkar**, Freddy Kleitz, and Shi Zhang Qiao. *Enzyme-Responsive Controlled Release of Covalently Bound Prodrug from Functional Mesoporous Silica Nanospheres*. ***Angewandte Chemie International Edition, 2012***, 51 (50), 12486–12489.
3. Kun Qian, Fang Liu, Jie Yang, Xiaodan Huang, Wenyi Gu, **Siddharth Jambhrunkar**, Pei Yuan and Chengzhong Yu. *Pore size-optimized periodic mesoporous organosilicas for the enrichment of peptides and polymers*. ***RSC Advances***, ***2013,*** *3, 14466-14472*
4. Chun Xu, Yuting Niu, **Siddharth Jambhrunkar**, Surajit Karmakar, Amirali Popat and Chengzhong Yu. *Rod-like Mesoporous Silica Nanoparticles with Rough Surfaces for Enhanced Cellular Delivery*. ***Journal of Material Chemistry B, 2014,*** 2, 253-256.

5. Chang Lei, Owen Noonan, **Siddharth Jambhrunkar**, Kun Qian, Chun Xu, Jun Zhang, Amanda Nouwens and Chengzhong Yu. *Sensitive Detection of Human Insulin using a Designed Combo-Pore Approach*, **Small, 2014**, 10 (12), 2413-18.
6. Amirali Popat, **Siddharth Jambhrunkar**, Jun Zhang, Jie Yang,Honwei Zhang, Anand Meka and Chengzhong Yu. *Programmable Drug Release using Bioresponsive Mesoporous Silica Nanoparticles for Site-specific Oral Drug Delivery*. ***Chemical Communications, 2014***, 50, 5547-50.
7. Amirali Popat[†], Surajit Karmakar[†], **Siddharth Jambhrunkar**, Chun Xu, Chengzhong Yu. *Curcumin-cyclodextrin Encapsulated Chitosan Nanoconjugates with Enhanced Solubility and Cell Cytotoxicity*. ***Colloids and Surfaces B: Biointerface, 2014,*** 117, 520-7.
8. Prasanna Abbaraju, **Siddharth Jambhrunkar**, Anand Meka, Jun Zhang, Chun Xu, Amirali Popat and Chengzhong Yu. *Floating tablets from mesoporous silica nanoparticles.* ***Journal of Material Chemistry B, 2014*** *(in press).*
9. Meihua Yu, Yuting Niu, Jun Zhang, Elena Taran, **Siddharth Jambhrunkar**, Wenyi Gu, Peter Thorn and Chengzhong Yu. *An Unusual Size-dependent Gene Delivery Relationship of Monodispersed Silica Nanoparticles*. ***ACS Nano, 2014*** (*submitted*).
10. Chun Xiang (Cynthia) Lin, **Siddharth Jambhrunkar**, Pei Yuan, Xiu Song Zhao. *Multi-compartment Mesoporous Organosilicas for Drug Storage and Release*. ***Angewandte Chemie International Edition, 2014*** (*submitted*).

Conference Presentation and poster

1. **Siddharth Jambhrunkar**, Surajit Karmakar, Amirali Popat, Zhi Qu, Jie Yang, Owen Noonan, Luiz Acauan, Yusilawati Ahmad Nor, Chengzhong Yu. Oral presentation on "*Influence of Surface Functionality of Silica Nanoparticles on Cytotoxicity and Cell Uptake*" NanoBio conference, July 2014, Brisbane, Australia.
2. **Siddharth Jambhrunkar**, Meihua Yu, Jie Yang, Jun Zhang, Abhijit Shrotri, Xianglan Wu, Jian Liu, Liliana Endo-Munoz, Wenyi Gu, Gaoqing Lu, Chengzhong Yu. Oral presentation on "*Precise pore size control of nanoporous materials and its application"*, UQ/UWA/Flinders Mini-Workshop, Dec. 2013, Brisbane, Australia.
3. **Siddharth Jambhrunkar**, Meihua Yu, Jie Yang, Jun Zhang, Abhijit Shrotri, Xianglan Wu, Jian Liu, Liliana Endo-Munoz, Wenyi Gu, Gaoqing Lu, Chengzhong Yu. Poster presentation on *"Stepwise pore size reduction in ordered nanoporous materials in precise range of 2-4 angstroms per step"*, 1st International Conference on BioNano Innovation (ICBNI), 18-20 July 2012, Brisbane, Australia.

Publications included in this thesis

1. **Siddharth Jambhrunkar**, Meihua Yu, Jie Yang, Jun Zhang, Abhijit Shrotri, Liliana Endo-Munoz, Joël Moreau, Gaoqing Lu and Chengzhong Yu. *Stepwise Pore Size Reduction of Ordered Nanoporous Silica Materials at Angstrom Precision*. ***Journal of the American Chemical Society, 2013,*** 135, 8444-8447 – incorporated as chapter 4.

Contributor	Statement of contribution
Siddharth Jambhrunkar	Experimental design and performance (85 %) Analysis and interpretation of data (65 %) Drafting and writing (70 %)
Meihua Yu	Drafting and writing (5 %)
Jie Yang	Analysis and interpretation of data (5 %)
Jun Zhang	Analysis and interpretation of data (10 %)
Abhijit Shrotri	Experimental design and performance (5 %) Analysis and interpretation of data (5 %)
Liliana Endo-Munoz	Drafting and writing (5 %)
Joël Moreau	Drafting and writing (5 %)
Gaoqing Lu	Drafting and writing (5 %)
Chengzhong Yu	Experimental design and performance (10 %) Analysis and interpretation of data (15 %) Drafting and writing (10 %)

2. **Siddharth Jambhrunkar**[†], Surajit Karmakar[†], Amirali Popat, Meihua Yu and Chengzhong Yu. *Mesoporous Silica Nanoparticles Enhance the Cytotoxicity of Curcumin*. ***RSC Advances, 2014,*** 4(2), 709-712 – incorporated as chapter 5.

Contributor	Statement of contribution
Siddharth Jambhrunkar	Experimental design and performance (45 %) Analysis and interpretation of data (40 %) Drafting and writing (60 %)
Surajit karmakar	Experimental design and performance (45 %) Analysis and interpretation of data (40 %) Drafting and writing (30 %)
Amirali Popat	Analysis and interpretation of data (5 %)
Meihua Yu	Analysis and interpretation of data (5 %)

Chengzhong Yu	Experimental design and performance (10 %) Analysis and interpretation of data (10 %) Drafting and writing (10 %)

3. **Siddharth Jambhrunkar**, Surajit Karmakar, Amirali Popat, Zhi Qu, Jie Yang, Owen Noonan, Luiz Acauan, Yusilawati Ahmad Nor, Chengzhong Yu. *Effect of Surface Functionality of Silica Nanoparticles on Cellular Uptake and Cytotoxicity*. ***Molecular Pharmaceutics, 2014,*** 11(10), 3642-3655 – incorporated as chapter 6.

Contributor	Statement of contribution
Siddharth Jambhrunkar	Experimental design and performance (60 %) Analysis and interpretation of data (65 %) Drafting and writing (65 %)
Surajit karmakar	Experimental design and performance (25 %) Drafting and writing (25 %)
Amirali Popat	Analysis and interpretation of data (5 %)
Zhi Qu	Experimental design and performance (10 %) Analysis and interpretation of data (5 %)
Jie Yang	Analysis and interpretation of data (5 %)
Owen Noonan	Analysis and interpretation of data (5 %)
Luiz Acauan	Analysis and interpretation of data (5 %)
Yusilawati Ahmad Nor	Drafting and writing (5 %)
Chengzhong Yu	Experimental design and performance (5 %) Analysis and interpretation of data (10 %) Drafting and writing (5 %)

5. **Siddharth Jambhrunkar**, Zhi Qu, Amirali Popat, Surajit Karmakar, Chun Xu, Chengzhong Yu. *Modulating in vitro Release and Solubility of Griseofulvin Using Functionalised Mesoporous Silica Nanoparticles*. ***Journal of Colloid and Interface Science, 2014***, 434, 218-225 – incorporated as chapter 7.

Contributor	Statement of contribution
Siddharth Jambhrunkar	Experimental design and performance (70 %) Analysis and interpretation of data (75 %) Drafting and writing (80 %)
Zhi Qu	Experimental design and performance (15 %)

Surajit karmakar	Analysis and interpretation of data (5 %) Drafting and writing (5 %)
Amirali Popat	Analysis and interpretation of data (5 %) Drafting and writing (5 %)
Chun Xu	Experimental design and performance (5 %)
Chengzhong Yu	Experimental design and performance (10 %) Analysis and interpretation of data (15 %) Drafting and writing (10 %)

Contributions by others to the thesis

"No contributions by others."

Statement of parts of the thesis submitted to qualify for the award of another degree

"None".

Acknowledgements

At this opportunity, I would like to express my sincere gratitude to Professor Chengzhong (Michael) Yu for providing me the opportunity to pursue my research interest and for his supervision, guidance, support and being my friend, philosopher in this journey. Similarly, I would like to thank my supervisors, Dr. Liliana Endo-Munoz and Dr. Wenyi Gu for their guidance and support. It would have been impossible for me to complete this thesis without their guidance and assistance.

I would like to thank ARC Centre of Excellence for Functional Materials executives, Cheryl Berquist, Celestien Warnaar-Notschaele and Chaoqing Lu for their kind assistance to make all the laboratory works going effectively. I thank Dr Ekaterina Strounina from The Centre of Magnetic Resonance for her help on NMR measurement. I thank Tony Miscamble for lending me help and advice in answering all sorts of questions relevant to postgraduate studies.

My sincere thanks goes to all my group members and colleagues in ARC Centre of Excellence for Functional Materials for their friendship and help (in no particular order): Dr. Amirali Popat, Dr. Surajit Karmakar, Dr. Liang Zhou, Abhijit Shrotri, Meihua Yu, Jun Zhang, Kun Qian, Jie Yang, Sandy Budi Hartono, Yusilawati Ahmad Nor, Yannan Yang, Anand Meka, Hongwei Zhang, Yuting Niu, Chang Lei, ChunXu, Swasmi Purwajanti, Irene Emmanuelawati, Dr. Chun Xiang Cynthia Lin, Dr. Qing Ma, Dr. Muxina Konarova and Zhi Qu.

Special thanks also go to ARC Centre of Excellence for Functional Materials and the Australian Institute for Bioengineering and Nanotechnology for providing high quality research facilities. In addition, big appreciations to the University of Queensland for providing the UQRS Scholarship and also AIBN for the generous funding which makes this research work possible.

Most of all, I thank my wife, Manasi and my son, Smit for their unending love. I wish to express my deep gratitude to my wife for her prayers, patience and encouragement throughout the whole course of my study. Finally, I would like to extend my deepest appreciation to my parents and family for their unwavering love, belief and support. Without their support, this thesis would not have been possible. To them I dedicate this PhD thesis.

Keywords

Mesoporous silica nanoparticles, pore size reduction, drug delivery, curcumin, griseofulvin, surface functionalization, hydrophobicity, cytotoxicity, cell cycle, cell apoptosis

ANZSRC code: 100708, Nanomaterials, 60%

ANZSRC code: 100709, Nanomedicine, 20%

ANZSRC code: 100712, Nanoscale Characterisation, 20%

Fields of Research (FoR) Classification

FoR code: 1007, Nanotechnology, 100%

Table of Contents

Chapter 1

Introduction

1.1 Background

The human kind has always been struggling to combat the diseases with the help of medicines. Most of the drugs used as medicines for treating these diseases have high side effects and lack patient compliance necessitating the requirement for discovery of potent, safe drug and effective drug carrier system. However, more than 40% of drugs emerging from high throughput screening process are hydrophobic and highly potent but, possess low aqueous solubility. The low aqueous solubility not only lowers the bioavailability but also hinders its clinical application. This raises a huge challenge for pharmaceutical scientists to find solution to enhance solubility of these hydrophobic drugs. Till date several strategies have been developed to address this issue which comprises of conventional and nanotechnological approaches but, with limited success. Of the strategies developed, drug particle size reduction has been proposed to be the most promising strategy based on Ostwald–Freundlich equation. However, the drug particle size cannot be reduced below 20 nm, a regime in which a dramatic increase in solubility is expected. Thus, the quest to find an appropriate method for solubility enhancement of hydrophobic drugs such as anticancer drug still persists.

Recently inorganic mesoporous silica nanoparticles (MSNs) have been proposed to address this issue owing to its structural characteristics such as high surface area, possibility of surface modification, adjustable pore size to name a few. By confining the drug molecules in the pores of MSNs with pore size 1-10 nm, the drug particle size can be reduced which would help to enhance the drug solubility. However, one needs to find an optimized pore size for a given drug to encapsulate it in the pores and achieve highest solubility. To achieve this aim, we need to find a technique which can precisely control the pore size adjustment at angstrom scale. This study was further postulated using a model hydrophobic anticancer drug molecule, Curcumin.

Cancer treatment requires delivering anticancer drugs to cancerous cells using appropriate carrier system. As cancer cells are negatively charged, designing positively charged carrier system is the

most preferred strategy. However, bare positively charged carrier system pose cytotoxic activity raising concern for its application. As MSNs are reported to enhance solubility of hydrophobic drugs, it can be selected as the carrier system owing to its ability of surface functionalization. MSNs with different surface functionalization can be evaluated to study its efficacy as drug carrier in enhancing cytotoxicity of encapsulated hydrophobic anticancer drug.

1.2 Aim of the research and its Significance

As the hydrophobic drugs (such as anticancer drugs) possess drawback of low aqueous solubility, it is important to enhance their solubility using a general strategy. Most of the anticancer drugs are hydrophobic in nature with low aqueous solubility and this technique could help in cancer treatment. Carrier system plays an important role in delivering the drugs to its specific site. Especially, in cancer as the cancer cells are negatively charged, positively charged carrier systems are more preferred but pose cytotoxic activity. Positively charged mesoporous silica nanoparticles are studied as carrier system for cancer disease but face toxicity issues owing to the agents used for their surface functionalization. Hence, it is important to study the influence of surface functionalization in proposing mesoporous silica nanoparticles as carrier system.

The specific objectives of this research are:

1. To develop a technique for solubility enhancement by controlling the pore size of mesoporous silica nanoparticles at angstrom scale to find an optimized pore size for a given hydrophobic drug.
2. To study the efficacy of mesoporous silica nanoparticles as carrier system for enhancing cytotoxicity of anticancer drugs.
3. To study the influence of surface functionalized mesoporous silica nanoparticles on drug solubility and drug release.
4. To study the influence of surface functionalized mesoporous silica nanoparticles on cytotoxicity of anticancer drugs.

This research would address the challenge of enhancing the solubility of hydrophobic drugs by proposing a novel method to control the pore size of mesoporous silica nanoparticles at angstrom scale. As this strategy could be applied to all hydrophobic drugs, it would help significantly towards

the development of effective drug delivery system. The findings generated by encapsulating hydrophobic anticancer drug in mesoporous silica nanoparticles and carefully evaluating the influence of surface functionalization on drug solubility, drug release and cytotoxicity better understanding and new strategies could be developed for cancer treatment.

1.3 Structure of the thesis

Chapter 1 Introduction

A brief overview of the background of this research work, including aims and significance are presented.

Chapter 2 Literature Review

A literature review focusing on solubility enhancement techniques is presented. A detailed review of the contributions made by the mesoporous silica nanoparticles as drug delivery system including effect of pore size, surface functionalization and cytotoxicity is presented.

Chapter 3 Research Methodology

The systematic approach in this research work is presented.

Chapter 4 Stepwise Pore Size Reduction of Ordered Nanoporous Silica Materials at Angstrom Precision

In this chapter we report, a novel technique for controlling pore size of mesoporous silica nanoparticles at angstrom scale and demonstrating its application for solubility enhancement of hydrophobic drug. This chapter was published in *Journal of the American Chemical Society*, 2013, 135, 8444-8447.

Chapter 5 Mesoporous Silica Nanoparticles Enhance the Cytotoxicity of Curcumin

In this chapter, mesoporous silica nanoparticles are studied as drug carrier system by encapsulating hydrophobic anticancer drug in it and studied for its cytotoxicity. Encapsulation of drug in

mesoporous silica nanoparticle resulted in cytotoxicity enhancement compared to the pure drug signifying its advantage as drug carrier system. This chapter was published in *RSC Advances, 2014, 4(2), 709-712.*

Chapter 6 Effect of Surface Functionality of Silica Nanoparticles on Cellular Uptake and Cytotoxicity

This chapter is continuation of chapter 5 where in mesoporous silica nanoparticles with different surface chemistry (surface charge and hydrophobicity) are synthesized and studied for its influence on drug release, cytotoxicity by encapsulating the above hydrophobic anticancer drug. Detailed investigation is performed to understand the effect of surface chemistry on anticancer activity using anticancer cell line. This chapter is submitted to *Molecular Pharmaceutics, 2014.*

Chapter 7 Modulating in vitro Release and Solubility of Griseofulvin Using Functionalised Mesoporous Silica Nanoparticles

To confirm the finding from chapter 6 emphasizing the role of surface functionality, the mesoporous silica nanoparticles with different surface chemistry (surface charge and hydrophobicity) were studied for their influence on drug solubility and drug release using a hydrophobic antifungal drug. This chapter is submitted to *Journal of Colloid and Interface Sciences, 2014.*

Chapter 8 Conclusions and Recommendations

Conclusion and major contributions of this work are highlighted and recommendations for future works are presented.

Chapter 2

Literature Review

2.1 Hydrophobic drugs and its dilemma

More than 40% of newer drug molecules emerging from high-throughput screening for treating diseases such as cancer (anti-cancer drugs such as Paclitaxel, Camptothecin, etc.), fungal infection (anti-fungal drugs such as Amphotericin B, Itraconazole, Griseofulvin etc.), anxiety (anti-anxiety drugs such as Alprazolam, Diazepam, Lorazepam etc.), diabetes (anti-diabetic drugs such as Glibenclamide, Glipizide, etc.), inflammation (anti-inflammatory drugs such as Ibuprofen, Naproxen, Diclofenac etc), etc. are hydrophobic in nature possessing poor aqueous solubility, resulting in low bioavailability and reduced patient compliance requiring to have frequent administration of drug.[1,2] These characteristics not only create an obstacle in drug formulation development but also delays their clinical applications.[3] Hence there is a need to address these concerns by developing efficient solubility enhancement method and designing appropriate drug carrier system.

2.1.1 Enhancement of drug solubility – Conventional approach

To overcome the poor aqueous solubility of such hydrophobic drugs, conventional strategies such as salt formation, complexation, use of co-solvents, etc. are employed.

As most of the active drug molecules have poor aqueous solubility, its salt forms were synthesized. This salt form of the drug molecules not only retained the pharmacological activity of the drug but also enhanced its aqueous solubility. The most common drug-salt form comprise of chlorides, carbonate, maleate, citrate etc. Many products with drug-salt form as active constituent have been commercially synthesized such as Diclofenac sodium, chlorphenaramine maleate, etc.[4]

Complexation technique employs conjugation of drug molecules within the cavity of cyclodextrins (CD). Various kinds of cyclodextrin are currently available such as α-CD, β-CD, γ-CD, Hydroxypropyl β-CD, etc. CD were discovered in 1891 however it's industrial application

begun in 1970s. Till date several product have been developed using CD to enhance solubility for drugs such as Piroxicam, Itraconazole, Hydrocortisone, etc.[5]

Co-solvents are mixtures of water and one or more water miscible solvents used to create a solution with enhanced solubility for hydrophobic drug molecules. The most commonly used co-solvents used are propylene glycol, ethanol, glycerin, polyethylene glycol, and Dimethylsulfoxide (DMSO), etc.[4]

The conventional strategies employed face the problems of precipitation, toxicity and altered pharmacological activity.[3,6,7] Also, these techniques are not applicable to all the drug molecules which results in exploring effective techniques to enhance the drug solubility.

2.1.2 Relationship between solubility and drug particle size

Reducing micron-sized drug particles to the nano range or sub-100 nm range is important as it leads to an increase in saturation solubility and dissolution velocity because of the change in physicochemical properties which is the basis of nanotechnology and explained by Ostwald-Freundlich and Noyes-Whitney equations respectively.[3,8]

In general, the solubility of a particle is related to both its bulk molecular property and interfacial property, which can be described by the Ostwald-Freundlich equation (Eq. 1) according to which a decrease in particle size (r) results in an increase in saturation solubility of the drug.[9]

$$S/S_0 = exp\ (2\gamma M / r\rho RT) \quad \text{---------- Eq. 1}$$

where S is the solubility of a spherical particle of radius r,
S_0 is the equilibrium solubility,
R is the universal gas constant,
T is the temperature,
M is the molecular weight,
ρ is the density and
γ is the solid-liquid interfacial tension.

In the case of hydrophobic drug molecule - curcumin, Eq. (1) can be rewritten as (assuming T = 298 K, M = 368 g/mol, ρ = 1.0 g/cm3)

$$S/S_0 = exp\ (0.3\gamma / r)$$ ---------- Eq. 2

To semi-quantitatively explain the *S*-*r* relationship, we arbitrarily define r_c as the critical radius where S/S_0 = 2. Because there is no method available to precisely determine γ, the value of γ is also arbitrarily set in a common range of 5-20 mN/m. As shown in Fig. 1, it can be seen that in order to achieve S/S_0 = 2, r_c is 2.2, 4.3 and 8.7 nm when γ is adjusted to 5, 10 and 20 mN/m, respectively. Moreover, it is also clearly seen that *S* increases more significantly when $r < r_c$. Therefore, in order to significantly enhance the solubility of hydrophobic drugs, it is extremely important to restrict their particle size in the range of 1-10 nm, especially for drugs with low γ values.

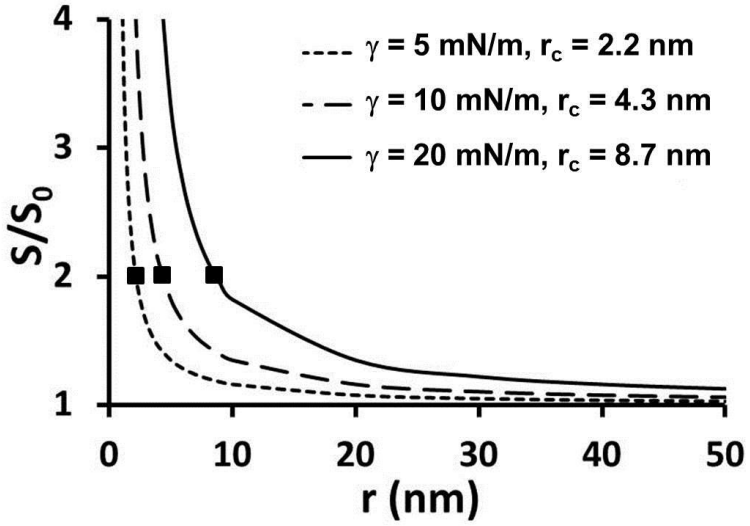

Fig. 2.1 Influence of drug particle size on solubility at different interfacial tensions based on Ostwald-Freundlich equation for curcumin.

On size reduction, the surface area of a particle increases drastically, thereby a tremendous rise in dissolution velocity is observed as given by the modified Noyes-Whitney equation[10] (Eq. 3) describing the dissolution velocity

$$-dM/dt = DA/h\ (C_S - C_B)$$ ---------- Eq. 3

where *M* is mass of drug dissolved in time *t*,
D is diffusion coefficient of drug in medium,

A is surface area,

h is thickness of stagnant film layer,

C_S is saturation solubility at drug-media interface and C_B is drug concentration in bulk medium.

On careful evaluation of the parameters involved in the above equation with respect to their role in dissolution it can be seen that surface area and solubility can lead to significant enhancement in dissolution velocity of the drug.

2.1.3 Relationship between solubility and surface charge

For a given drug, its surface charge can be defined by its dissociation constant which plays an important role in influencing its solubility. Most of the drugs are weak electrolytes and have tendency to undergo ionisation in solution. Drugs are more soluble in its ionised state while reflect poor solubility in its unionised state. The degree of drug ionisation is governed by two factors – dissociation constant and pH of the medium.

The equilibrium achieved by weakly acidic drug, HA in solution can be represented as:

$HA \rightleftharpoons H^+ + A^-$ ---------- Eq. 4

Similarly the protonation of weakly basic drug, B can be represented as:

$B + H^+ \rightleftharpoons BH^+$ ---------- Eq. 5

Solving the above equilibrium reactions we are able to obtain following equations which are termed as Henderson-Hasselbalch equation and describe the relationship between the dissociation constant of the drug and the pH of the medium.

For weakly acidic drugs: $pK_a = pH + \log_{10} [HA] / [A^-]$ ---------- Eq. 6

For weakly basic drugs: $pK_b = pH + \log_{10} [BH^+] / [B]$ ---------- Eq. 7

The symbol pK_a is used to represent the negative logarithm of the acid dissociation constant, K_a in an analogous way where pH is used to represent the negative logarithm of the hydrogen ion concentration. Similarly, pK_b represents the negative logarithm of the basic dissociation constant, K_b.

An increase in solubility can be observed with increasing pH for weakly acidic drugs as the concentration of ionized species is higher compared to that of unionized species. Conversely, increase in solubility can be observed for weakly basic drugs with decrease in pH. This relationship between drug's dissociation constant and pH helps to understand the solubility of drug and its effect on bioavailability.[11]

2.1.4 Enhancement of drug solubility – Nanotechnology approach

With the need to enhance the drug solubility, drug particle size reduction is seen as the most promising approach leading to new era of nanotechnology. Nanotechnology involves 'bottom up' and 'top down' (also known as nanosizing) approaches to achieve solubility enhancement.[8,12]

The bottom up approach involves a controlled precipitation process in which the drug is dissolved in a solvent and this solvent solution is then added to a non-solvent medium resulting in precipitation to form crystalline or amorphous drug particles. There are various controlled drug precipitation process wherein we can obtain water-insoluble colorants in colloid-disperse form (patented process by BASF)[13], cold-water dispersible powders such as carotenoid preparation (patented process by BASF)[14,15], and generation of amorphous drug particles which are marketed by the name of Nanomorph™. There are few more techniques such as highgravity controlled precipitation technology, sonocrystallization etc. which helps in obtaining drug crystals for solubility enhancement.[8] The main disadvantage of bottom-up approach is the removal of organic solvent used in the process. Hence, this approach is not the preferred approach for solubility enhancement.

Top-down approach includes techniques such as micronization.[2,16] Micronization technique represents processes such as milling and homogenization. The most preferred milling process is the wet milling where in the drug is dispersed in surfactant solution or a stabilizer solution and subjected to milling process. Wet milling can be conducted using either high energy or low energy. A low energy wet milling processes is pearl mill which can reduce the drug particle size range of 0.2 – 0.4 mm.[2] The low energy wet milling takes longer duration of upto several days for drug particle size reduction. Alternatively, high energy wet milling processes can reduce the drug particle in 30-120 mins making it industrially favourable. Nanocrystal™ process is based on such high energy wet milling process.[12]

Homogenization process involves drug attrition to small size under high energy. The sample preparation is similar to the wet milling process which involves preparation of dispersion medium containing drug and stabiliser/ surfactant.[17] The advantages of homogenization process is reduction in time, reduced microbiological issues and less contamination compared to the milling process.[18] Nanosuspension formulated using homogenization process helps in increasing the chemical stability of the drug which was demonstrated using Omeprazole as the drug molecule. Omeprazole nanosuspension exhibited excellent stability and there was no change in the drug content or color as compared to the Omeparzole suspension prepared by conventional technique.[19]

The major drawback of top-down approach is that it is time and energy consuming, the drug particle size achieved is larger than 100nm and drug particles are prone to degradation due to mechanical stress involved in the process and have a tendency to agglomerate.[20] Also, specially designed equipments are required to meet the demands of high energy wet milling process.[12] The nanosizing technique has been successfully applied for a few hydrophobic drugs to improve their dissolution rate *in vitro* and their bioavailability.[21] The complete list of drug molecules approved by FDA for commercial sale is listed in the table 1 below.

Company	**Trade Name**	**Drug**	**FDA approval date**	**Description**	**Technology**	**Advantage**
Wyeth Pharmaceuticals	Rapamune®	Sirolimus	Aug. 2000	Tablet	Wet milling	Improved bioavailability, dose proportionality, absorption variability
Merck	Emend®	Aprepitant	Mar. 2003	Capsule	Wet milling	Eliminating food effect
Abbott labs	TRICOR®	Fenofibrate	Dec. 2004	Tablet	Wet milling	Eliminating fed/fast effect
Par Pharmaceuticals	Megace ES®	Megestrol acetate	Jul. 2005	Oral suspension	Wet milling	Rapid onset of action, lower dosing regimen
Nucryst Pharmaceuticals	NPI 32101	Silver	Jul. 2007	Topical cream	Magnetron sputtering	Enhanced antimicrobial activity
Janssen Pharmaceuticals	Invega® Sustenna™	Paliperidone Palmitate	Jul. 2009	Extended release injectable suspension	Wet milling	Reducing risk of relapse

Table 2.1. Commercialized Nanocrystal based Drug Formulation (reproduced from ref. 4)

The drug particle size achieved by the existing nanotechnology approach is still above 100 nm and based on Ostwald-Freundlich equation, if we are able to reduce the drug particle size below 50 or 10 nm, we may be able to observe drastic increase in solubility. Thus the limited success achieved to date with the nanotechnology approach, demands the development of a general strategy to downsize the drug particles to sub-nano scale or even smaller, to further increase the solubility and bioavailability of hydrophobic drugs.

2.1.5 Drug Delivery Systems

A drug delivery system (DDS) is a two component system comprising of 'Drug' and 'Delivery system'. The first component of DDS – Drug is defined as "a substance intended for use in the diagnosis, cure, mitigation, treatment, or prevention of disease" according to U.S. FDA.[22] However, most of the drugs cannot be administered in the body directly as they have certain physicochemical limitations such as low aqueous solubility, poor permeability, unstable to light, unpalatability to name a few. Hence, it is important to select or design an appropriate delivery system which would help in improving the drug efficacy and safety.

The second component of DDS – Delivery system is defined as a formulation or a device that enables the introduction of a therapeutic substance or drug in the body improving its efficacy and safety by controlling the rate, time, and place of drug release in the body.[23] To cater the above requirement, various delivery systems such as tablets, capsules, suspensions, injections, etc. had been developed. For example, Ibuprofen – a well-known drug for treating pain and inflammation has low aqueous solubility and bitter taste[24] and hence it is administered in the form of tablet or suspension to overcome its limitations. The solubility of Ibuprofen in the tablet or suspension can be enhanced by one of the approaches such as reducing its particle size by top-down or bottom-up technique or by using an inclusion complex of ibuprofen and cyclodextrin or by obtaining microsphere of Ibuprofen and polymer in the formulations.

2.1.6 Current Drug Carrier systems

The drug particle size obtained using either of the nanotechnological approach needs to be administered to the patients using an appropriate delivery system. Moreover, the drug carrier system used in DDS should have ideal features such as bioinertness, biodegradability, physicochemical and structural stability, lack of immunogenicity, cellular targetability, programmability, zero premature

drug leakage until it reaches the target cell, facile synthesis process with high reproducibility.[23] In quest of developing such an ideal DDS several novel systems such as liposomes, dendrimers, polymeric nanoparticles, solid dispersions, microemulsions, etc. have been developed. However, these systems possess drawbacks such as low drug loading, poor stability, tedious synthesis process, etc.

In comparison to the above organic based DDS, inorganic mesoporous silica nanoparticles have attracted huge research interest in the fields of catalysis and DDS.[25] Since the first study, it has attracted enormous interest in drug delivery field and several studies have been conducted to study its efficacy and found to be almost fulfilling the ideal DDS characteristics.

2.2 Mesoporous silica materials

Mesoporous silica nanoparticles (MSNs) are inorganic nanoparticles composed of silica with uniform mesopores of diameter between 2 – 50 nm as per IUPAC.[26] The first MSNs were discovered by Mobil researchers in 1992 which was named as Mobil Crystalline Materials (MCM-41)[27] for catalysis. MSN possess unique characteristics of high surface area, adjustable pore size and particle size, facile surface functionalization which lead to its application in adsorption, ion exchange, advanced catalysts, sensors and various other fields.[28-36] Realising the potential of such inorganic silica nanoparticles, variety of MSN structures such as SBA-15[37], MSU-1[38], KIT-6[39], FSM-16[40], FDU family[41] and many more are synthesized till date.

Among the several properties of MSNs, uniform and tuneable pore size and ease of surface functionalization are the most important criteria which have enticed researchers for its diverse applications. More specifically, these properties play vital role in the field of pharmaceutical drug delivery and peptide/ protein encapsulation to enhance the properties of encapsulated drugs and peptides/ proteins. Maria Vallet-Regi *et al*. was first to report the application of MSN in drug delivery using Ibuprofen as the drug molecule.[25]

2.2.1 Methods for pore size control

The pore size is one of the most important features of MSNs for its application in catalysis by entrapping the metal particle in the pore channels or in drug delivery by encapsulating drug molecules in the pore channels. In catalysis, the entrapment of metal particle in smaller pores leads to smaller metal particle size resulting in larger surface area and high reactivity favouring faster

reactions. Similarly, in drug delivery the encapsulation of drug molecules in pore channels would lead to reduction in drug molecules at nanoscale leading to higher surface area and also changing its crystallinity to non-crystalline state. These effect leads to enhanced drug release. This advantage of pore channel size to enhance drug release has been widely studied using MCM-41, MCM-48 and SBA-15 materials.

Based on the Ostwald-Freundlich equation, we observed that, solubility of hydrophobic drugs increases dramatically when the particle size is below 10 nm. The commercial techniques to decrease drug particle size such as micronization, homogenizer, nanomilling, spray drying etc. face the limitation in which they are unable to reduce drug particle size below 100 nm and as these techniques involve mechanical stress it may lead to drug degradation.[12] Hence, it is important to find a process by which we can reduce the drug particle size below 100 nm and more preferably below 10 nm.

The existing techniques to control pore size thus can be broadly classified into three classes:

a) Increasing the pore size by varying synthesis conditions,

b) Decreasing the pore size using grafting process and

c) ALD or CVD process.

a) Increasing the pore size by varying synthesis conditions

The pore size of MCM-41 was controlled by adjusting the pH of the synthesis mixture from pH 11.5 to 10.0 resulting in pore size variation from 3.8 nm to 5.3 nm. This pH variation during synthesis causes change in the electrostatic charge distribution which affects the interaction of micelle head group resulting in pore expansion. The MCM-41 obtained by this process has different morphology based on the pH of the synthesis mixture.[42] This method lacks fine pore size control and requires newly synthesized material to achieve pore size control.

Pore size control on SBA-15 was achieved by varying the temperature and time of hydrothermal treatment in the presence of hexane as the micelle expander. Initial pore size of SBA-15 (9.4 nm) was increased in the range of 11.9 nm – 18.2 nm by varying the hydrothermal treatment temperature from 40°C – 130°C and duration of hydrothermal treatment from 1 day – 5 days.[43] The material obtained by this process have ordered structure (Ordered structure for SBA-15 is defined as the arrangement of pore channels with well-defined size and uniform shape yielding array of non-

intersecting hexagonal channels over micrometer length scale.) however, the pore size control achieved by varying the synthesis conditions lacks fine pore size control.

Pore size control was achieved on titanium containing MCM-41 (Ti-MCM-41) using swelling agents such as dodecylamine, *n*-heptane and trimethylbenzene. Use of the swelling agents – dodecylamine, *n*-heptane and trimethylbenzene resulted in pore size of 4.51 nm, 4.83 nm and 3.05 nm compared to parent Ti-MCM-41 with 2.86 nm.[44] The swelling agent did increase the pore size however it affected their ordered structure especially, with the inclusion of dodecylamine, the ordered structure was completely destroyed. Thus the pore size control achieved by this method has the disadvantage of affecting the ordered structure. Most importantly, the pore size control is in a broad range.

b) Decreasing the pore size using grafting process

Pore size reduction was achieved using a post grafting method on MCM-41 wherein trimethylchlorosilane (TMCS) was used as silica precursor. This method imparts hydrophobicity to MCM-41 material by the addition of methyl groups and reducing the pore size from 2.95 nm to 2.30 nm.[45] However, this method cannot be used in repetitive manner to further decrease the pore size and pore size reduction is at a relatively larger value.

Pore size control was performed using supercritical fluids (SCF such as CO_2) wherein FSM-16 was used as the MSN. This method involved synthesizing FSM-16 using surfactants with varying alkyl chain length (n= 8, 10, 12 and 16) and then exposing to silica precursor (TEOS) dissolved in SCF under the influence of temperature and pressure. The pore size was reduced in a range of 0.1 – 0.9 nm as the alkyl chain length increased for these materials and repeatability of the process was not discussed.[46]

Pore size of MCM-41 was varied by selecting surfactants with different alkyl chain lengths. C_nTAB surfactants with varying alkyl chain length, n= 16 and 12 used in the synthesis of MCM-41 which resulted in pore size of 2.5 and 1.8 nm respectively.[25] This method lacks fine pore size control and the material synthesis requires surfactants with different chain lengths.

c) ALD or CVD process

Atomic layer deposition (ALD) process was utilized for pore size reduction on MSN. ALD is based on sequential self-limiting surface reactions which involve reaction of two gas phase molecules A, B in sequential manner with the substrate in ABAB... sequence. The gas molecule (A) react with surface species such as silanol groups adding the desired atomic element and changing the surface species to a new surface group. In subsequent step, (B) gas molecules react with this new surface group and add second desired atomic element. This second reaction with (B) gas molecules changes the surface group back to the original surface species. The overall reaction of A and B gas molecules results in a deposition of thin films at atomic scale.[47]

ALD process was used to achieve pore size reduction in SBA-15 using $TiCl_4$ and water as the precursors resulting in titania coated SBA-15. The pore size was reduced from 6.7 nm to 3.2 nm after 18 ALD cycles. Pore size reduction after each cycle was not measured however, on an average basis after 18 ALD cycles, pore size reduction was found to be 0.18 nm/ cycle.[48] The average pore size reduction was in quite small range which would be beneficial in reducing pore size at angstrom scale however, inability to achieve such pore size reduction after each cycle makes this process unattractive. Also, the material obtained after ALD cycle was different from parent SBA-15 because of titania coating on its surface.

In another such study pore size reduction was attained on SBA-15 using niobium ethoxide and water as the precursors resulting in niobia coated SBA-15. The pore size reduced from 6.49 nm to 5.80 nm, 5.60 nm, 4.75 nm and 3.74 nm after 1, 10, 19 and 30 ALD cycles respectively.[49] The pore size reduction obtained is 0.1 nm on an average after 30 ALD cycles. However, this method results in material with niobia coating and does not give a precisely controlled size reduction after each ALD cycle similar to the above study.

In another approach, chemical vapour deposition (CVD) process using water and tetraethoxy orthosilicate (TEOS) as the silica precursor was used to tailor the pore size of MCM-41 with initial pore size of 3.0 nm. MCM-41 was exposed to TEOS and water vapours alternatively in cyclic manner for three cycles followed by calcination. This process resulted in ink-bottle like structure with pore entrance of 1.35 nm and inner pore diameter of 3.0 nm. The average pore size reduction achieved by this process is 0.55 nm/cycle lacking fine control on pore size reduction after each cycle.[50]

Pore size control was achieved on SBA-15 material using metallorganic chemical vapour deposition (MOCVD) process wherein the pore opening was decreased from 5.78 nm to 3.7 nm using carbon and copper coating while retaining its pore volume and surface area forming an ink-bottle like structure similar to MCM-41 mentioned earlier.[51]

Different silica precursors such as TEOS and TMOS were utilized for pore size reduction of MCM-41 using CVD process by varying the number of CVD cycles, deposition temperature (130, 300 and 400°C) and deposition time (3 and 6 hrs). Variation in temperature, time and number of CVD cycles decreased pore size in the range of 0.2 – 0.5 nm, 0.1 – 0.5 nm and 0.0 – 0.5 nm respectively. Pore size reduction achieved by this process varied widely displaying its limitation to control the pore size at narrow scale.[52]

Thus the above existing techniques to control pore size face the limitation of precisely controlling the pore size change at angstrom scale after each cycle which is important parameter as per the Ostwald-Freundlich equation to achieve solubility enhancement as seen earlier.

2.2.2 Methods for Surface functionalization

MSN surface functionalization plays important role as they can control the drug release and targetability *in vivo*. MSN particles can be functionalized to impart positively charged surface using functional active agents such as 3-aminopropyltriethoxysilane (APTES),[53,54] polyethyleneimine (PEI),[55,56] polylysine,[57,58] etc. or to impart negatively charged surface using polyphoshonate,[59,60] carboxylic acid,[61,62] etc. or to impart hydrophobicity using Trimethylchlorosilane (TMCS)[45,63] Diethoxydimethylsilane (DEDMS),[64] polymethylhydrosiloxane,[65] hexamethyldisilazane[66,67] etc. Drug molecules are encapsulated in the pores of MSN by electrostatic binding or hydrogen bonding or covalent bonding based on the functional group attached on its surface. This binding force in turn controls the drug release profile from the MSN pores. Moreover, the surface functionalization also helps in specific targeting of the tissues in *in vivo* studies. Specifically, the positively charged drug encapsulated MSN are preferred to target negatively charged cancer cells leading to higher cytotoxicity and efficacy.[68] With this advantages offered by MSNs, materials like MCM-41, MCM-48 and SBA-15 are more widely studied to achieve functional group driven drug release and targeting.

MSN surface functionalization is performed broadly by two methods: a) co-condensation, and b) postsynthetic grafting.

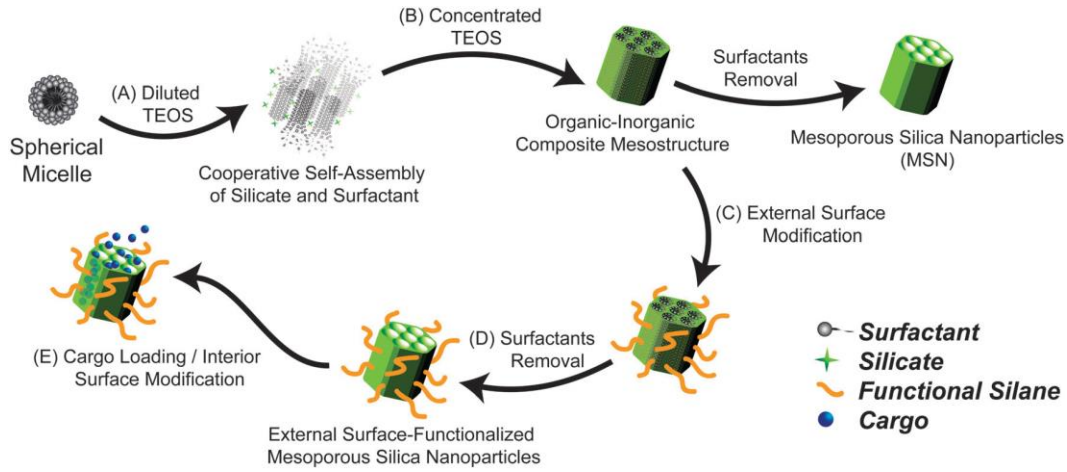

Fig. 2.2 Schematic illustration for the synthesis and selective functionalization of MSNs. (reproduced from ref. 23)

a) Co-condensation:

In this method organosilane and organoalkoxysilane are mixed together during the synthesis in the gel solution with the surfactant assembly still present inside the pores as shown in step B of fig.4. This method results in positioning the organic moiety on the outer surface as shown in step C of fig.4. The surfactant assembly could be then removed using appropriate organic solution and HCl as shown in step D of fig.4. The empty pores can be used as cargo for loading drug or other genetic material. This method offers advantage of being simple, achieving high and uniform distribution of functionalization. However, complete surfactant extraction would be subjected to solvent of choice during extraction.[26,36]

b) Post synthetic grafting:

This method allows the modification of MSN surface after the removal of surfactant template by either solvent extraction or calcination process. Functionalization can be achieved on both interior pore wall surface as well as external surface of MSNs. This is widely used method for functionalization of MSNs using functional groups which are chemically prone to hydrolysis and elimination reactions. To achieve different functional group coverage on interior and external surface of MSN, modification reaction can be started prior to surfactant template removal to have

surface coverage on external wall surface. The surfactant template can then be removed and interior pore surface which possess silanols groups can be used for second functionalization reaction.[26,36]

2.2.3 Drug loading techniques

Since MSNs have found its application as drug delivery carriers, various drug loading methods have been used till date. Below are listed few methods which are employed for encapsulating drugs in MSNs:

a) Immersion method

In this method, MSNs are added to known volume and concentration of drug solution under stirring for a certain time. The drug loaded MSNs are obtained by filtering the suspension or by centrifugation and the filtrate or supernatant obtained is analysed by UV spectrophotometer to determine the drug loading amount. A known quantity of MCM-41 was added to 10 ml of 0.1M Ibuprofen-hexane solution and stirred for 4 hrs. Ibuprofen loaded MCM-41 was obtained by filtering the suspension and analysing the filtrate by UV spectrophotometer.[69] Similar approach was followed for encapsulating various drugs such as Famotidine,[62] Captopril,[70] Doxorubicin,[71-73] Camptothecin,[53,60] Paclitaxel,[60] Ibuprofen,[74-76] Telmisartan,[77] Prednisolone,[78] protoporphyrin IX,[79] Fenofibrate,[80] Curcumin,[81] Sulfadiazine,[82] Celecoxib,[83] etc.

b) Rotavap

In this method, MSNs are added to known volume of drug solution and shaken for certain time. After which the solvent is slowly evaporated from the suspension using rotavapor at a reduced pressure with the aid of temperature. Indomethacin solution was prepared in ethanol and MCM-41 was added to it. Ethanol was slowly evaporated from the suspension at reduced pressure using rotavapor to obtain indomethacin loaded MCM-41.[84] Similar approach was followed for encapsulating drug such as Atazanivir.[85]

c) Fluidized bed method

Fluidized bed drier was used to encapsulate Indomethacin in MCM-41 by spraying the suspension of MCM-41 – Indomethacin solution. Indomethacin solution was prepared by

dissolving it in Ethanol. The rate of spraying and heating temperature in the fluidized bed drier helps in the encapsulation of indomethacin in the pores of MCM-41.[84]

d) Impregnation

This method involves soaking MSNs with drug solution under continuous stirring until dried powder is obtained resulting in impregnation of drug in pores of MSNs. In one such study, Fenofibrate was dissolved in methylene chloride at concentration of 50 mg/ml and added drop wise to MCM-41. This moist mixture was continuously stirred with spatula until dried powder was obtained.[86] Similar approach was followed for encapsulating various drugs such as Aceclofenac,[87] Carvedilol,[88] Ezetimibe,[89] Indomethacin,[90] Glibenclamide,[90]

2.3 MSNs as drug carriers

The first study of MSN as drug carriers was conducted using MCM-41 and Ibuprofen as the drug candidate.[25] MCM-41 materials were prepared by employing two different surfactants – dodecyltrimethylammonium bromide (C_{12}TAB) and hexadecyltrimethylammonium bromide (C_{16}TAB) resulting in pore size of 2.5 nm and 1.8 nm respectively. Ibuprofen encapsulation in MCM-41 materials was performed by immersion method followed by conducting *in-vitro* drug release study. Drug release appeared to increase with the increase in the pore size thus demonstrating the application of MCM-41 as drug carrier.[25]

Effect of MSN surface functionalization on drug loading and drug release was studied by comparing SBA-15 and MCM-41 with and without amino functionalization in this study. SBA-15 and MCM-41 (with and without amino functionalization) materials were compacted into disc and soaked in sodium alendronate solution for its encapsulation. It was found that; sodium alendronate was loaded almost three times higher in amino functionalized MSN (SBA-15 and MCM-41) material compared to bare MSN (SBA-15 and MCM-41) material. This preferential higher loading in amino functionalized MSN material is attributed to the higher affinity of sodium alendronate to the amino groups on MSN. Drug release studies showed slower release of sodium alendronate from amino functionalized MSN compared to bare MSN thus demonstrating the influence of MSN surface functionalization on drug loading and drug release.[91]

Effect of amino functionalized MCM-41 on drug release was reported using Ibuprofen as model drug wherein it was observed that, the drug release was slower for amino functionalized MCM-41 compared to bare MCM-41 demonstrating the influence of surface functionalization.[92]

In another report effect of amino functionalization amount on ibuprofen release was studied. 3-aminopropyltriethoxysilane (APTES) was added in different stoichiometric ratio of 1, 3 and 6 corresponding to the silanol number in MCM-41. It was observed that, the ibuprofen loading increased with increasing APTES amount with ratio of 6 showing highest ibuprofen loading which was attributed to the specific affinity between carboxylic group of ibuprofen and amino groups of APTES grafted on MCM-41. However the drug release decreases with increasing APTES amount which was due to the adsorption of drug in secondary mesopores of MCM-41. Thus choosing an optimal ratio of APTES plays important role in both drug loading and drug release.[76]

Influence of drug loading method on drug release was studied by encapsulating Indomethacin using three different methods – immersion, fluidized bed and rotavap in MCM-41 followed by its compression as tablets. Amongst the different loading methods, fluidized bed and rotavap showed better drug loading and drug release compared to pure drug. Compression of these Indomethacin loaded materials into tablet did not affect the drug release and demonstrates its potential to be used as tablet.[84]

In another study, a hydrophobic plant growth regulator, namely the indole-3-butyric acid (IBA) was used as model drug to study its effect on dissolution after encapsulating it in MCM-41 by immersion method. The drug release of IBA was higher from IBA encapsulated in MCM-41 compared to the physical mixture and pure IBA. Moreover, the aqueous drug solubility was almost twice compared to pure IBA clearly displaying the advantage of utilising MCM-41 as the drug carrier.[93]

Mesoporous silica scaffold was used to encapsulate curcumin to improve its dissolution and photo stability. The drug loading was performed during the synthesis of mesoporous silica scaffold unlike the other methods where in the drug loading is performed post synthesis. The drug release studies were conducted in aqueous sodium hydroxide solution (pH 7.70) which showed controlled release of curcumin further confirming the application of MSNs as effective drug carrier system.[94]

The drug release rate and bioavailability of fenofibrate, a poorly water soluble drug was controlled by controlling the pore size of SBA-15 and MCM-41. SBA-15 materials (pore size of 7.3 nm and 4.4 nm) and MCM-41 materials (pore size of 2.7 nm) were loaded with fenofibrate by impregnation method. It was observed that under sink condition, drug release from SBA-15 (7.3 nm) was very fast while that from SBA-15 (4.4 nm) and MCM-41 (2.7 nm) was relatively slow. Similar observation was seen in animal experiments where in the drug loaded MCM-41 exhibited highest concentration max. and highest area under the curve indicating more sustained super saturation of drug in instestinal media. Thus drug release was controlled by controlling the pore size which led to enhanced dissolution and bioavailability of poorly aqueous soluble drugs.[86]

In a subsequent study, a model hydrophobic drug, Itraconazole was encapsulated in SBA-15 materials with pore size ranging from 4.5 nm, 6.4 nm, 7.9 nm and 9.0 nm. Itraconazole was loaded in SBA-15 materials by immersion method and the drug loading achieved was approximately 10 %. Drug release studies showed slower release from SBA-15 with pore size of 4.5 nm while faster release from SBA-15 materials with pore size above 6.4 nm. The slower itraconazole release from SBA-15 with pore size of 4.5 nm is attributed to molecular diffusion barrier leading to inability of itraconazole molecule to diffuse through the pore channel. Comparatively faster release from larger pore size SBA-15 materials is due to the easy diffusion of itraconazole proposing the existence of an optimized pore size for itraconazole to enhance drug release.[95]

Similar results were observed when Ibuprofen was encapsulated in MCM-48 which has two independent intertwined networks of pore channels (pore size = 3.7 nm) and SBA-15 which has unidirectional pore channels (pore size = 8.8 nm). The pore structure did not show any influence on the drug release however its pore size affected the drug release from first-order kinetics for MCM-48 to zero-order kinetics for SBA-15. Thus, the pore size control plays a crucial role in modulating drug release.[96]

MSN was reported as carrier system for delivering hydrophobic anticancer drug, Camptothecin (CPT) using MCM-41. CPT encapsulated MCM-41 was tested in three pancreatic cancer-cell lines (PANC-1, Capan-1, and AsPc-1), a colon cancer-cell line (SW480), and a stomach cancer-cell line (MKN45) which showed almost complete inhibition similar to that of CPT dissolved in dimethylsulfoxide (DMSO) at 100 nm dose.[53]

Further study of MSN for tumor suppression in pancreatic cancer was demonstrated using CPT as anticancer drug. MSN were grafted with folic acid as ligands on its surface to have specificity towards tumor cells followed by encapsulation of CPT by immersion method. Biocompatibility and excretion of MSN was studied in regular mice and found that MSNs are almost completely excreted within a week and they retain their morphology as well. CPT encapsulated MSNs were injected intraperitoneally at the dose of 7.8 μM to nude mice's with established xenografts of human pancreatic cancer cells, PANC-1 and MiaPaca-2. CPT encapsulated folate grafted MSNs (FMSN) showed superior anti-tumor effect compared to CPT encapsulated MSNs and pure CPT with tumor volume reduced almost completely by 24 days in both PANC-1 and MiaPaca-2 xenograft in nude mice. This study systematically demonstrated the influence of folate receptors to achieve higher targetability to treat tumor using MSNs.[97]

The drug encapsulated in the pore channels of MSNs can have burst release at times as the pore entrance of these pore channels are open (without any capping) to the biological system. Hence, MSNs are closed or capped with chemical moieties which would help to achieve very less drug release or zero drug release in initial period. Several chemical moieties such as pseudorotaxanes,[98,99] iron oxide, cadmium sulphate, β-cyclodextrins, etc. have been used as end capping agents. The end capped MSNs can then be further conjugated with specific ligands to achieve cell-specific targeting.

Redox-responsive MSN system was synthesized and end-capped with collagen to prevent drug leakage. Collagen which is one of the extracellular components was immobilized on the MSN surface by disulphide bonds. Disulfide bonds are easily cleaved by glutathione which are expressed by the cells and thus cargo encapsulated within the MSN pores can be released within the cells. Further lactobionic acid (LA) was grafted on the collagen as the ligand to targeting moiety. Fluorescein isothiocyanate (FITC) was used as the model drug in this study. The redox-responsiveness of the system for controlled release of cargo was studied by using dithiothreitol (DTT) as external stimulus. 6.5% and 80% of FITC was released from MSN with LA grafted on collagen within 2 hrs in the absence and presence of DTT respectively indicating redox responsiveness of the system to DTT. The endocytosis of MSN with LA grafted on collagen study showed two times higher efficiency by HepaG2 cells (receptor for LA) compared to endothelial cells (non-receptor for LA).[100]

2.4 Cytotoxicity of MSNs

Mesoporous Silica Nanoparticle has been proposed as the promising drug delivery system which is aptly supported by several studies conducted in the last decade. However, there are a few concerns regarding its biocompatibility, toxicity in scientific and industrial community. MSNs which are comprised of silica as the main component is accepted as "Generally Recognized As Safe" (GRAS) by the FDA. Silica in the form of colloidal silicon dioxide (also known as Aerosil) is a very well-known glidant and is one of the main excipients in tablets and also reported to find its applications in cosmetics and as food additive.[101,102] Aerosil is reported to have LD_{50} of 1.5 mg/kg for intravenous administration in rats while LD_{50} of 3.16 g/kg for oral administration in rats proposing its safety.[103] However, as the structure of MSNs is different from colloidal silicon dioxide, its biocompatibility relies on various aspects such as MSNs porosity, particle size, shape, surface functionalization, structure and concentration.

The influence of MSN particle size on toxicity was studied by comparing MSNs with sizes of 190, 420 and 1220 nm on breast cancer cell line – MDA-MB-468 cells. MSNs with size of 190 and 420 nm showed significant cytotoxicity at concentrations above 25µg/mL while MSN with size of 1220 nm showed slight cytotoxicity as it has decreased endocytosis.[104] In another study it was seen that MSNs with size of 25, 42, 93, 155 and 225 nm showed concentration and size dependent hemolytic activity wherein the smaller MSNs showed higher hemolysis compared to larger ones.[105] A similar study further confirmed that, the silica particles with smaller size possess higher cytotoxicity. Silica particles with size below 20 nm showed higher cytotoxicity compared to silica particles with size of 104 and 335 nm.[106]

Influence of dosage on cytotoxicity was evaluated where MSNs with size of 270 nm were found to be less toxic than silica particles with size of 2.5 µm and the cytotoxicity increased with increasing dosages in human monocyte-derived dendritic cells.[107] Similar dosage dependent cytotoxic effect of MSNs was observed in a study on COS-7 and MDA-MB-468 cells. No cytotoxicity was observed until concentration of 25 µg/mL. However, above this dose, MSNs showed cytotoxicity.[108]

Prolonged circulation of any drug loaded particles without being detected by reticuloendothelial system (RES) in the body is desirable to achieve better response. Surface modification with polyethylene glycols (PEGs) on MSNs is one such strategy which not only

avoids the RES detection but also increases the dispersity of particles[109]. In another study, effect of surface modification was evaluated by comparing aminopropyl and mercaptopropyl functionalized MCM-41 with unfunctionalized MCM-41 and non-porous silica nanoparticles for cytotoxicity in human neuroblastoma (SK-N-SH) cells. It was found that the unfunctionalized MCM-41 showed least cytotoxicity whereas aminopropyl functionalized MCM-41 and non-porous silica nanoparticles displayed highest cytotoxicity.[110]

The influence of porosity on cytotoxicity was studied by comparing MSNs with non-porous silica nanoparticles in J774A.1 cells. It was found that MSNs showed less cytotoxicity than non-porous silica nanoparticles.[111] A study was conducted to evaluate the influence of porosity, particle shape and surface functionalization on toxicity and hemolysis in RAW 264.7 cell line. It was found that the non-porous silica nanoparticles were less toxic compared to MSNs while the particle shape did not influence the cytotoxicity. When studied for the effect of porosity and surface functionalization, it was observed that, the positive surface functionalization lead to higher hemolysis compared to the unfunctionalized silica materials. Unfunctionalized non-porous silica materials were found to be more biocompatible compared to the non-functionalized MSNs as they displayed less hemolysis. The MSNs with lower aspect ratio displayed higher hemolysis compared to MSNs with higher aspect ratio.[112]

Cytotoxicity of silica materials was evaluated by conducting *in vitro* and *in vivo* studies for MCM-41 and non-porous silica nanoparticles. *In vitro* studies demonstrated that, the MCM-41 display low cytotoxicity than non-porous silica nanoparticles. However, *in vivo* studies showed MCM-41 to be more cytotoxic compared to non-porous silica nanoparticles.[113] Thus toxicity of MSNs is material and cell line dependent making it difficult to deduce any correlation.

The fate of MSNs after administration in rats was studied by using two MSNs – positively and negatively charged MSNs. Positively charged MSNs was found to have rapid uptake and elimination via liver while the negatively charged MSNs had higher uptake and retention in liver. The impact of surface charge can thus be a useful parameter in designing effective nanoparticles with high residence time in the body to impart higher response.[114] As this study was performed using a dye as model drug to demonstrate the influence of surface charge, we propose to study the effect of surface charge and hydrophobicity on drug release and cytotoxicity using model drugs – curcumin and griseofulvin.

References

(1) Lipinski, C. Poor Aqueous Solubility – an Industry Wide Problem in Drug Discovery. *Am.pharm.Rev.* **2002**, *5*, 82-85.

(2) Merisko-Liversidge, E.; Liversidge, G. G.; Cooper, E. R. Nanosizing: a formulation approach for poorly-water-soluble compounds. *Eur. J. Pharm. Sci.* **2003**, *18*, 113-120.

(3) Nagarwal, R. C.; Kumar, R.; Dhanawat, M.; Das, N.; Pandit, J. K. Nanocrystal Technology in the Delivery of Poorly Soluble Drugs: An Overview. *Curr. Drug Deliv.* **2011**, *8*, 398-406.

(4) Berge, S. M.; Bighley, L. D.; Monkhouse, D. C. Pharmaceutical Salts. *J. Pharm. Sci.* **1977**, *66*, 1-19.

(5) Szejtli, J. Past, present, and future of cyclodextrin research. *Pure Appl. Chem.* **2004**, *76*, 1825-1845.

(6) Gad, S. C. Evaluating products for their potential to cause dermal and ocular irritation and corrosion. *J. Toxicol.-Cutan. Ocul. Toxicol.* **2002**, *21*, 213-244.

(7) Amin, K.; Dannenfelser, R. M.; Zielinski, J.; Wang, B. Lyophilization of polyethylene glycol mixtures. *J. Pharm. Sci.* **2004**, *93*, 2244-2249.

(8) Muller, R. H.; Gohla, S.; Keck, C. M. State of the art of nanocrystals - Special features, production, nanotoxicology aspects and intracellular delivery. *Eur. J Pharm. Biopharm.* **2011**, *78*, 1-9.

(9) Ostwald, W. On the assumed isomerism of red and yellow mercury oxide and the surface-tension of solid bodies. *Z Phys Che-Stoch Ve* **1900**, *34*, 495-503.

(10) Gowthamarajan, K.; Singh, S. K. Dissolution Testing for Poorly Soluble Drugs: A Continuing Perspective. *Dissolut. Technol.* **2010**, *17*, 24-32.

(11) Aulton, M. E. T., Kevin *Aulton's pharmaceutics*; 4th ed. ed.; Churchill Livingstone/Elsevier: New York, Edinburgh, 2013.

(12) Moschwitzer, J. P. Drug nanocrystals in the commercial pharmaceutical development process. *Int. J Pharm.* **2013**, *453*, 142-156.

(13) Auweter, H.; Bohn, H.; Heger, R.; Horn, D.; Siegel, B.; Siemensmeyer, K. Precipitated Water-insoluble Colorants In Colloid Disperse Form, **2002**, *WO9951695-A; EP1066355-A; DE19815129-A1; WO9951695-A1; EP1066355-A1; JP2002510739-W; US6494924-B1; EP1066355-B1; DE59907374-G*

(14) Runge, F.; Auweter, H.; Musaeus-Jensen, N.; Haberkorn, H.; Rieger, J. Stable, pulverulent lycopene formulations, comprising lycopene having a degree of crystallinity of greater than 20%, **2001**, *US 6235315*

(15) Auweter, H.; Bohn, H.; Luddecke, E. Stable, aqueous dispersions and stable, water-dispersible dry xanthophyll powder, their production and use, **2001**, *US 6296877*

(16) Rabinow, B. E. Nanosuspensions in drug delivery. *Nat. Rev. Drug Discov.* **2004**, *3*, 785-796.

(17) Wu, L.; Zhang, J.; Watanabe, W. Physical and chemical stability of drug nanoparticles. *Adv. Drug. Deliver. Rev.* **2011**, *63*, 456-469.

(18) Teeranachaideekul, V.; Junyaprasert, V. B.; Souto, E. B.; Mueller, R. H. Development of ascorbyl palmitate nanocrystals applying the nanosuspension technology. *Int. J. Pharm.* **2008**, *354*, 227-234.

(19) Moschwitzer, J.; Achleitner, G.; Pomper, H.; Muller, R. H. Development of an intravenously injectable chemically stable aqueous omeprazole formulation using nanosuspension technology. *Eur. J. Pharm. Biopharm.* **2004**, *58*, 615-619.

(20) Afolabi, A.; Akinlabi, O.; Bilgili, E. Impact of process parameters on the breakage kinetics of poorly water-soluble drugs during wet stirred media milling: A microhydrodynamic view. *Eur. J Pharm. Sci* **2014**, *51*, 75-86.

(21) Kesisoglou, F.; Panmai, S.; Wu, Y. H. Nanosizing - Oral formulation development and biopharmaceutical evaluation. *Adv. Drug Deliver. Rev.* **2007**, *59*, 631-644.

(22) FDA, U. S. "Regulatory Information" http://www.fda.gov/RegulatoryInformation/Legislation/FederalFoodDrugandCosmeticActFDCAct/FDCActChaptersIandIIShortTitleandDefinitions/ucm086297.htm. **2012**.

(23) Jain, K. K.; Jain, K. K., Ed.; Humana Press: 2008, p 1-254.

(24) Weiss, G.; Knoch, A.; Laicher, A.; Stanislaus, F.; Daniels, R. Simple coacervation of hydroxypropyl methylcellulose phthalate (HPMCP) II. Microencapsulation of Ibuprofen. *Int. J. Pharm.* **1995**, *124*, 97-105.

(25) Vallet-Regi, M.; Ramila, A.; del Real, R. P.; Perez-Pariente, J. A new property of MCM-41: Drug delivery system. *Chem. Mat.* **2001**, *13*, 308-311.

(26) Tarn, D.; Ashley, C. E.; Xue, M.; Carnes, E. C.; Zink, J. I.; Brinker, C. J. Mesoporous Silica Nanoparticle Nanocarriers: Biofunctionality and Biocompatibility. *Accounts Chem Res* **2013**, *46*, 792-801.

(27) Kresge, C. T.; Leonowicz, M. E.; Roth, W. J.; Vartuli, J. C.; Beck, J. S. Ordered mesoporous molecular-sieves synthesized by a liquid-crystal template mechanism. *Nature* **1992**, *359*, 710-712.

(28) Somorjai, G. A.; Frei, H.; Park, J. Y. Advancing the Frontiers in Nanocatalysis, Biointerfaces, and Renewable Energy Conversion by Innovations of Surface Techniques. *J. Am. Chem. Soc.* **2009**, *131*, 16589-16605.

(29) Corma, A. From microporous to mesoporous molecular sieve materials and their use in catalysis. *Chem. Rev.* **1997**, *97*, 2373-2419.

(30) Sayari, A. Catalysis by crystalline mesoporous molecular sieves. *Chem. Mater.* **1996**, *8*, 1840-1852.

(31) Ariga, K.; Vinu, A.; Hill, J. P.; Mori, T. Coordination chemistry and supramolecular chemistry in mesoporous nanospace. *Coordin. Chem. Rev.* **2007**, *251*, 2562-2591.

(32) Srivastava, R.; Choi, M.; Ryoo, R. Mesoporous materials with zeolite framework: remarkable effect of the hierarchical structure for retardation of catalyst deactivation. *Chem. Commun.* **2006**, 4489-4491.

(33) Wan, Y.; Shi, Y. F.; Zhao, D. Y. Designed synthesis of mesoporous solids via nonionic-surfactant-templating approach. *Chem. Commun.* **2007**, 897-926.

(34) Hu, X. J.; Qiao, S. Z.; Zhao, X. S.; Lu, G. Q. Adsorption study of benzene in ink-bottle-like MCM-41. *Ind. Eng. Chem. Res.* **2001**, *40*, 862-867.

(35) Vallet-Regi, M.; Balas, F.; Arcos, D. Mesoporous materials for drug delivery. *Angew. Chem. Int. Edit.* **2007**, *46*, 7548-7558.

(36) Wu, S. H.; Hung, Y.; Mou, C. Y. Mesoporous silica nanoparticles as nanocarriers. *Chem. Commun.* **2011**, *47*, 9972-9985.

(37) Zhao, D. Y.; Feng, J. L.; Huo, Q. S.; Melosh, N.; Fredrickson, G. H.; Chmelka, B. F.; Stucky, G. D. Triblock copolymer syntheses of mesoporous silica with periodic 50 to 300 angstrom pores. *Science* **1998**, *279*, 548-552.

(38) Bagshaw, S. A.; Prouzet, E.; Pinnavaia, T. J. Templating of mesoporous molecular-sieves by nonionic polyethylene oxide surfactants. *Science* **1995**, *269*, 1242-1244.

(39) Ryoo, R.; Kim, J. M.; Ko, C. H.; Shin, C. H. Disordered molecular sieve with branched mesoporous channel network. *J Phys. Chem.-US* **1996**, *100*, 17718-17721.

(40) Inagaki, S.; Fukushima, Y.; Kuroda, K. *SYNTHESIS AND CHARACTERIZATION OF HIGHLY ORDERED MESOPOROUS MATERIAL - FSM-16, FROM A LAYERED POLYSILICATE*; Elsevier Science Publ B V: Amsterdam, 1994; Vol. 84.

(41) Huo, Q. S.; Margolese, D. I.; Ciesla, U.; Feng, P. Y.; Gier, T. E.; Sieger, P.; Leon, R.; Petroff, P. M.; Schuth, F.; Stucky, G. D. Generalized synthesis of periodic surfactant inorganic composite-materials. *Nature* **1994**, *368*, 317-321.

(42) Wang, A. J.; Kabe, T. Fine-tuning of pore size of MCM-41 by adjusting the initial pH of the synthesis mixture. *Chem. Commun.* **1999**, 2067-2068.

(43) Kruk, M.; Cao, L. Pore size tailoring in large-pore SBA-15 silica synthesized in the presence of hexane. *Langmuir* **2007**, *23*, 7247-7254.

(44) Wang, S. P.; Shi, Y.; Ma, X. B.; Gong, J. L. Tuning Porosity of Ti-MCM-41: Implication for Shape Selective Catalysis. *ACS Appl. Mater. Interfaces* **2011**, *3*, 2154-2160.

(45) Zhao, X. S.; Lu, G. Q. Modification of MCM-41 by surface silylation with trimethylchlorosilane and adsorption study. *J Phys. Chem. B* **1998**, *102*, 1556-1561.

(46) Wakayama, H.; Goto, Y.; Fukushima, Y. A novel method for tailoring porous structures of nanoporous materials using supercritical solvents. *Phys. Chem. Chem. Phys.* **2003**, *5*, 3784-3788.

(47) Wilson, C. A.; Grubbs, R. K.; George, S. M. Nucleation and growth during Al2O3 atomic layer deposition on polymers. *Chem. Mater.* **2005**, *17*, 5625-5634.

(48) Mahurin, S.; Bao, L.; Yan, W.; Liang, C.; Dai, S. Atomic layer deposition of TiO2 on mesoporous silica. *J. Non-Cryst. Solids* **2006**, *352*, 3280-3284.

(49) Pagan-Torres, Y. J.; Gallo, J. M. R.; Wang, D.; Pham, H. N.; Libera, J. A.; Marshall, C. L.; Elam, J. W.; Datye, A. K.; Dumesic, J. A. Synthesis of Highly Ordered Hydrothermally Stable Mesoporous Niobia Catalysts by Atomic Layer Deposition. *ACS Catal.* **2011**, *1*, 1234-1245.

(50) Zhao, X. S.; Lu, G. Q. M.; Hu, X. A novel method for tailoring the pore-opening size of MCM-41 materials. *Chem. Commun.* **1999**, 1391-1392.

(51) Zhang, Y.; Lam, F. L. Y.; Hu, X. J.; Yan, Z. F. Formation of an ink-bottle-like pore structure in SBA-15 by MOCVD. *Chem. Commun.* **2008**, 5131-5133.

(52) Fodor, K.; Bitter, J. H.; de Jong, K. P. Investigation of vapor-phase silica deposition on MCM-41, using tetraalkoxysilanes. *Micropor. Mesopor. Mat.* **2002**, *56*, 101-109.

(53) Lu, J.; Liong, M.; Zink, J. I.; Tamanoi, F. Mesoporous silica nanoparticles as a delivery system for hydrophobic anticancer drugs. *Small* **2007**, *3*, 1341-1346.

(54) Bardi, G.; Malvindi, M. A.; Gherardini, L.; Costa, M.; Pompa, P. P.; Cingolani, R.; Pizzorusso, T. The biocompatibility of amino functionalized CdSe/ZnS quantum-dot-Doped SiO2 nanoparticles with primary neural cells and their gene carrying performance. *Biomaterials* **2010**, *31*, 6555-6566.

(55) Meng, H.; Mai, W. X.; Zhang, H. Y.; Xue, M.; Xia, T.; Lin, S. J.; Wang, X.; Zhao, Y.; Ji, Z. X.; Zink, J. I.; Nel, A. E. Codelivery of an Optimal Drug/siRNA Combination Using Mesoporous Silica Nanoparticles To Overcome Drug Resistance in Breast Cancer in Vitro and in Vivo. *ACS Nano* **2013**, *7*, 994-1005.

(56) Rosenholm, J. M.; Peuhu, E.; Eriksson, J. E.; Sahlgren, C.; Linden, M. Targeted Intracellular Delivery of Hydrophobic Agents using Mesoporous Hybrid Silica Nanoparticles as Carrier Systems. *Nano Lett.* **2009**, *9*, 3308-3311.

(57) Hartono, S. B.; Gu, W. Y.; Kleitz, F.; Liu, J.; He, L. Z.; Middelberg, A. P. J.; Yu, C. Z.; Lu, G. Q.; Qiao, S. Z. Poly-L-lysine Functionalized Large Pore Cubic Mesostructured Silica Nanoparticles as Biocompatible Carriers for Gene Delivery. *ACS Nano* **2012**, *6*, 2104-2117.

(58) Zhu, Y. F.; Meng, W. J.; Gao, H.; Hanagata, N. Hollow Mesoporous Silica/Poly(L-lysine) Particles for Codelivery of Drug and Gene with Enzyme-Triggered Release Property. *J Phys. Chem. C* **2011**, *115*, 13630-13636.

(59) Meng, H. A.; Liong, M.; Xia, T. A.; Li, Z. X.; Ji, Z. X.; Zink, J. I.; Nel, A. E. Engineered Design of Mesoporous Silica Nanoparticles to Deliver Doxorubicin and P-Glycoprotein siRNA to Overcome Drug Resistance in a Cancer Cell Line. *ACS Nano* **2010**, *4*, 4539-4550.

(60) Liong, M.; Lu, J.; Kovochich, M.; Xia, T.; Ruehm, S. G.; Nel, A. E.; Tamanoi, F.; Zink, J. I. Multifunctional inorganic nanoparticles for imaging, targeting, and drug delivery. *ACS Nano* **2008**, *2*, 889-896.

(61) Yang, Q.; Wang, S. H.; Fan, P. W.; Wang, L. F.; Di, Y.; Lin, K. F.; Xiao, F. S. pH-responsive carrier system based on carboxylic acid modified mesoporous silica and polyelectrolyte for drug delivery. *Chem. Mater.* **2005**, *17*, 5999-6003.

(62) Tang, Q. L.; Xu, Y.; Wu, D.; Sun, Y. H. A study of carboxylic-modified i-nesoporous silica in controlled delivery for drug famotidine. *J Solid State Chem.* **2006**, *179*, 1513-1520.

(63) Park, D. H.; Nishiyama, N.; Egashira, Y.; Ueyama, K. Enhancement of hydrothermal stability and hydrophobicity of a silica MCM-48 membrane by silylation. *Ind. Eng. Chem. Res.* **2001**, *40*, 6105-6110.

(64) Tang, Q.; Chen, Y.; Chen, J.; Li, J.; Xu, Y.; Wu, D.; Sun, Y. Drug delivery from hydrophobic-modified mesoporous silicas: Control via modification level and site-selective modification. *J Solid State Chem.* **2010**, *183*, 76-83.

(65) Yang, D.; Xu, Y.; Wu, D.; Sun, Y.; Zhu, H.; Deng, F. Super hydrophobic mesoporous silica with anchored methyl groups on the surface by a one-step synthesis without surfactant template. *J Phys. Chem. C* **2007**, *111*, 999-1004.

(66) Trouve, A.; Batonneau-Gener, I.; Valange, S.; Bonne, M.; Mignard, S. Tuning the hydrophobicity of mesoporous silica materials for the adsorption of organic pollutant in aqueous solution. *J Hazard Mater.* **2012**, *201*, 107-114.

(67) Batonneau-Gener, I.; Yonli, A.; Trouve, A.; Mignard, S.; Guidotti, M.; Sgobba, M. Tailoring the Hydrophobic Character of Mesoporous Silica by Silylation for VOC Removal. *Separ. Sci. Technol.* **2010**, *45*, 768-775.

(68) Froehlich, E. The role of surface charge in cellular uptake and cytotoxicity of medical nanoparticles. *Int. J Nanomed.* **2012**, *7*, 5577-5591.

(69) Qu, F. Y.; Zhu, G. S.; Lin, H. M.; Zhang, W. W.; Sun, J. Y.; Li, S. G.; Qiu, S. L. A controlled release of ibuprofen by systematically tailoring the morphology of mesoporous silica materials. **2006**, *179*, 2027-2035.

(70) Qu, F. Y.; Zhu, G. S.; Huang, S. Y.; Li, S. G.; Sun, J. Y.; Zhang, D. L.; Qiu, S. L. Controlled release of Captopril by regulating the pore size and morphology of ordered mesoporous silica. *Micropor. Mesopor. Mat.* **2006**, *92*, 1-9.

(71) Mei, X.; Chen, D.; Li, N.; Xu, Q.; Ge, J.; Li, H.; Lu, J. Hollow mesoporous silica nanoparticles conjugated with pH-sensitive amphiphilic diblock polymer for controlled drug release. *Micropor. Mesopor. Mat.* **2012**, *152*, 16-24.

(72) Meng, H.; Xue, M.; Xia, T.; Zhao, Y.-L.; Tamanoi, F.; Stoddart, J. F.; Zink, J. I.; Nel, A. E. Autonomous in Vitro Anticancer Drug Release from Mesoporous Silica Nanoparticles by pH-Sensitive Nanovalves. *J Am. Chem. Soc.* **2010**, *132*, 12690-12697.

(73) Meng, H.; Mai, W. X.; Zhang, H.; Xue, M.; Xia, T.; Lin, S.; Wang, X.; Zhao, Y.; Ji, Z.; Zink, J. I.; Nel, A. E. Codelivery of an Optimal Drug/siRNA Combination Using Mesoporous Silica Nanoparticles To Overcome Drug Resistance in Breast Cancer in Vitro and in Vivo. *ACS Nano* **2013**, *7*, 994-1005.

(74) Popat, A.; Liu, J.; Lu, G. Q.; Qiao, S. Z. A pH-responsive drug delivery system based on chitosan coated mesoporous silica nanoparticles. *J Mater. Chem.* **2012**, *22*, 11173-11178.

(75) Santamaria, E.; Maestro, A.; Porras, M.; Gutierrez, J. M.; Gonzalez, C. Controlled release of ibuprofen by meso-macroporous silica. *J Solid State Chem.* **2014**, *210*, 242-250.

(76) Szegedi, A.; Popova, M.; Goshev, I.; Klebert, S.; Mihaly, J. Controlled drug release on amine functionalized spherical MCM-41. *J Solid State Chem* **2012**, *194*, 257-263.

(77) Zhang, Y. Z.; Zhi, Z. Z.; Jiang, T. Y.; Zhang, J. H.; Wang, Z. Y.; Wang, S. L. Spherical mesoporous silica nanoparticles for loading and release of the poorly water-soluble drug telmisartan. *J Control Release* **2010**, *145*, 257-263.

(78) Martin, A.; Garcia, R. A.; Sen Karaman, D.; Rosenholm, J. M. Polyethyleneimine-functionalized large pore ordered silica materials for poorly water-soluble drug delivery. *J Mater. Sci.* **2014**, *49*, 1437-1447.

(79) Teng, I. T.; Chang, Y. J.; Wang, L. S.; Lu, H. Y.; Wu, L. C.; Yang, C. M.; Chiu, C. C.; Yang, C. H.; Hsu, S. L.; Ho, J. A. A. Phospholipid-functionalized mesoporous silica nanocarriers for selective photodynamic therapy of cancer. *Biomaterials* **2013**, *34*, 7462-7470.

(80) Ahern, R. J.; Hanrahan, J. P.; Tobin, J. M.; Ryan, K. B.; Crean, A. M. Comparison of fenofibrate-mesoporous silica drug-loading processes for enhanced drug delivery. *Eur. J Pharm. Sci.* **2013**, *50*, 400-409.

(81) Choi, Y. L.; Jaworski, J.; Seo, M. L.; Lee, S. J.; Jung, J. H. Controlled release using mesoporous silica nanoparticles functionalized with 18-crown-6 derivative. *J Mater. Chem.* **2011**, *21*, 7882-7885.

(82) Popova, M. D.; Szegedi, A.; Kolev, I. N.; Mihaly, J.; Tzankov, B. S.; Momekov, G. T.; Lambov, N. G.; Yoncheva, K. P. Carboxylic modified spherical mesoporous silicas as drug delivery carriers. *Int. J. Pharm.* **2012**, *436*, 778-785.

(83) Zhao, P.; Jiang, H.; Jiang, T.; Zhi, Z.; Wu, C.; Sun, C.; Zhang, J.; Wang, S. Inclusion of celecoxib into fibrous ordered mesoporous carbon for enhanced oral bioavailability and reduced gastric irritancy. *Eur. J Pharm. Sci.* **2012**, *45*, 639-647.

(84) Limnell, T.; Santos, H. A.; Makila, E.; Heikkila, T.; Salonen, J.; Murzin, D. Y.; Kumar, N.; Laaksonen, T.; Peltonen, L.; Hirvonen, J. Drug Delivery Formulations of Ordered and Nonordered Mesoporous Silica: Comparison of Three Drug Loading Methods. *J. Pharm. Sci.* **2011**, *100*, 3294-3306.

(85) Xia, X.; Zhou, C.; Ballell, L.; Garcia-Bennett, A. E. In vivo Enhancement in Bioavailability of Atazanavir in the Presence of Proton-Pump Inhibitors using Mesoporous Materials. *Chemmedchem* **2012**, *7*, 43-48.

(86) Van Speybroeck, M.; Mellaerts, R.; Mols, R.; Do Thi, T.; Martens, J. A.; Van Humbeeck, J.; Annaert, P.; Van den Mooter, G.; Augustijns, P. Enhanced absorption of the poorly soluble drug fenofibrate by tuning its release rate from ordered mesoporous silica. *Eur. J Pharm. Sci.* **2010**, *41*, 623-630.

(87) Kumar, D.; Chirravuri, S. V. S.; Shastri, N. R. Impact of surface area of silica particles on dissolution rate and oral bioavailability of poorly water soluble drugs: A case study with aceclofenac. *Int. J. Pharm.* **2014**, *461*, 459-468.

(88) Hu, Y.; Zhi, Z.; Zhao, Q.; Wu, C.; Zhao, P.; Jiang, H.; Jiang, T.; Wang, S. 3D cubic mesoporous silica microsphere as a carrier for poorly soluble drug carvedilol. *Micropor. Mesopor. Mat.* **2012**, *147*, 94-101.

(89) Kiekens, F.; Eelen, S.; Verheyden, L.; Daems, T.; Martens, J.; Van Den Mooter, G. Use of ordered mesoporous silica to enhance the oral bioavailability of ezetimibe in dogs. *J. Pharm. Sci.* **2012**, *101*, 1136-1144.

(90) van Speybroeck, M.; Mellaerts, R.; Thao Do, T.; Martens, J. A.; Van Humbeeck, J.; Annaert, P.; Van den Mooter, G.; Augustijns, P. Preventing Release in the Acidic Environment of the Stomach via Occlusion in Ordered Mesoporous Silica Enhances the Absorption of Poorly Soluble Weakly Acidic Drugs. *J. Pharm. Sci.* **2011**, *100*, 4864-4876.

(91) Balas, F.; Manzano, M.; Horcajada, P.; Vallet-Regi, M. Confinement and controlled release of bisphosphonates on ordered mesoporous silica-based materials. *J. Am. Chem. Soc.* **2006**, *128*, 8116-8117.

(92) Manzano, M.; Aina, V.; Arean, C. O.; Balas, F.; Cauda, V.; Colilla, M.; Delgado, M. R.; Vallet-Regi, M. Studies on MCM-41 mesoporous silica for drug delivery: Effect of particle morphology and amine functionalization. *Chem. Eng. J* **2008**, *137*, 30-37.

(93) Ambrogi, V.; Famiani, F.; Perioli, L.; Marmottini, F.; Di Cunzolo, I.; Rossi, C. Effect of MCM-41 on the dissolution rate of the poorly soluble plant growth regulator, the indole-3-butyric acid. *Micropor. Mesopor. Mat.* **2006**, *96*, 177-183.

(94) Clifford, N. W.; Iyer, K. S.; Raston, C. L. Encapsulation and controlled release of nutraceuticals using mesoporous silica capsules. *J Mater Chem* **2008**, *18*, 162-165.

(95) Mellaerts, R.; Jammaer, J. A. G.; Van Speybroeck, M.; Chen, H.; Van Humbeeck, J.; Augustijns, P.; Van den Mooter, G.; Martens, J. A. Physical state of poorly water soluble therapeutic molecules loaded into SBA-15 ordered mesoporous silica carriers: A case study with itraconazole and ibuprofen. *Langmuir* **2008**, *24*, 8651-8659.

(96) Izquierdo-Barba, I.; Sousa, E.; Doadrio, J. C.; Doadrio, A. L.; Pariente, J. P.; Martinez, A.; Babonneau, F.; Vallet-Regi, M. Influence of mesoporous structure type on the controlled

delivery of drugs: release of ibuprofen from MCM-48, SBA-15 and functionalized SBA-15. *J Sol-gel Sci. Techn.* **2009**, *50*, 421-429.

(97) Lu, J.; Li, Z. X.; Zink, J. I.; Tamanoi, F. In vivo tumor suppression efficacy of mesoporous silica nanoparticles-based drug-delivery system: enhanced efficacy by folate modification. *Nanomedicine: NBM* **2012**, *8*, 212-220.

(98) Liu, J. S.; Du, X. Z. pH- and competitor-driven nanovalves of cucurbit 7 uril pseudorotaxanes based on mesoporous silica supports for controlled release. *J Mater. Chem.* **2010**, *20*, 3642-3649.

(99) Patel, K.; Angelos, S.; Dichtel, W. R.; Coskun, A.; Yang, Y. W.; Zink, J. I.; Stoddart, J. F. Enzyme-responsive snap-top covered silica nanocontainers. *J Am. Chem. Soc.* **2008**, *130*, 2382-2383.

(100) Luo, Z.; Cai, K. Y.; Hu, Y.; Zhao, L.; Liu, P.; Duan, L.; Yang, W. H. Mesoporous Silica Nanoparticles End-Capped with Collagen: Redox-Responsive Nanoreservoirs for Targeted Drug Delivery. *Angew. Chem. Int. Edit.* **2011**, *50*, 640-643.

(101) Halas, N. J. Nanoscience under glass: The versatile chemistry of silica nanostructures. *ACS Nano* **2008**, *2*, 179-183.

(102) Garcia-Bennett, A. E. Synthesis, toxicology and potential of ordered mesoporous materials in nanomedicine. *Nanomedicine: NBM* **2011**, *6*, 867-877.

(103) Raymond Rowe, P. S., Sian Owen *Handbook of Pharmaceutical Excipients*; 5th ed.; Pharmaceutical Press & American Pharmacists Association, 2006.

(104) He, Q.; Zhang, Z.; Gao, Y.; Shi, J.; Li, Y. Intracellular Localization and Cytotoxicity of Spherical Mesoporous Silica Nano- and Microparticles. *Small* **2009**, *5*, 2722-2729.

(105) Lin, Y.-S.; Haynes, C. L. Impacts of Mesoporous Silica Nanoparticle Size, Pore Ordering, and Pore Integrity on Hemolytic Activity. *J Am. Chem. Soc.* **2010**, *132*, 4834-4842.

(106) Napierska, D.; Thomassen, L. C. J.; Rabolli, V.; Lison, D.; Gonzalez, L.; Kirsch-Volders, M.; Martens, J. A.; Hoet, P. H. Size-Dependent Cytotoxicity of Monodisperse Silica Nanoparticles in Human Endothelial Cells. *Small* **2009**, *5*, 846-853.

(107) Vallhov, H.; Gabrielsson, S.; Stromme, M.; Scheynius, A.; Garcia-Bennett, A. E. Mesoporous silica particles induce size dependent effects on human dendritic cells. *Nano Lett.* **2007**, *7*, 3576-3582.

(108) Hartono, S. B.; Qiao, S. Z.; Jack, K.; Ladewig, B. P.; Hao, Z.; Lu, G. Q. Improving Adsorbent Properties of Cage-like Ordered Amine Functionalized Mesoporous Silica with Very Large Pores for Bioadsorption. *Langmuir* **2009**, *25*, 6413-6424.

(109) Veronese, F. M.; Pasut, G. PEGylation, successful approach to drug delivery. *Drug Discov. Today* **2005**, *10*, 1451-1458.

(110) Di Pasqua, A. J.; Sharma, K. K.; Shi, Y.-L.; Toms, B. B.; Ouellette, W.; Dabrowiak, J. C.; Asefa, T. Cytotoxicity of mesoporous silica nanomaterials. *J Inorg. Biochem.* **2008**, *102*, 1416-1423.

(111) Lee, S.; Yun, H.-S.; Kim, S.-H. The comparative effects of mesoporous silica nanoparticles and colloidal silica on inflammation and apoptosis. *Biomaterials* **2011**, *32*, 9434-9443.

(112) Yu, T.; Malugin, A.; Ghandehari, H. Impact of Silica Nanoparticle Design on Cellular Toxicity and Hemolytic Activity. *ACS Nano* **2011**, *5*, 5717-5728.

(113) Lee, S.; Kim, M. S.; Lee, D.; Kwon, T. K.; Khang, D.; Yun, H. S.; Kim, S. H. The comparative immunotoxicity of mesoporous silica nanoparticles and colloidal silica nanoparticles in mice. *Int. J Nanomed.* **2013**, *8*, 147-158.

(114) Souris, J. S.; Lee, C.-H.; Cheng, S.-H.; Chen, C.-T.; Yang, C.-S.; Ho, J.-a. A.; Mou, C.-Y.; Lo, L.-W. Surface charge-mediated rapid hepatobiliary excretion of mesoporous silica nanoparticles. *Biomaterials* **2010**, *31*, 5564-5574.

Chapter 3

Research Methodology

The main objective of this thesis is to conduct a comprehensive study for enhancing the aqueous solubility of hydrophobic drugs (such as anticancer drug - curcumin) using mesoporous silica nanoparticles and evaluating the influence of surface functionalization on solubility, drug release and cytotoxicity.

The first part of this thesis focuses on developing a technique to adjust the pore size of mesoporous silica nanoparticles (MSNs) at angstrom scale of 2-4 and 4-6 Å using two different silica precursors – tetraethoxyorthosilicate and tetramethoxyorthosilicate respectively. The series of MSNs materials obtained using the above process were thoroughly characterised and further a hydrophobic anticancer drug was encapsulated in them to study the influence of pore size on solubility.

The second part of the thesis investigates the application of mesoporous silica nanoparticles as drug carrier system by encapsulating hydrophobic anticancer drug. The influence of mesoporous silica nanoparticles on enhancing the solubility, drug release and cytotoxicity was evaluated in comparison to pure drug.

The third part focuses on the influence of surface functionalized mesoporous silica nanoparticles on cytotoxicity by encapsulating hydrophobic anticancer drug. Effect of surface charge and hydrophobicity on cytotoxicity was studied by conducting cell viability studies, cell cycle analysis, cell apoptosis study and reactive oxygen species generation studies. This part elucidates the role of surface functionalization in designing a effective drug carrier system.

The fourth part of the thesis focuses on the influence of surface functionalized mesoporous silica nanoparticles on solubility and drug release by encapsulating hydrophobic anticancer drug. Interaction between the drug molecules and surface functionalized species was studied to evaluate its role in modulating the solubility and drug release which would help in selecting appropriate drug carrier system.

Chapter 4

Stepwise Pore Size Reduction of Ordered Nanoporous Silica Materials at Angstrom Precision

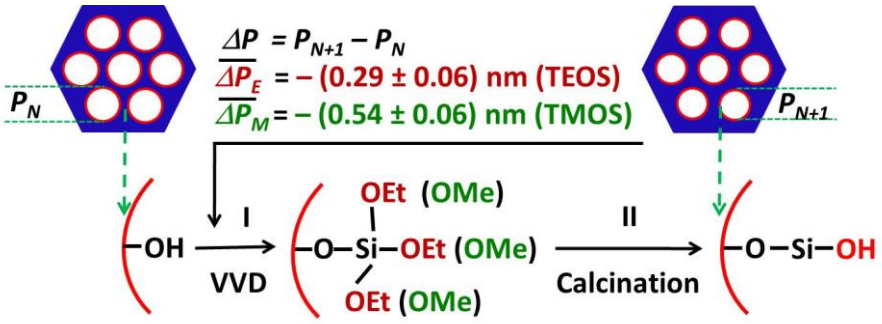

A facile vacuum-assisted vapor deposition process has been developed to control the pore size of ordered mesoporous silica materials in a stepwise manner with angstrom precision, providing an unprecedented paradigm for screening a designer hydrophobic drug nanocarrier with optimized pore diameter to maximize drug solubility.

Chapter 4 is included as it appears in Journal of the American Chemical Society, 2013,135, 8444-8447.

JACS
JOURNAL OF THE AMERICAN CHEMICAL SOCIETY

Communication

pubs.acs.org/JACS

Stepwise Pore Size Reduction of Ordered Nanoporous Silica Materials at Angstrom Precision

Siddharth Jambhrunkar,[†] Meihua Yu,[†] Jie Yang,[†] Jun Zhang,[†] Abhijit Shrotri,[†] Liliana Endo-Munoz,[‡] Joël Moreau,[§] Gaoqing Lu,[†] and Chengzhong Yu*[,†]

[†]ARC Centre of Excellence for Functional Nanomaterials and Australian Institute for Bioengineering and Nanotechnology, The University of Queensland, Brisbane, QLD 4072, Australia

[‡]Diamantina Institute, Princess Alexandra Hospital, Ipswich Road, Brisbane, QLD 4102, Australia

[§]Ecole Nationale Supérieure de Chimie de Montpellier, 34296 Montpellier CEDEX 5, France

Supporting Information

ABSTRACT: A facile vacuum-assisted vapor deposition process has been developed to control the pore size of ordered mesoporous silica materials in a stepwise manner with angstrom precision, providing an unprecedented paradigm for screening a designer hydrophobic drug nanocarrier with optimized pore diameter to maximize drug solubility.

Since the discovery of MCM-41[1] and SBA-15,[2] ordered mesoporous silica materials have attracted ever-increasing attention because of their potential applications in many fields.[3] The uniform mesopores and adjustable pore sizes are important characteristics of mesoporous materials that are critically important for the controlled immobilization and release behavior of guest molecules,[4] catalytic reaction performance in confined nanospaces,[5] controlled release of hydrophobic drugs,[4,6] and use as nanocarriers for water-insoluble drugs.[7] To date, much effort has been devoted to controlling the pore size of ordered mesoporous silica materials. Generally, the pore size can be increased using post-synthesis methods or the addition of swelling agents[2] or by varying the structure-directing template.[8] Alternatively, the pore size can be reduced by the grafting method,[9] metal−organic chemical vapor deposition,[10] or atomic layer deposition (ALD).[11] Of these, ALD has been widely used to modify mesoporous silica materials with another oxide phase (e.g., TiO_2, HfO_2),[11b−d] showing pore size reduction at the atomic scale. However, it is difficult to achieve a constant pore size reduction in each cycle. Moreover, unlike zeolites or metal−organic frameworks, whose pore sizes can be designed at angstrom precision for size-selective applications,[12] it has been a big challenge to achieve such precise control over the pore sizes of ordered mesoporous silica materials since their discovery, especially over a wide mesopore size range and in a reproducible manner.

Up to 40% of new chemical drugs emerging from high-throughput screening processes are poorly water-soluble, posing the challenge of improving their solubility and hence their bioavailability.[13] Various approaches to address this issue have been studied,[14] among which reducing the hydrophobic drug particle size[15] is an efficient one, as reflected by the Ostwald−Freundlich equation.[16] However, methods of reducing drug particle sizes find limitations in downsizing drug particle sizes below 20 nm, a regime in which a dramatic increase in solubility is expected. Ordered mesoporous silica materials provide an adjustable confined nanospace, and hence, the size of the drug loaded inside can be limited. By confining the hydrophobic drug indole-3-butyric acid into MCM-41 with a pore size of 3.31 nm, its solubility was increased ca. 2-fold relative to the drug alone.[7c] Surprisingly, this is a rare case showing the influence of nanoconfinement on the solubility of drugs. It is not known whether this concept can be generally applied to other hydrophobic drugs. Importantly, to our knowledge, the relationship between the pore size of the host mesoporous material and the solubility of the loaded drug has not been reported. We hypothesized that there exists an optimized pore size displaying the highest solubility for a given hydrophobic drug [see Influence of Pore Size on Solubility in the Supporting Information (SI)]. To test this hypothesis, it was necessary to design a series of mesoporous silica materials with precisely controlled pore sizes and encapsulate the drug in them.

Herein we report a facile vacuum-assisted vapor deposition (VVD) approach for reducing the pore size of ordered mesoporous silica materials in a stepwise and precise fashion (Figure 1). The step size was adjustable in increments of 0.29 ± 0.06 nm using tetraethoxyorthosilicate (TEOS) or 0.54 ± 0.06 nm using tetramethoxyorthosilicate (TMOS) as the silica precursor. A surface-chemistry switching mechanism is proposed (Figure 1A). By means of the surface silanols at the pore surface, the TEOS or TMOS vapor molecules are anchored on the pore surface by VVD (step I), which is followed by calcination (step II) to complete one cycle. Upon completion of one cycle, the pore diameter is reduced, and the silanols are regenerated and can be used for a subsequent cycle. This approach was tested using two ordered mesoporous silica materials with different initial pore sizes, SBA-15[2] and MCM-41[1] (Figure 1B). In consecutive cycles, the pore size reduction was consistent for both materials and/or silica precursors. By encapsulation of the hydrophobic drug curcumin in the series of MCM-41 materials with controlled pore sizes, a pore size−solubility function was obtained that shows an optimal pore size

Received: March 9, 2013
Published: May 13, 2013

dx.doi.org/10.1021/ja402463h | *J. Am. Chem. Soc.* 2013, 135, 8444−8447

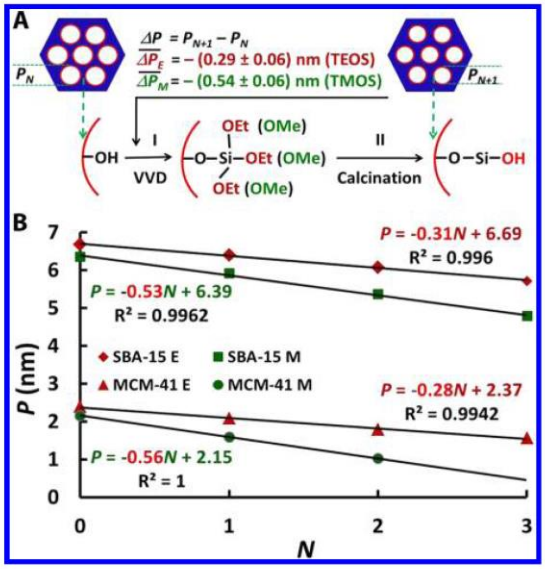

Figure 1. (A) Scheme demonstrating the VVD approach for stepwise reduction of the pore sizes of ordered mesoporous silica materials over a precise range using TEOS or TMOS (abbreviated as "E" or "M", respectively). N is the cycle number, and P_N and P_{N+1} are the pore diameters before and after cycle N, respectively. ΔP denotes the pore size change after one VVD cycle. $\overline{\Delta P}$ denotes the mean pore size reduction and is expressed as the mean ± standard deviation after three cycles, except for MCM-41 with TMOS, where only two cycles were included in the linear regression. (B) Variation of the pore diameter, P, as a function of N for both SBA-15 and MCM-41 materials. R^2 is the regression coefficient.

(1.70 nm) where curcumin possesses the highest solubility (4.5 times higher than for the drug alone).

SBA-15 and MCM-41 were prepared according to published methods[17] with slight variations (see the Experimental Section in the SI). To adjust the pore size, 0.8 g of calcined SBA-15 or MCM-41 material was placed in a home-designed VVD apparatus to undergo the VVD process (Figure S1 in the SI). The VVD process was performed by exposure of the mesoporous silica material to either TEOS or TMOS for 24 h at 60 °C (step I) followed by calcination (step II) (Figure 1A). The samples obtained in one VVD cycle are denoted as sample-D*N*-E/M and sample-C*N*-E/M, where "sample" is SBA-15 or MCM-41, "D" refers to the deposition step, and "C" refers to the calcination step (*N*, E, and M are defined in Figure 1).

The X-ray diffraction (XRD) patterns of SBA-15-C*N*-E (N = 0–3) are shown in Figure S2A. For SBA-15-C0-E before VVD treatment, three well-resolved diffractions appear at 2θ = 0.90, 1.56, and 1.81° with a reciprocal d-spacing ratio close to $1:\sqrt{3}:2$, which can be indexed as the 100, 110, and 200 reflections of an ordered two-dimensional hexagonal mesostructure (*p6mm*). From the intense (100) peak, a d_{100} spacing of 9.81 nm was calculated, corresponding to a unit cell parameter (a) of 11.33 nm (Table S1 in the SI). The XRD patterns for SBA-15-C*N*-E after successive VVD cycles (N = 1–3) are similar to that of SBA-15-C0-E, demonstrating retention of the ordered hexagonal mesostructure. Moreover, the positions of the three diffractions are similar for the four materials. In addition, a gradual increase in the ratio of intensity of 200 to 110 peaks can be observed, suggesting a slight increase in wall thickness in each VVD cycle.[18]

The N_2 adsorption–desorption isotherms for SBA-15-C*N*-E (N = 0–3) are typical type-IV isotherms with a steep capillary condensation step occurring at a relative pressure (P/P_0) range of 0.7–0.8, characteristic of ordered mesoporous materials with large and uniform mesopores (Figure S3A). The pore size variation in SBA-15-C*N*-E can be clearly seen in their pore size distribution curves calculated from the adsorption branch using the Barrett–Joyner–Halenda (BJH) model after Gaussian fitting (Figure S2B). The pore sizes were calculated to be 6.67, 6.40, 6.07, and 5.71 nm for N = 0–3, respectively, and the pore size distribution curve was narrow even after three VVD cycles. After linear regression analysis, the equation $P = -0.31N + 6.69$) with a regression coefficient of R^2 = 0.9960 was obtained (Figure 1B), indicating a high statistical significance of the VVD process to achieve fine control over the pore size. The pore sizes as well as surface areas and pore volumes of SBA-15-C*N*-E (N = 0–3) are summarized in Table S1 for comparison.

To understand why the pore size was precisely reduced after every cycle in the VVD process in a stepwise manner, Fourier transform IR (FTIR) analysis of the SBA-15 material treated in each step of the three cycles was performed. To show the surface chemistry changes clearly, only regions of interest are displayed in Figure 2. Before the VVD process, SBA-15-C0-E exhibited one peak at 3745 cm^{-1} (Figure 2A) assigned to

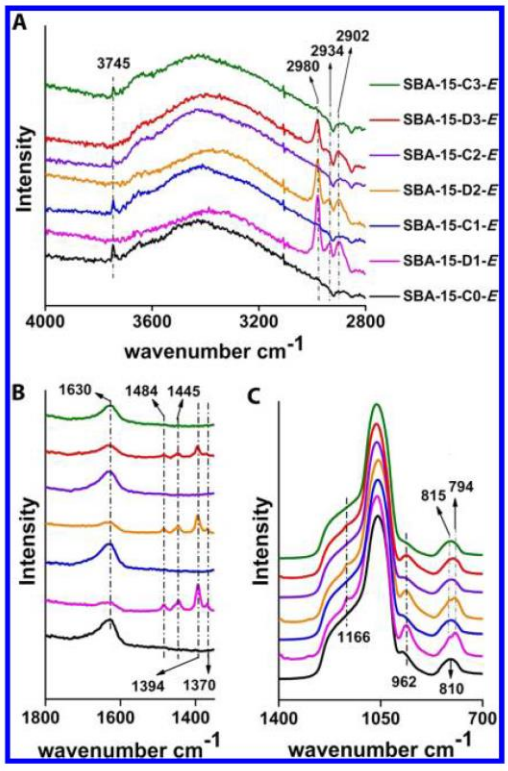

Figure 2. FTIR spectra of the SBA-15 sample before, during, and after treatment with the VVD process for three cycles using TEOS as the silica precursor. Samples are named as SBA-15-D*N*-E and SBA-15-C*N*-E, where D denotes the deposited sample after step I in the cycle, C denotes the calcined sample after step II in the cycle, N denotes the cycle number, and E denotes TEOS.

dx.doi.org/10.1021/ja402463h | J. Am. Chem. Soc. 2013, 135, 8444–8447

isolated silanols [ν(O−H)].[19] After the first deposition step (SBA-15-D1-E), this peak could not be observed. Instead, a group of peaks at 2902, 2934, and 2980 cm^{-1} appeared, which can be assigned to ν(C−H) of unhydrolyzed ethoxy groups (Si−OCH$_2$CH$_3$).[19c] After the first calcination step (SBA-15-C1-E), the peaks assigned to ethoxy groups disappeared, and the peak at 3745 cm^{-1} associated with surface silanols was regenerated. The above results indicate that in one VVD cycle, the surface silanols are "switched off" and ethoxy groups are "switched on" in the deposition step and then the silanols are "switched on" and the ethoxy groups are "switched off" in the calcination step (see Figure 1A). Moreover, the "on/off" surface chemistry was repeatedly observed over three consecutive cycles.

The surface chemistry switching mechanism was further confirmed by the spectra shown in Figure 2B,C. The bands associated with ethoxy groups at 1166 [ρ(CH$_3$)], 1370 [ω(CH$_2$)], 1394 [δ_s(CH$_3$)], 1445 [δ_a'(CH$_2$)] and 1484 cm^{-1} [δ_a(CH$_3$) + δ_a(CH$_2$)] were observed only after each deposition step. The band at 962 cm^{-1} (Figure 2C) is the characteristic peak for ρ(CH$_3$), which overlaps with the band of silanols (observed after calcination) with relatively weaker intensity.[20] The band observed at 810 cm^{-1} after each calcination step (Figure 2C) can be indexed to symmetric Si−O−Si stretching [ν_s(Si−O−Si)].[19a] After deposition, only two peaks at 794 [ν(Si−O)] and 815 cm^{-1} [δs(Si−O−C)] indexed to the nonreacted (Si−OCH$_2$CH$_3$) groups were observed.[21] The intensity of the band associated with physiosorbed water at 1630 cm^{-1} was higher when Si−OH was "switched on" and lower when Si−OH was "switched off", consistent with the hydrophilicity/hydrophobicity change of the pore walls and the surface chemistry switching mechanism.

The VVD process was further applied to MCM-41 materials using TEOS as the silica precursor. Both XRD and nitrogen sorption results showed that the ordered hexagonal mesostructure with narrow pore size distribution was retained after three VVD cycles (Figures S3 and S4). FTIR spectra (Figure S5) demonstrated the mechanism proposed in Figure 1 to be reproducible for both SBA-15 and MCM-41 materials. After linear regression, the equation $P = -0.28N + 2.37$ with R^2 = 0.9942 was obtained (Figure 1B), confirming that our VVD process can be applied to both SBA-15 and MCM-41 to achieve a stepwise pore size reduction in a precise range of 0.29 ± 0.06 nm per step. The VVD process was repeated on freshly synthesized SBA-15 and MCM-41, further demonstrating its reproducibility (see Reproducibility of VVD process in the SI along with Figures S6−S8 and Table S2).

The VVD process was further conducted on SBA-15 and MCM-41 materials using TMOS as the silica precursor. The XRD patterns for SBA-15-C*N*-M (Figure S9A) and MCM-41-C*N*-M (Figure S10A) showed that the ordered hexagonal structure was retained after each VVD cycle. N_2 adsorption−desorption isotherms for SBA-15-C*N*-M (N = 0−3) and MCM-41-C*N*-M (N = 0−2) (Figure S11) were typical type-IV isotherms, similar to those obtained for SBA-15-C*N*-E (N = 0−3) and MCM-41-C*N*-E (N = 0−3). The pore sizes, surface areas, and pore volumes of SBA-15-C*N*-M (N = 0−3) and MCM-41-C*N*-M (N = 0−2) are summarized in Table S1. For MCM-41-C3-M, the mesopores were nearly blocked, and it was very difficult to detect the pore size using the BJH model because the pore size was in microporous range. Hence, the pore size distribution curve for MCM-41 material was calculated for only two VVD cycles.

The pore size distribution data for SBA-15-C*N*-M (N = 0−3) and MCM-41-C*N*-M (N = 0−2) are shown in Figures S9B and S10B, respectively. After linear regression analysis, the equations $P = -0.53N + 6.39$ (R^2 = 0.9962) and $P = -0.56N + 2.15$ (R^2 = 1) were obtained for the SBA-15 and MCM-41 groups, respectively, indicating high statistical significance (Figure 1B). Using TMOS in the VVD process led to a stepwise pore size reduction of 0.54 ± 0.06 nm per step for SBA-15 and MCM-41. FTIR analysis was performed for SBA-15-C*N*-M and MCM-41-C*N*-M, and surface chemistry "on/off" switching similar to that for SBA-15-C*N*-E and MCM-41-C*N*-E was observed (Figures S12 and S13).

To understand the difference in the pore size reduction steps using TEOS (0.29 ± 0.06 nm) and TMOS (0.54 ± 0.06 nm) in our VVD process, the weight change upon deposition (step I) was carefully monitored for SBA-15 using TEOS as the silica precursor. The weight gains observed for SBA-15-D*N*-E (N = 1−3) are listed in Table S3. After each deposition step, the number of TEOS molecules deposited on the internal surface of SBA-15 had a constant value of 0.9 nm^{-2}. Because TEOS has a molecular size of 0.93 nm,[22] the surface coverage constant of 0.9 nm^{-2} is consistent with monolayer-like deposition behavior on the wall surface (Figure S14A). After calcination (step II) to convert −Si(OEt)$_3$ to Si−OH, the newly generated Si−OH must be distributed sparsely because of its smaller size compared with −Si(OEt)$_3$. It is noted that a densely packed Si−OH monolayer theoretically would generate a pore size reduction of 0.62 nm (Figure S14C). The sparse distribution of Si−OH in our model (Figure S14B) leads to the observed pore size reduction of 0.29 ± 0.06 nm. Because TMOS molecules are smaller than TEOS molecules, the number of TMOS molecules deposited on the internal surface of SBA-15 during step I should be higher (Figure S14A), leading to relatively higher density of newly generated Si−OH after step II, which results in a larger pore size reduction step of 0.54 ± 0.06 nm.

Finally, the series of MCM-41 nanoporous materials with precisely controlled pore sizes were utilized to confine the hydrophobic drug curcumin in order to study the pore size−solubility relationship. As shown in Figure 3, pure curcumin has a very low water solubility of 0.31 μg/mL. Curcumin encapsulated in pristine MCM-41 with a pore size of 2.22 nm had an improved solubility of 0.53 μg/mL. The curcumin solubility further increased with decreasing pore size, reaching a

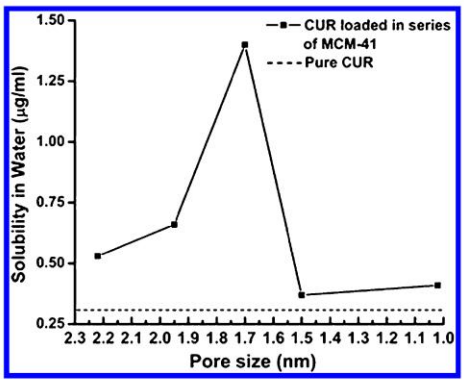

Figure 3. Correlation between pore size and curcumin solubility in water after loading of curcumin into a series of calcined MCM-41 materials with precisely controlled pore sizes.

maximum of 1.40 μg/mL (4.5 times of pure curcumin) at the optimal pore size of 1.70 nm. However, the curcumin solubility diminished significantly when the pore size was further decreased from 1.70 to 1.50 and 1.02 nm. Our experimental observations are in good accordance with the theoretical predictions (see the SI).

In conclusion, we have developed a novel VVD approach to achieve stepwise reductions in the pore size of mesoporous silica materials at angstrom precision. The pore size−solubility relationship has been established, allowing a mesoporous material with an optimized pore size displaying maximized drug solubility to be identified. With our discovery, the pore sizes of ordered mesoporous materials can be adjusted over a broad regime with a precision that has not been achieved before, offering new materials for advanced pore-size-dependent applications.

■ ASSOCIATED CONTENT

Supporting Information

Experimental methods and other characterizations. This material is available free of charge via the Internet at http://pubs.acs.org.

■ AUTHOR INFORMATION

Corresponding Author

c.yu@uq.edu.au

Notes

The authors declare no competing financial interest.

■ ACKNOWLEDGMENTS

This work was supported by the Australian Research Council.

■ REFERENCES

(1) Kresge, C. T.; Leonowicz, M. E.; Roth, W. J.; Vartuli, J. C.; Beck, J. S. *Nature* **1992**, *359*, 710.
(2) Zhao, D. Y.; Feng, J. L.; Huo, Q. S.; Melosh, N.; Fredrickson, G. H.; Chmelka, B. F.; Stucky, G. D. *Science* **1998**, *279*, 548.
(3) (a) Vallet-Regi, M.; Balas, F.; Arcos, D. *Angew. Chem., Int. Ed.* **2007**, *46*, 7548. (b) Somorjai, G. A.; Frei, H.; Park, J. Y. *J. Am. Chem. Soc.* **2009**, *131*, 16589.
(4) Balas, F.; Manzano, M.; Horcajada, P.; Vallet-Regi, M. *J. Am. Chem. Soc.* **2006**, *128*, 8116.
(5) (a) Ying, J. Y.; Mehnert, C. P.; Wong, M. S. *Angew. Chem., Int. Ed.* **1999**, *38*, 56. (b) Nandi, M.; Mondal, J.; Sarkar, K.; Yamauchi, Y.; Bhaumik, A. *Chem. Commun.* **2011**, *47*, 6677.
(6) Mellaerts, R.; Jammaer, J. A. G.; Van Speybroeck, M.; Chen, H.; Van Humbeeck, J.; Augustijns, P.; Van den Mooter, G.; Martens, J. A. *Langmuir* **2008**, *24*, 8651.
(7) (a) Lu, J.; Liong, M.; Zink, J. I.; Tamanoi, F. *Small* **2007**, *3*, 1341. (b) Lu, J.; Liong, M.; Li, Z. X.; Zink, J. I.; Tamanoi, F. *Small* **2010**, *6*, 1794. (c) Ambrogi, V.; Famiani, F.; Perioli, L.; Marmottini, F.; Di Cunzolo, I.; Rossi, C. *Microporous Mesoporous Mater.* **2006**, *96*, 177.
(8) Yu, C. Z.; Fan, J.; Tian, B. Z.; Stucky, G. D.; Zhao, D. Y. *J. Phys. Chem. B* **2003**, *107*, 13368.
(9) Zhao, X. S.; Lu, G. Q. M.; Hu, X. *Chem. Commun.* **1999**, 1391.
(10) Zhang, Y.; Lam, F. L. Y.; Hu, X. J.; Yan, Z. F. *Chem. Commun.* **2008**, 5131.
(11) (a) Berland, B. S.; Gartland, I. P.; Ott, A. W.; George, S. M. *Chem. Mater.* **1998**, *10*, 3941. (b) Mahurin, S.; Bao, L.; Yan, W.; Liang, C.; Dai, S. *J. Non-Cryst. Solids* **2006**, *352*, 3280. (c) Pagan-Torres, Y. J.; Gallo, J. M. R.; Wang, D.; Pham, H. N.; Libera, J. A.; Marshall, C. L.; Elam, J. W.; Datye, A. K.; Dumesic, J. A. *ACS Catal.* **2011**, *1*, 1234. (d) Dendooven, J.; Goris, B.; Devloo-Casier, K.; Levrau, E.; Biermans, E.; Baklanov, M. R.; Ludwig, K. F.; Van der Voort, P.; Bals, S.; Detavernier, C. *Chem. Mater.* **2012**, *24*, 1992.
(12) Li, J. R.; Kuppler, R. J.; Zhou, H. C. *Chem. Soc. Rev.* **2009**, *38*, 1477.
(13) Lipinski, C. *Am. Pharm. Rev.* **2002**, *5*, 82.
(14) Chadha, R.; Kapoor, V. K.; Thakur, D.; Kaur, R.; Arora, P.; Jain, D. V. S. *J. Sci. Ind. Res.* **2008**, *67*, 185.
(15) Rabinow, B. E. *Nat. Rev. Drug Discovery* **2004**, *3*, 785.
(16) Ostwald, W. *Z. Phys. Chem., Stoechiom. Verwandtschaftsl.* **1900**, *34*, 495.
(17) (a) Pan, D. H.; Yuan, P.; Zhao, L. Z.; Liu, N. A.; Zhou, L.; Wei, G. F.; Zhang, J.; Ling, Y. C.; Fan, Y.; Wei, B. Y.; Liu, H. Y.; Yu, C. Z.; Bao, X. *J. Chem. Mater.* **2009**, *21*, 5413. (b) Yang, S.; Zhao, L. Z.; Yu, C. Z.; Zhou, X. F.; Tang, J. W.; Yuan, P.; Chen, D. Y.; Zhao, D. Y. *J. Am. Chem. Soc.* **2006**, *128*, 10460.
(18) Kozlova, S. A.; Kirik, S. D. *Microporous Mesoporous Mater.* **2010**, *133*, 124.
(19) (a) Muroya, M. *Colloids Surf., A* **1999**, *157*, 147. (b) Pan, D. H.; Zhao, L. Z.; Qian, K.; Tan, L.; Zhou, L.; Zhang, J.; Huang, X. D.; Fan, Y.; Liu, H. Y.; Yu, C. Z.; Bao, X. J. *J. Mater. Res.* **2011**, *26*, 804. (c) Tejedor-Tejedor, M. I.; Paredes, L.; Anderson, M. A. *Chem. Mater.* **1998**, *10*, 3410.
(20) Zhang, J.; Yu, M. H.; Yuan, P.; Wang, H. N.; Qian, K.; Tan, L.; Wang, Y. H.; Yu, C. Z. *J. Mater. Res.* **2010**, *25*, 648.
(21) (a) Velasco-Santos, C.; Martinez-Hernandez, A. L.; Brostow, W.; Castaño, V. M. *J. Nanomater.* **2011**, No. 928659. (b) Bourgeat-Lami, E.; Tissot, I.; Lefebvre, F. *Macromolecules* **2002**, *35*, 6185.
(22) Wróbel, A. M.; Walkiewicz-Pietrzykowska, A.; Stasiak, M.; Kulpiúski, *J. Chem. Vap. Deposition* **1996**, *2*, 285.

Stepwise pore size reduction of ordered nanoporous silica materials at angstrom precision

Siddharth Jambhrunkar[a], Meihua Yu[a], Jie Yang[a], Jun Zhang[a], Abhijit Shrotri[a], Liliana Endo-Munoz[b], Joël Moreau[c] , Gaoqing Lu[a], Chengzhong Yu*[a]

[a] ARC Centre of Excellence for Functional Nanomaterials and Australian Institute for Bioengineering and Nanotechnology, The University of Queensland, Brisbane, QLD 4072, Australia.

[b] Diamantina Institute, Princess Alexandra Hospital, Ipswich Rd, Brisbane QLD 4102, Australia

[c] CNRS UMR 5253, Ecole Nationale Supérieure de Chimie, 34296 Montpellier Cedex 5, France

Influence of pore size on solubility

In general, the solubility of a particle is related to both its bulk molecular property and interfacial property, which can be described by the Ostwald-Freundlich equation (Eq. 1),[1] according to which a decrease in particle size results in an increase in saturation solubility of the drug.

$$S/S_0 = \exp(2\gamma M / r\rho RT) \quad \text{Eq. 1,}$$

where S is the solubility of a spherical particle with a radius of r, S_0 is the equilibrium solubility, R is the universal gas constant, T is the temperature, M is the molecular weight, ρ is the density and γ is the solid-liquid interfacial tension.

When the drug molecules are loaded in mesoporous materials after solvent evaporation, their particle sizes are limited by the pore sizes and adjustable through tuning the pore sizes of mesoporous materials (Scheme S1). Therefore, the Ostwald-Freundlich equation can be qualitatively expressed by the relationship between solubility and pore size. When the pore size is decreased from Scheme S1A to S1B, the drug crystal size is reduced accordingly, leading to enhanced solubility as predicted by Equation 1. However, when the pore size is further decreased and approaching the molecular size of the selected drug, the steric hindrance and the interaction between the pore surface and drug molecule will play an important role to counteract the solubility enhancement effect. When the pore size is smaller than the size of drug molecules for them to enter (Scheme S1C), the solubility under such circumstances should be similar to a bulk drug solution. It is hypothesized that there should be an optimized pore size where the drug solubility is maximized. We will test this theory in this work.

It is noted that in this approach, the Ostwald-Freundlich equation cannot be used for quantitative prediction. Firstly, there is no method available to precisely determine γ of a given molecule. Secondly, the equation is applied on an ideal spherical model. However, the shape of nanoparticles inside the mesopores is difficult to determine. Thirdly, the crystallization behavior of one drug and the drug-pore surface interaction is case-specific. Therefore, the optimised pore size to achieve the

maximised drug solubility should be experimentally determined, relying on designing a series of mesoporous silica materials with precisely controlled pore sizes in a very narrow range.

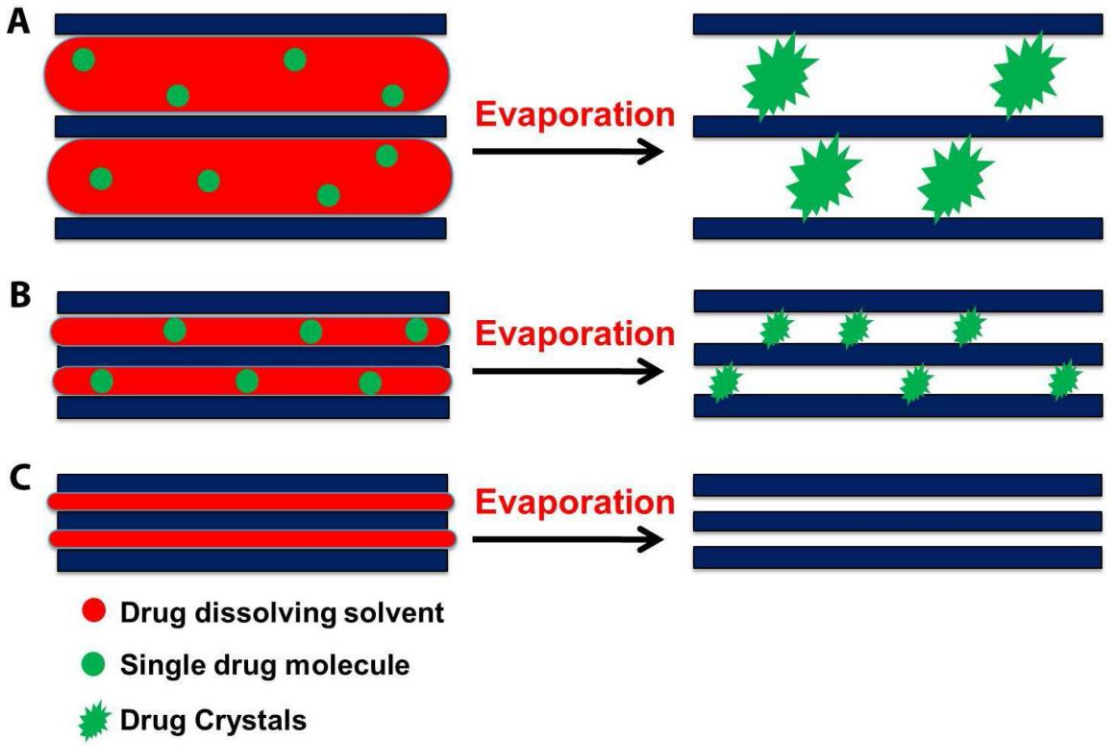

Scheme S1. A scheme demonstrating the influence of pore size on drug crystal size during the drug encapsulation process. The sizes of objects are not to scale.

Experimental Section

Chemicals

Tetraethylorthosilicate (TEOS), Tetramethoxyorthosilicate (TMOS), Cetyl trimethylammonium bromide (CTAB), polyoxyethylene-polyoxypropylene-polyoxyethylene block copolymer (PEO_{20}-PPO_{70}-PEO_{20}, known as Pluronic®P123), Sodium lauryl sulphate (SLS) and Curcumin were purchased from Sigma-Aldrich. Reagent grade sodium hydroxide (NaOH) and hydrochloric acid (HCl) were received from ChemSupply and Ajax Finochem Pty Ltd, respectively. Methanol was purchased from RCI Labscan Ltd.

Characterization

X-ray diffraction (XRD) patterns of SBA-15 and MCM-41 materials were recorded on a German Bruker D8 X-ray diffractometer with Ni-filtered Cu Kα radiation (λ = 1.5406 Å). The XRD patterns were obtained at 40 kV and 30 mA with a step size of 0.01°. Nitrogen adsorption-desorption isotherms were measured at -196°C by using a Micromeritics Tristar II 3020 system. The samples were degassed at 200°C overnight on a vacuum line. The Brunauer–Emmett–Teller (BET) method was utilized to calculate the specific surface areas. The pore size distribution curves were derived

from the adsorption branches of the isotherms using the Barrett–Joyner–Halanda (BJH) method after gaussian fitting. The total pore volume was calculated from the amount adsorbed at a maximum relative pressure (P/P_0). Fourier transform infrared (FTIR) spectra were collected with ThermoNicolet Nexus 6700 FTIR spectrometer equipped with Diamond ATR (attenuated total reflection) Crystal. For each spectrum, 128 scans were collected at a resolution of 4 cm^{-1} over the range 400–4000cm^{-1}. Curcumin concentration was determined using UV-VIS spectrophometer (Shimadzu UV-2450).

Synthesis

MCM-41 material was synthesized using the method reported by Yang et al.[2] with slight modifications. In a typical synthesis, 1.0 g of CTAB was dissolved in 480 g of deionized water with 3.5 mL of NaOH (2 M) under stirring at 80 °C. Then, 6.7 mL of TEOS was added into the mixture and kept under continuous stirring for an additional 2 h. The resultant product was collected by filtration and dried at room temperature. The surfactant templates were removed by calcination at 550 °C for 5 h.

SBA-15 was synthesized according to the procedure described by Pan *et al*.[3] with slight modification as described below. 2 g of P123 was dissolved in 2.0 M HCl aqueous solution, followed by addition of 4.16 g of TEOS under stirring at 38 °C. After stirring for 24 h at 38 °C, the resulting white precipitate was filtered. The product was mixed with 40 g of deionized water and the pH was adjusted to 1.65 using 1 M HCl. The mixture was transferred into an autoclave for hydrothermal treatment at 130 °C for 24 h. The as-synthesized product was collected by filtration, washed with deionized water and dried in air. The dried material was subjected to calcination at 550 °C for 5 h to remove the surfactant template.

The home-made VVD apparatus is shown in Figure S1, which consists of an upper chamber (custom made glass crucible with sintered glass disc of G4 porosity) and a bottom chamber (a glass cylinder). The two parts are attached together to form a VVD apparatus. The SBA-15 or MCM-41 material (0.8 g) was held on the porous disc and TEOS or TMOS was placed in the bottom chamber. The VVD apparatus is placed in the vacuum oven (175 Torr) at 60 °C for 24 h. TEOS or TMOS vapour molecules can only pass through the porous disc and the mesoporous silica placed on the top of the disc. The vacuum (175 Torr) helps in continuous contact between mesoporous silica and TEOS or TMOS vapour generated from the bottom chamber, so that TEOS or TMOS molecules can be adsorbed on the silica surface. After 24 h of the VVD process, the mesoporous silica materials adsorbed with TEOS or TMOS were calcined at 550 °C for 5 h.

SBA-15 and MCM-41 material was weighed before and after the deposition step I to obtain the weight gain occurring due to the deposition of the silica precursor in deposition step I. Using the weight gain, number of silica precursor molecules adsorbed on per square nm area of silica material was calculated.

Curcumin loading solubility determination

Curcumin loading in series of pore size reduced silica materials was performed using Rotavapor technique. To rotavapor flask (RF) containing 80 mg of silica material, 20 mg of curcumin was added followed by addition of 5 ml of methanol. This suspension was sonicated for 1 min in ultrasonic bath

and the RF was affixed to the rotavapor assembly and methanol was slowly evaporated at 50 °C. The solvent evaporation procedure was continued for another 30 mins to ensure complete solvent removal.

Curcumin solubility studies were conducted by adding an excess quantity of curcumin and curcumin loaded silica material to 2 ml of water and kept for shaking for 48 hrs at 37°C. The suspension was then centrifuged and the supernatant was analysed for curcumin content at 432 nm using UV-VIS spectrophotometer.

Reproducibility of VVD process

Reproducibility of VVD process was demonstrated by freshly synthesizing SBA-15 (denoted as SBA-15-CN-E$^{\#}$, N=0-3) and MCM-41 (denoted as MCM-41-CN-E$^{\#}$, N=0-3) materials using TEOS as the silica precursor for 3 VVD cycles. The N_2 adsorption-desorption isotherms and the pore size distribution curves for SBA-15-CN-E$^{\#}$ (Figures S6) and MCM-41-CN-E$^{\#}$ (Figure S7) are similar to SBA-15-CN-E and MCM-41-CN-E, respectively. The variation of pore size for SBA-15-E$^{\#}$ and MCM-41-E$^{\#}$ (Figure S8) is similar to SBA-15-E and MCM-41-E respectively. The pore sizes, surface areas and pore volumes of SBA-15-CN-E$^{\#}$ (N=0-3) and MCM-41-CN-E$^{\#}$ (N=0-3) are listed in Table S2 for comparison.

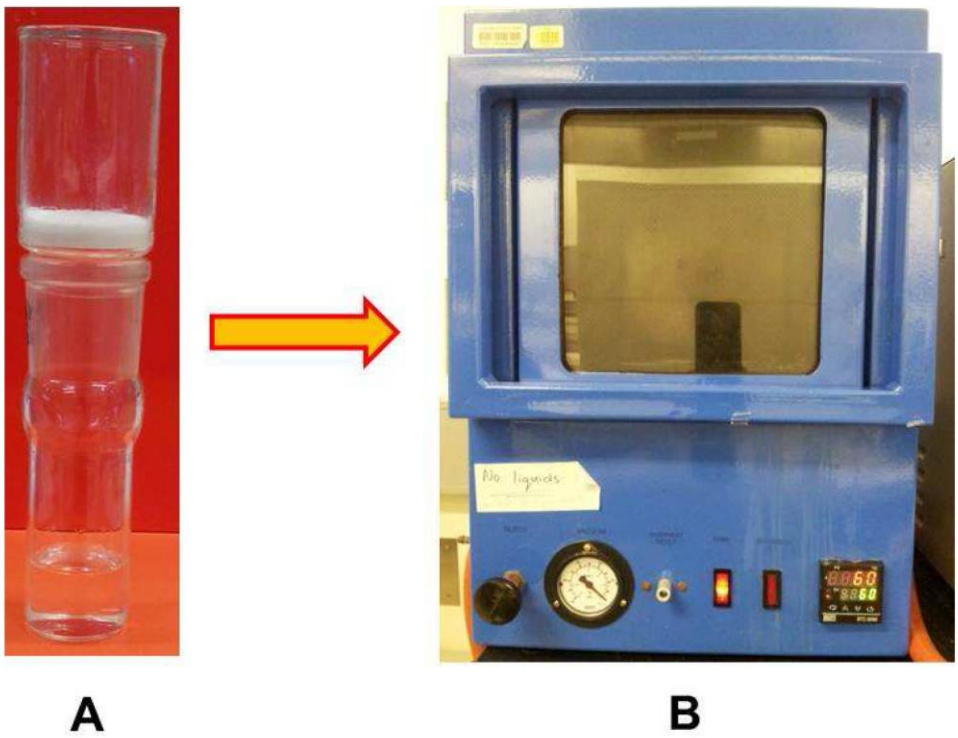

Figure S1. A scheme showing the home-made VVD apparatus and the VVD process. A) Custom made VVD apparatus for the VVD process consisting of upper and lower chamber. Upper chamber is a custom made glass crucible with G4 sintered glass disc to hold the mesoporous silica material. Lower

chamber is a glass cylinder to contain the silica precursor. B) Placing the VVD apparatus in the vacuum oven for the initiation of VVD process. Temperature is set at 60°C.

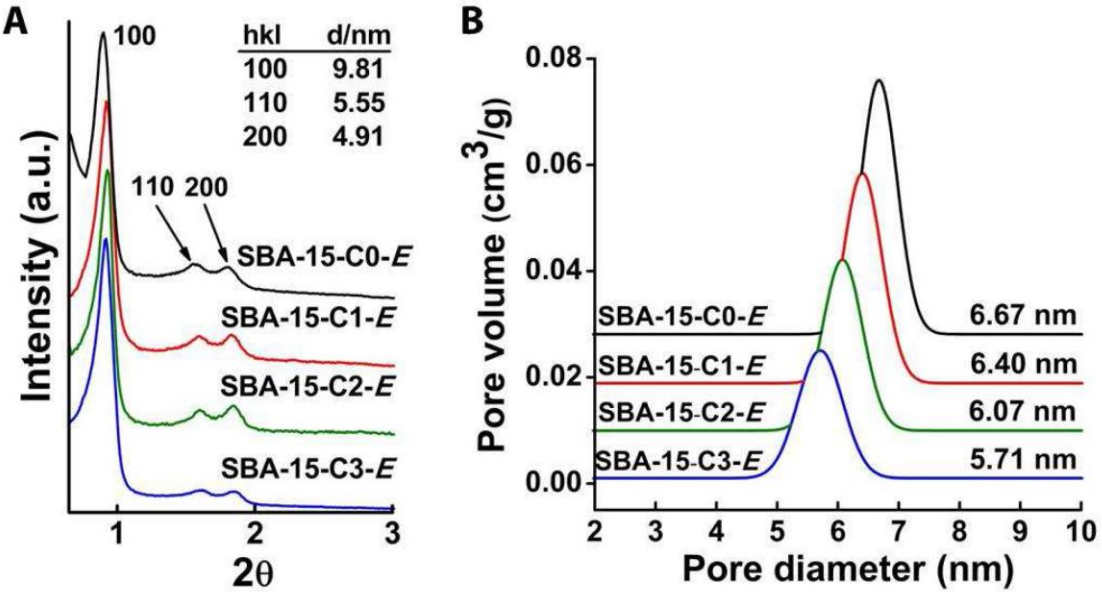

Figure S2. XRD patterns (A) and BJH pore size distribution curves (B) of calcined SBA-15-CN-*E* (N = 0-3) materials.

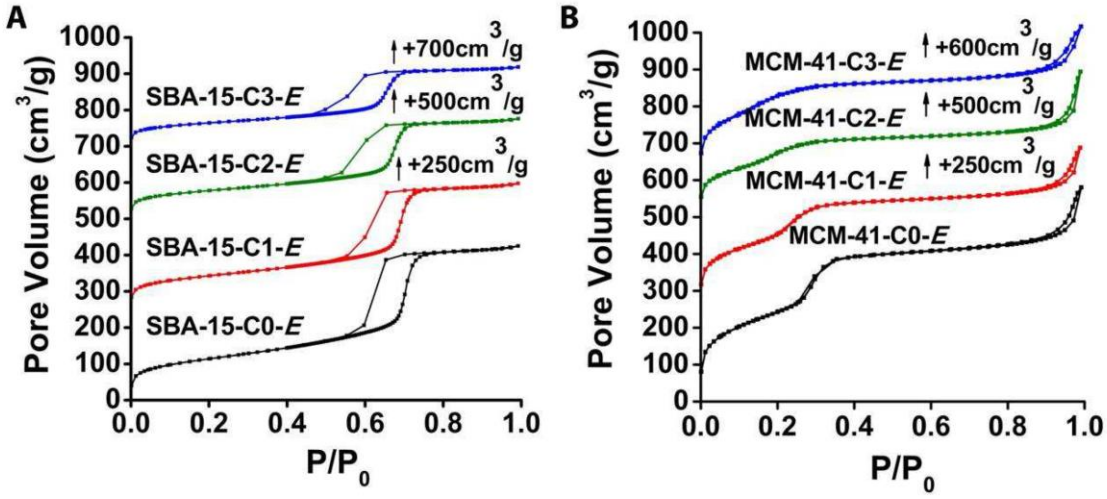

Figure S3. N_2 adsorption - desorption isotherms of calcined SBA-15-CN-*E* (N = 0-3) materials (A) and MCM-41-CN-*E* (N = 0-3) materials (B).

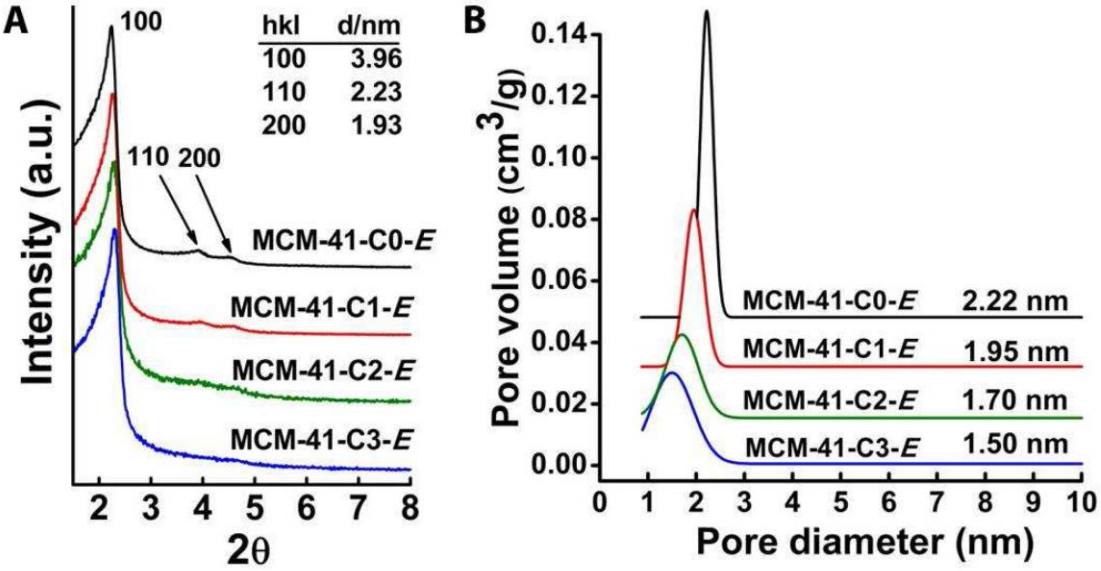

Figure S4. XRD patterns (A) and BJH pore size distribution plots (B) of calcined MCM-41-CN-*E* (N = 0-3) materials.

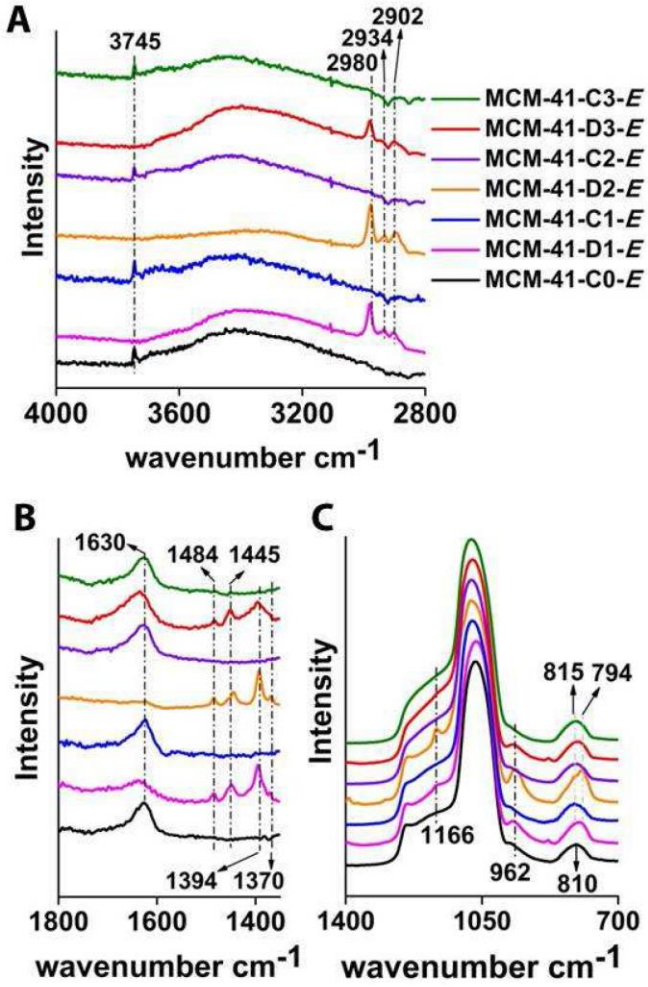

Figure S5.FTIR spectra of MCM-41-CN-*E* (N = 0-3) and MCM-41-DN-*E* (N = 1-3) samples.

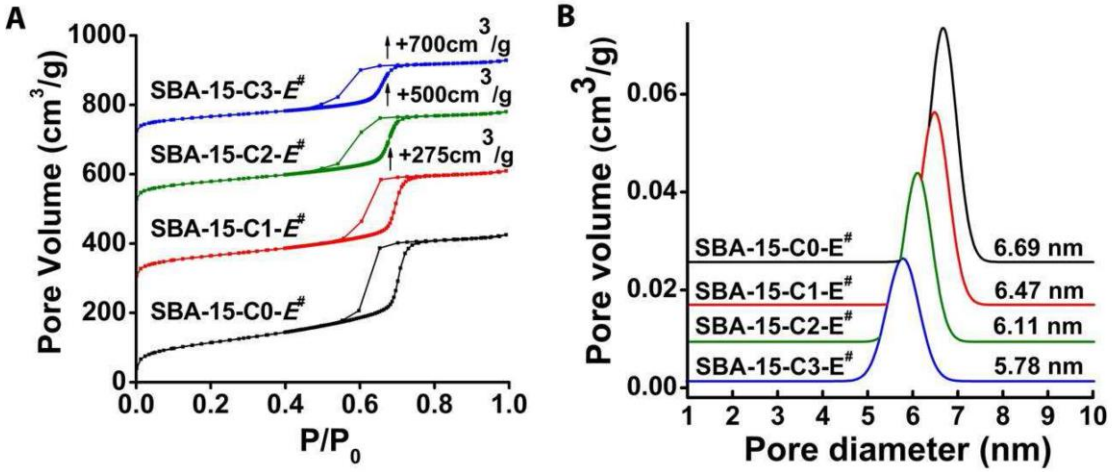

Figure S6. N_2 adsorption - desorption isotherms (A) and BJH pore size distribution plots (B) of calcined SBA-15-CN-*E*$^{\#}$ (N = 0-3) materials.

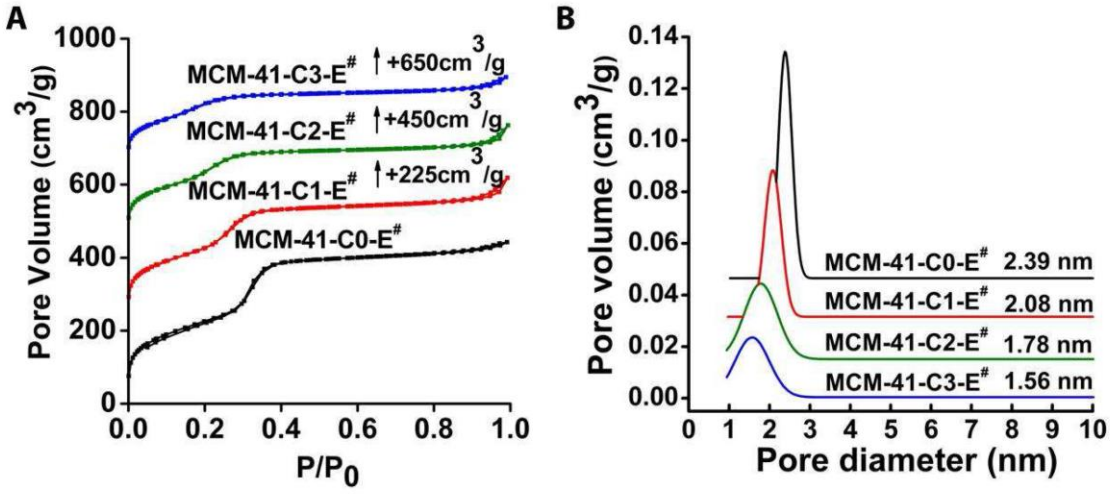

Figure S7. N_2 adsorption - desorption isotherms (A) and BJH pore size distribution plots (B) of calcined MCM-41-CN-*E*$^{\#}$ (N = 0-3) materials.

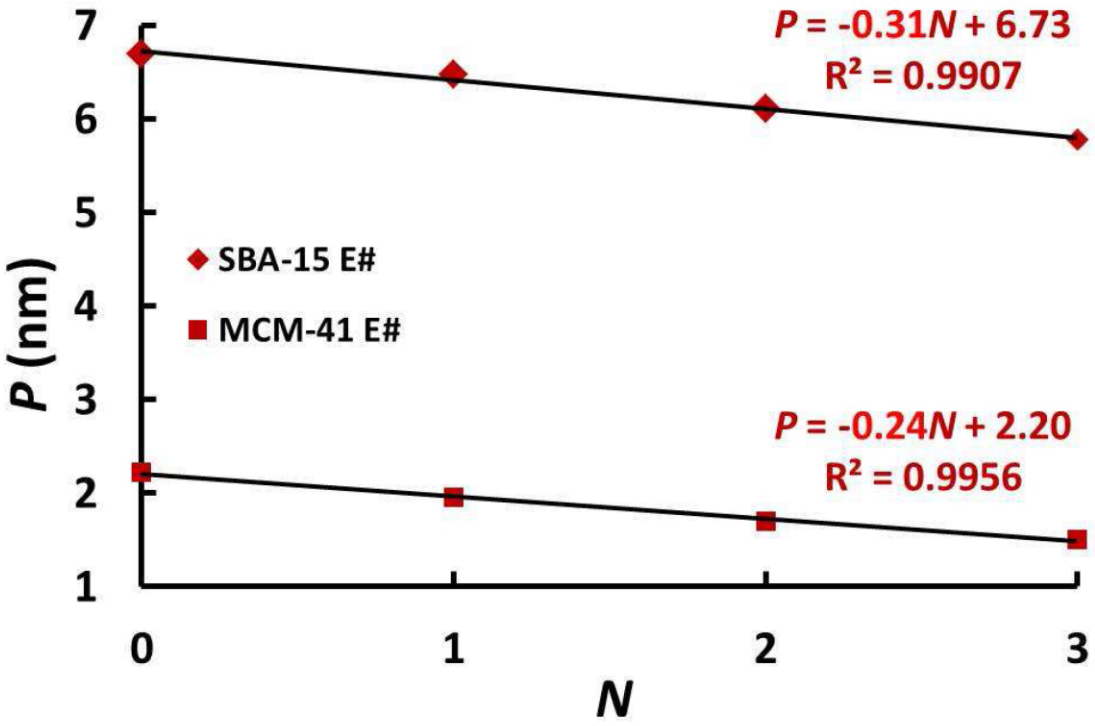

Figure S8. Variation of pore size, *P*, as a function of *N* for both SBA-15-CN-*E*$^{\#}$ (N= 0-3) and MCM-41-CN-*E*$^{\#}$ (N= 0-3) materials. R^2 is the regression coefficient.

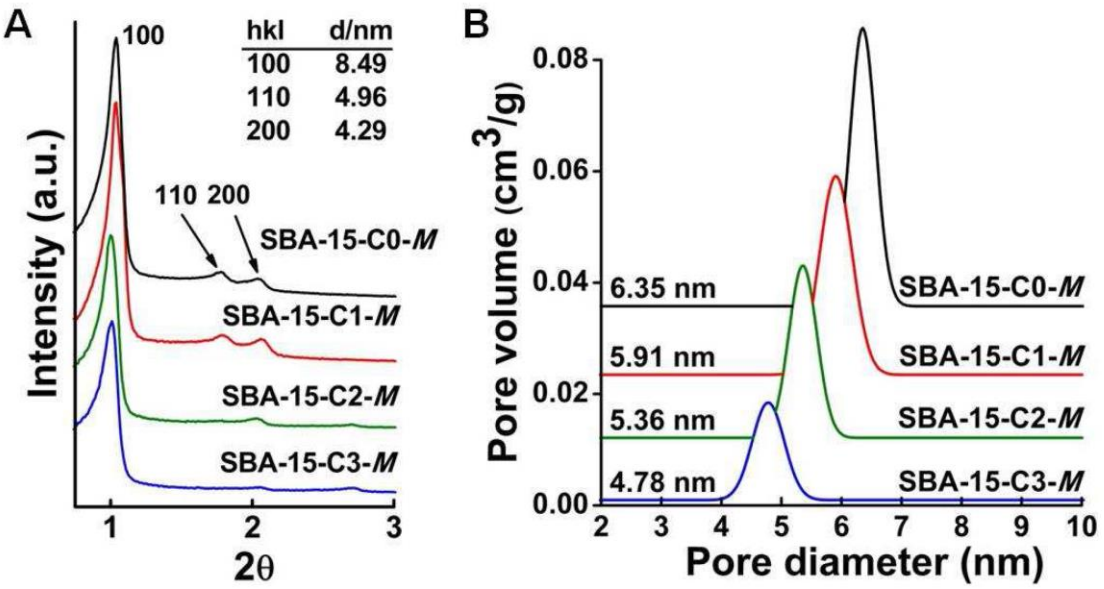

Figure S9. XRD patterns (A) and BJH pore size distribution plots (B) of calcined SBA-15-CN-*M* (N = 0-3) materials.

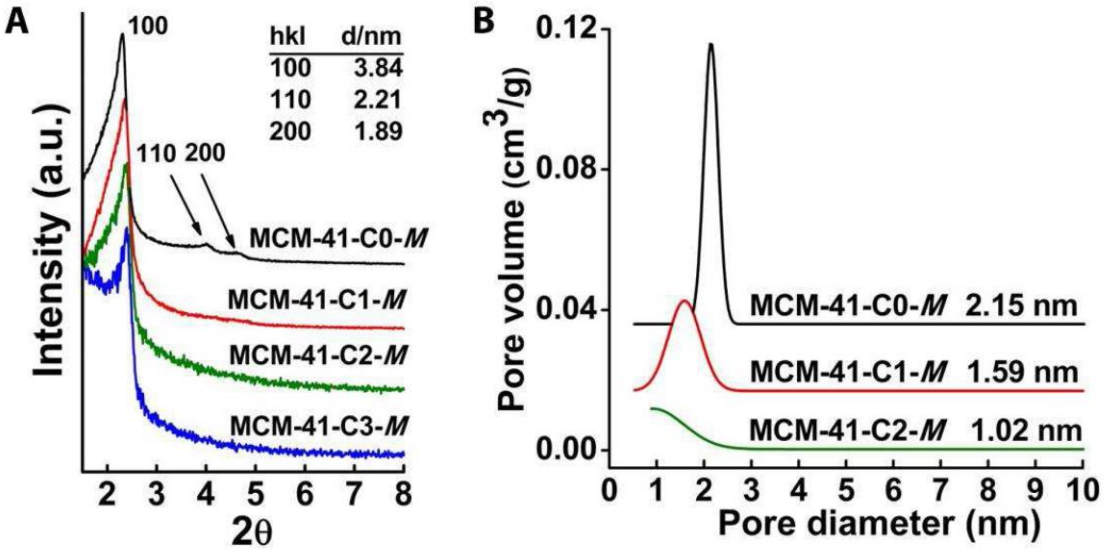

Figure S10. XRD patterns (A) and BJH pore size distribution plots (B) of calcined MCM-41-CN-*M* (N = 0-3) samples.

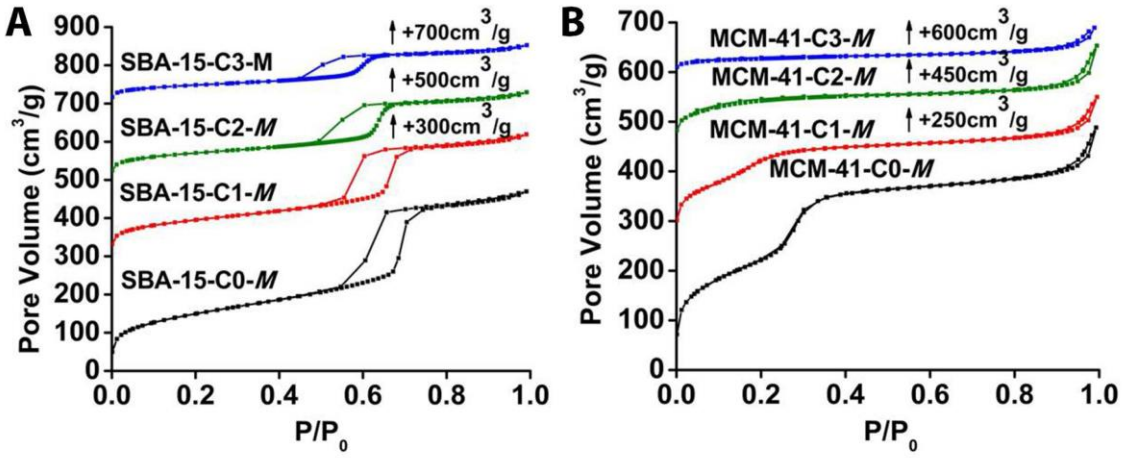

Figure S11. N_2 adsorption-desorption isotherms of calcined SBA-15-CN-*M* (N = 0-3) (A) and MCM-41-CN-*M* (N = 0-3) (B) materials.

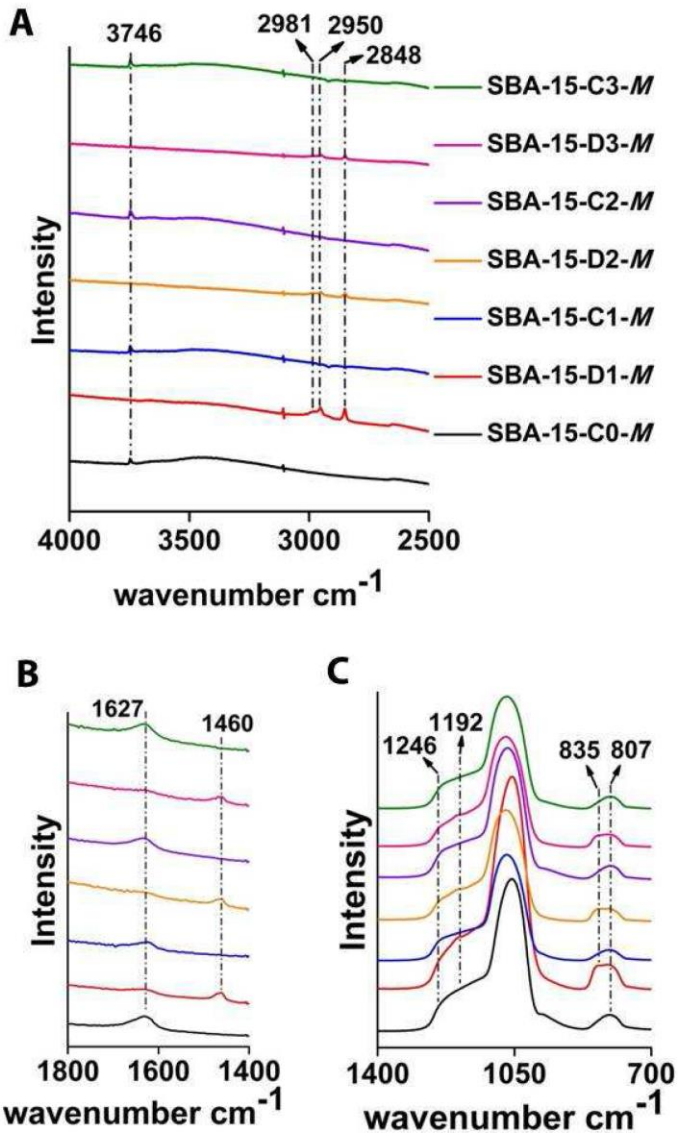

Figure S12. FTIR spectra of SBA-15-CN-*M* (N = 0-3) and SBA-15-DN-*M* (N = 1-3) samples

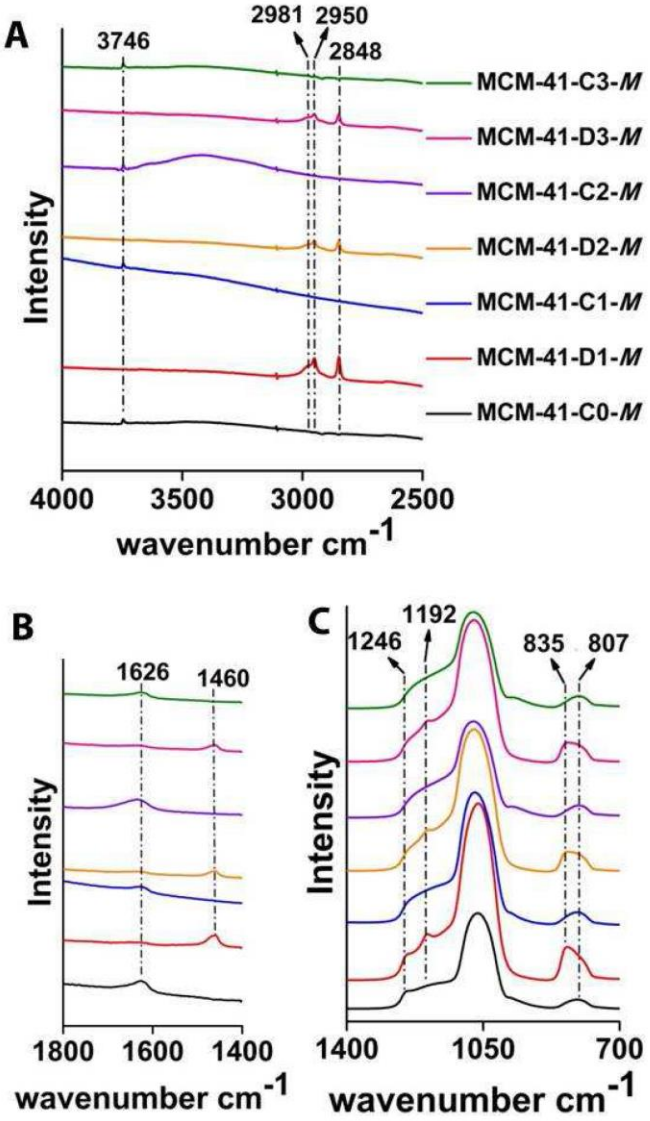

Figure S13. FTIR spectra of MCM-41-CN-*M* (N = 0-3) and MCM-41-DN-*M* (N = 1-3) samples.

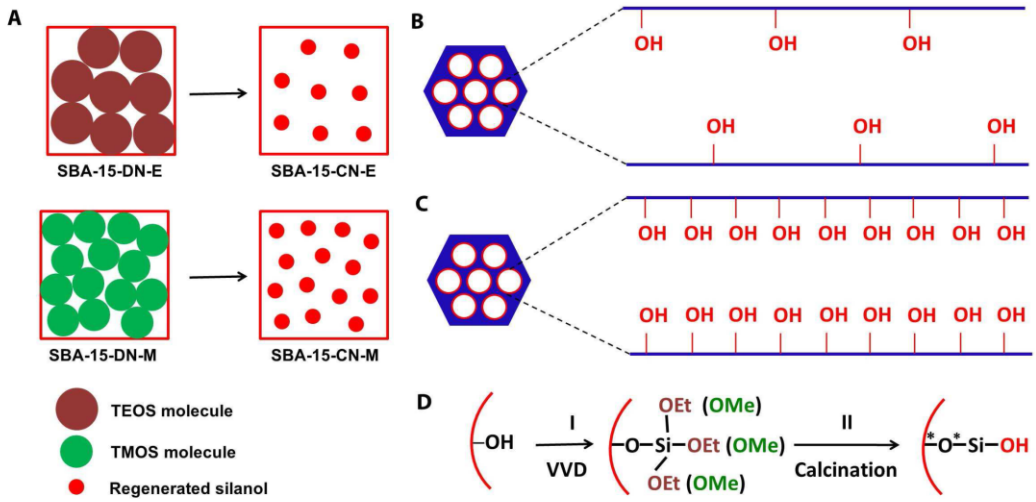

Figure S14. A) Schematic representation of SBA-15 pore wall surface after deposition step of the silica precursor and calcination step. B) Schematic representation of SBA-15 material depicting pore channel with sparsely distributed surface of regenerated silanols in real situation. C) Schematic representation of SBA-15 material depicting pore channel with uniform monolayer surface of regenerated silanols in an ideal situation. D) VVD process demonstrating the changes occurring in the deposition and calcination steps. The schematic representations used in figures A-D are not to scale.

In one VVD cycle, the silica precursor is anchored to surface silanol during deposition step I and condenses to regenerate silanol in calcination step II. On completion of one VVD cycle, regenerated silanol contribute twice the bond length of Si-O (marked as ∗ in Figure S14D). Considering the bond length of Si-O (0.163 nm) and Si-O-Si bond angle (140°), the net increase in bond length comes to 0.31 nm. In ideal situation such as in Figures S14A and S14C, with monolayer silanol distribution, pore size would be reduced by 0.62 nm (0.31 nm from either pore wall surface). In actual situation (Figure S14B), as -Si(OEt)$_3$ condenses to Si-OH, the density of regenerated silanol is reduced and we observe sparse distribution of regenerated silanols leading to pore size reduction of 0.29 nm.

Table S1. Physicochemical properties of calcined SBA-15-CN-*E*, MCM-41-CN-*E,* SBA-15-CN-*M* and MCM-41-CN-*M* materials

Sample	*a* (nm)	*P* (nm)	S_{BET} (m^2/g)	V_p (cm^3/g)
SBA-15-C0-*E*	11.33	6.67	401	0.658
SBA-15-C1-*E*	11.09	6.40	325	0.538
SBA-15-C2-*E*	10.97	6.07	271	0.426
SBA-15-C3-*E*	11.09	5.71	224	0.338
MCM-41-C0-*E*	4.57	2.22	976	0.898
MCM-41-C1-*E*	4.49	1.95	871	0.677
MCM-41-C2-*E*	4.47	1.70	672	0.610
MCM-41-C3-*E*	4.43	1.50	523	0.544
SBA-15-C0-*M*	9.80	6.35	527	0.726
SBA-15-C1-*M*	9.90	5.91	334	0.493
SBA-15-C2-*M*	10.30	5.36	246	0.355
SBA-15-C3-*M*	10.20	4.78	168	0.236
MCM-41-C0-M	4.43	2.15	946	0.755
MCM-41-C1-*M*	4.32	1.59	639	0.464
MCM-41-C2-*M*	4.28	1.02	309	0.314

Note: *a*= unit cell parameter; *P* = pore size; S_{BET} = BET surface area; V_p = total pore volume.

Table S2. Physicochemical properties of calcined SBA-15-CN-$E^{\#}$ and MCM-41-CN-$E^{\#}$ materials

Sample	P (nm)	S_{BET} (m^2/g)	V_p (cm^3/g)
SBA-15-C0-$E^{\#}$	6.69	401	0.658
SBA-15-C1-$E^{\#}$	6.47	313	0.518
SBA-15-C2-$E^{\#}$	6.11	276	0.433
SBA-15-C3-$E^{\#}$	5.78	231	0.353
MCM-41-C0-$E^{\#}$	2.39	847	0.684
MCM-41-C1-$E^{\#}$	2.08	846	0.609
MCM-41-C2-$E^{\#}$	1.78	749	0.483
MCM-41-C3-$E^{\#}$	1.56	631	0.378

Note: P = pore size; S_{BET} = BET surface area; V_p = total pore volume.

Table S3. Number of TEOS molecules occupied/ sq. nm for SBA-15 and MCM-41 using TEOS as silica precursor

Sample name	SA (m^2/g)	Δ W (g)	M_e (mol)	N_e	N_e / m^2	N_e / nm^2
SBA-15-D1-*E*	423	0.1294	0.0006	3.7×10^{20}	8.9×10^{17}	0.9
SBA-15-D2-*E*	344	0.1007	0.0005	2.9×10^{20}	8.5×10^{17}	0.9
SBA-15-D3-*E*	208	0.0648	0.0003	1.9×10^{20}	9.0×10^{17}	0.9

Note: SA = BET Surface area of SBA-15-CN-E (N=0-3); Δ W = Weight gain after step I of VVD process; M_e = Moles of TEOS molecules; N_e = Number of TEOS molecules.

Reference:

(1) W. Ostwald, *Z. Phys. Chem.-Stoch. Ve,* 1900, **34**, 495.
(2) S. Yang, L. Z. Zhao, C. Z. Yu, X. F. Zhou, J. W. Tang, P. Yuan, D. Y. Chen and D. Y. Zhao, *J. Am. Chem. Soc.,* 2006, **128**, 10460.
(3) D. H. Pan, P. Yuan, L. Z. Zhao, N. A. Liu, L. Zhou, G. F. Wei, J. Zhang, Y. C. Ling, Y. Fan, B. Y. Wei, H. Y. Liu, C. Z. Yu and X. J. Bao, *Chem. Mater.,* 2009, **21**, 5413.

Chapter 5

Mesoporous Silica Nanoparticles Enhance the Cytotoxicity of Curcumin

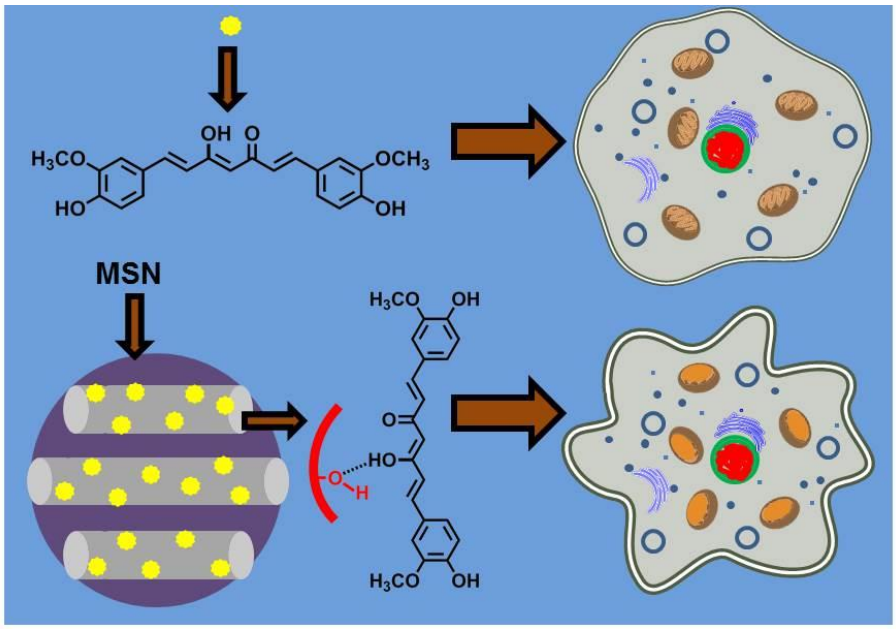

Curcumin encapsulated in mesoporous silica nanoparticles showed improved solubility, in vitro release profile and significantly enhanced cell cytotoxicity compared to the pure drug.

Chapter 5 is included as it appears in RSC Advances, 2014, 4(2), 709-712.

RSC Advances

COMMUNICATION

Mesoporous silica nanoparticles enhance the cytotoxicity of curcumin†

Cite this: *RSC Adv.*, 2014, **4**, 709

Received 8th August 2013
Accepted 5th November 2013

DOI: 10.1039/c3ra44257h

www.rsc.org/advances

Siddharth Jambhrunkar,‡ Surajit Karmakar,‡ Amirali Popat, Meihua Yu and Chengzhong Yu*

Curcumin encapsulated in mesoporous silica nanoparticles showed improved solubility, *in vitro* release profile and significantly enhanced cell cytotoxicity compared to the pure drug.

Curcumin, a diferuloylmethane obtained from the rhizomes of the plant *Curcuma longa*,[1] is commonly used as a spice, dye and traditional medicine in Indian and Chinese culture (see Scheme 1A for its structure). Curcumin possesses a range of pharmacological activities such as antiseptic, anti-inflammatory, antioxidant, antiarthritic, and anticancer functions.[2] It has been found that curcumin inhibits the viability and proliferation of a variety of human cancer cell lines including gastrointestinal cancers, genitourinary cancers, breast cancer, ovarian cancer, lung cancer, melanoma, and sarcoma.[3] Despite its advantages, the clinical application of curcumin is stalled due to its poor aqueous solubility leading to poor bioavailability.[4]

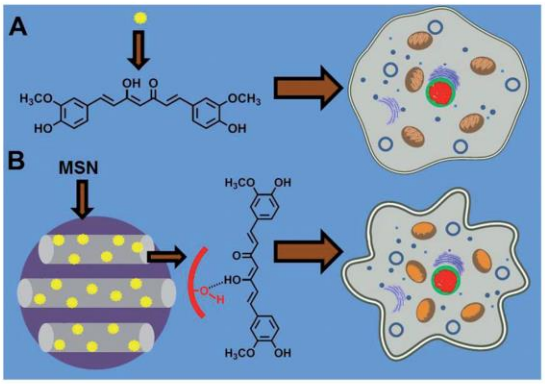

Scheme 1 Schematic representation comparing treatment of SCC-25 cell with pure curcumin (A) and curcumin encapsulated MCM-41 (B) displaying higher cytotoxic effect by curcumin encapsulated MCM-41.

Several curcumin delivery systems such as surfactant complexes, liposomes, hydrogels, and polymeric nanoparticles have been developed but suffer from synthesis complexity and poor biological stability.[5] Compared to the organic counterparts, mesoporous silica nanoparticles (MSNs) with rigid inorganic frameworks have attracted increasing attention as drug delivery carriers[6] owing to their unique properties.[7] Previously, curcumin was encapsulated in cetyltrimethylammonium bromide (CTAB) micelle followed by silica coating,[8] or used as a model drug to test its pH-dependent *in vitro* release behavior in modified porous silica materials.[9,10] It is noted that curcumin undergoes rapid degradation at pH > 7.70 (condition used in *in vitro* release studies).[11] Moreover, CTAB has shown toxicity in cell studies.[12] In a recent study, a solid silica and curcumin conjugate was prepared, showing cytotoxicity against cancer and normal cell lines.[13] However, as ammonia was used to prepare the conjugate, the drug structure in the conjugate is not clear, as curcumin may exist in different forms dependent on the pH values.[14] It is concluded that the great potential of MSNs in curcumin formulation, *i.e.*; using nanopores with high pore volumes as the reservoir for drug loading and controlled release, and using the desired particle size for cellular delivery, is yet to be exploited.

In this work, for the first time, we demonstrate that curcumin can be successfully encapsulated in the nanopores of MSNs through a hydrogen-bonding model (Scheme 1B) leading to significantly higher cell cytotoxicity. Compared to pure drug, the curcumin loaded inside MSNs shows enhanced solubility, sustained release profile, and improved cell cytotoxicity towards SCC-25, a skin cancer cell line. It is shown that the cellular toxicity is associated with the inhibition of polycomb group (PcG) onco-proteins, which are highly expressed in cancer cells and responsible for the cell proliferation and survival.[15] The

Australian Institute for Bioengineering and Nanotechnology, The University of Queensland, Brisbane, QLD 4072, Australia. E-mail: c.yu@uq.edu.au; Fax: +61 7 3346 3973; Tel: +61 7 3346 3283

† Electronic supplementary information (ESI) available: Experimental details and Results. See DOI: 10.1039/c3ra44257h

‡ These authors contribute equally to this paper.

curcumin encapsulated in MSNs sufficiently knocks down the expression level of PcG proteins, thus the growth and transformation of cancer cells are inhibited.[16]

MCM-41[17] type MSNs were synthesized and curcumin (CUR) was encapsulated into calcined MCM-41 (MCM-41–CUR) by a simple rotary evaporatory (Rotavap) technique (see ESI†). For comparison the physical mixture of MCM-41 and curcumin (MCM-41–CUR PM) was also prepared.

The X-ray diffraction (XRD) pattern of calcined MCM-41 (Fig. S1A†) shows three well resolved diffractions at 2θ of 2.68, 4.63 and 5.34° with a reciprocal *d*-spacing ratio close to $1 : \sqrt{3} : 2$, which can be indexed as 100, 110 and 200 reflections of an ordered two-dimensional (2D) hexagonal mesostructure (*p6mm*). MCM-41CUR displayed XRD pattern similar to that of MCM-41 demonstrating retention of the ordered structure after the curcumin encapsulation. Transmission electron microscopy (TEM) image of MCM-41 shows the typical well-ordered hexagonal structure (Fig. S1B†). Dynamic light scattering (DLS) measurements reveal a mean size of 164 (PDI = 0.23) and 190 nm (PDI = 0.31) for MCM-41 and MCM-41–CUR, respectively (Fig. S1C†).

The N_2 adsorption–desorption isotherms of MCM-41 and MCM-41–CUR (Fig. S2A†) exhibited typical type IV isotherm and a steep capillary condensation step occurring at a relative pressure (P/P_0) range of 0.2–0.4. Compared to MCM-41, the surface area and pore volume of MCM-41–CUR decrease (Table S1†). From the pore size distribution curves it is shown that the pore size of MCM-41–CUR decreases from 2.23 to 2.12 nm (Fig. S2B†), indicating that CUR forms nano-sized aggregates in the pores.

Thermogravimetric analysis (TGA) shows 17% of curcumin encapsulation for MCM-41–CUR (Fig. S3A†), indicating a high efficiency (85%) of the Rotavap process used for curcumin encapsulation, in accordance with a previous report.[18] For comparison, MCM-41–CUR PM sample shows a CUR weight loss of 20% identical to the feed ratio in the physical mixing. Differential scanning calorimetry (DSC) analysis was performed to determine the crystallisation behaviour of curcumin in MCM-41–CUR and MCM-41–CUR PM (Fig. S3B†). Pure curcumin clearly displays a sharp melting point peak at 176 °C. A small peak is observed for MCM-41–CUR PM indicating existence of curcumin's crystalline structure after physical mixing. However, such a peak cannot be found in MCM-41–CUR, suggesting curcumin has been loaded successfully in the pores of MCM-41 as nano-sized aggregates.[19]

Fourier transform infrared (FTIR) analysis was performed to study the interaction between curcumin and MCM-41. To observe the information clearly, only regions of interest are shown in Fig. S4.† MCM-41 exhibits one typical peak at 3745 cm^{-1} assigned to isolated silanols (ν(O–H)) whereas CUR displays a sharp peak at 3507 cm^{-1} and a broad peak at 3293 cm^{-1} (–OH group vibrations without and with intermolecular hydrogen bonding, respectively).[20] The above three peaks can be observed in the spectrum of MCM-41–CUR PM, however, not in MCM-41–CUR. Instead a new broad peak centered at 3428 cm^{-1} (Fig. S4A†) can be seen in MCM-41–CUR due to intermolecular hydrogen bonding between isolated silanol and enolic hydroxyl group[21] (Scheme 1B). Additionally, the other typical CUR bands are also found in MCM-41–CUR (Fig. S4A and B†).

Solubility of curcumin was determined by preparing saturated solution of CUR, MCM-41–CUR and MCM-41–CUR PM in water to reach the equilibrium concentration. Curcumin solubility was increased by 71% in MCM-41–CUR (0.53 μg ml^{-1}) compared to CUR (0.31 μg ml^{-1}, Fig. S5A†), in accordance with a previous study using Indole-3-butyric acid loaded in MCM-41.[19a] MCM-41–CUR PM showed solubility similar to CUR (0.36 μg ml^{-1}). The enhanced solubility of curcumin in MCM-41–CUR is attributed to the encapsulation in nanopores based on Ostwald–Freundlich equation where the solubility enhancement is related to particle size.[22] This augmented solubility of curcumin from MCM-41–CUR is also observed from *in vitro* release profile performed in 0.5% Sodium lauryl sulphate (SLS) as the dissolution medium (Fig. S5B†). After 1 h, the release for CUR, MCM-41–CUR and MCM-41–CUR PM was 0.25%, 0.67% and 0.29% respectively. The drug release profile increased slowly for MCM-41–CUR reaching 28.5% after 72 h whereas the drug release for CUR and MCM-41–CUR PM was just 8.9% and 9%, respectively. The faster and higher release amount of CUR from MCM-41–CUR should be attributed to the formation of CUR nano-aggregates in the pore channels of MCM-41.

Taking advantage of the improved solubility and *in vitro* release profile, cell cytotoxicity studies using MTT assay on SCC-25 cell line was conducted in triplicate (see ESI, *In vitro* Cytotoxicity Assay and Table S2† for % cell viability with standard deviation). MCM-41 showed no cytotoxicity even after 72 h confirming earlier reports of silica nanoparticles to be a better drug carrier system.[23] MCM-41–CUR treated cells showed dose and time-dependent higher cell cytotoxicity compared to CUR and MCM-41–CUR PM (Fig. 1A). For example, the cell viability from CUR (46%) and MCM-41–CUR (37%) is similar at 45 ppm dose after 24 h but higher than that of MCM-41–CUR PM (67%). Cytotoxicity from CUR reaches almost maximum activity showing no increase in cytotoxicity at 48 and 72 h. On the other hand, the cell viability from MCM-41–CUR decreases with exposure time showing 11% and only 2% at 48 and 72 h, respectively. The superior cytotoxicity of MCM-41–CUR could be attributed to enhanced and sustained release of curcumin from the MCM-41–CUR as demonstrated from the *in vitro* dissolution studies (Fig. S5B†). Moreover, it was demonstrated that MSNs upto 250 μg ml^{-1} did not affect cell viability when studied in HEK 293 cells.[24] As there is no report using curcumin nanoformulation in SCC-25 cell line, we compared our results with studies performed in MCF-7 cell line using curcumin nanospheres or solid lipid nanoparticles and found the cytotoxicity observed in our studies is comparable.[5b,25] When compared to curcumin encapsulated in a polymeric system and its toxicity in a Pancreatic cancer cell line XPA-1, the IC50 value of MCM-41–CUR is slightly higher (24 μM compared to 19 μM), indicating the efficacy of our system is slightly lower.[26]

We further studied the down-regulation of PcG proteins – enhancer of zeste homolog 2 (EzH2) and B lymphoma Mo-MLV insertion region 1 homolog (Bmi-1) by conducting Western blot analysis on SCC-25 cell line (Fig. 1B). The glyceraldehyde-3-phosphate dehydrogenase (GAPDH) was used as an internal

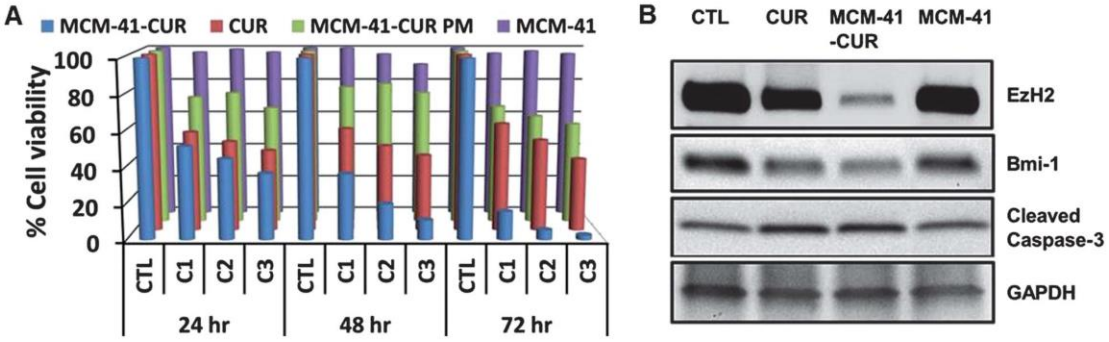

Fig. 1 *In vitro* cytotoxicity of pure curcumin, MCM-41–CUR and MCM-41–CUR PM in SCC-25 cell line after 24, 48 and 72 h (A). CTL, C1, C2 and C3 denote the control group, curcumin equivalent dose of 15 ppm, 30 ppm and 45 ppm respectively used in the cell cytotoxicity experiment. Protein expression studies using Western blot analysis for pure curcumin, MCM-41–CUR and MCM-41 (B).

loading control in the analysis. We observed that CUR and MCM-41–CUR increases activation of caspase-3 through generation of cleaved caspase-3 resulting in enhanced cell apoptosis. MCM-41–CUR mediated suppression of PcG proteins and protease mediated apoptosis are the key events in SCC-25 cell death. The efficacy of MCM-41–CUR was clearly evident from the dramatic reduction in EzH2 level compared to CUR. This higher efficacy could be due to the enhanced endocytosis as observed from the higher silica content in SCC-25 cells carrying curcumin cargo in the cells (Fig. S6†) and time-dependent controlled release of curcumin from MCM-41–CUR. Though there are not many reports focusing on the impact of curcumin nano-formulation on PcG proteins, our observation is in line with previous report studying the effect of free curcumin on down-regulation of EzH2 expression in human breast cancer MDA-MB-435 cells.[27]

In summary, we have demonstrated a simple and efficient technique for curcumin encapsulation in the nanopores of MCM-41 type MSNs. This strategy leads to improved aqueous solubility, enhanced drug release, and high cellular delivery efficiency of curcumin. Consequently, compared to the pure drug, curcumin encapsulated in MCM-41 possesses enhanced cytotoxic effect, which is linked with the inhibition of PcG proteins and activation of caspase-3. This work provides a simple but efficient method to design new curcumin based nano-formulations to improve its therapeutic efficacy.

We thank the Australian Research Council and Cancer Council of Queensland for financial support. We acknowledge the Australian National Fabrication Facility and the Australian Microscopy and Microanalysis Research Facility at the Centre for Microscopy and Microanalysis, the University of Queensland.

Notes and references

1 M. T. Huang, Y. R. Lou, W. Ma, H. L. Newmark, K. R. Reuhl and A. H. Conney, *Cancer Res.*, 1994, **54**, 5841.

2 A. Duvoix, R. Blasius, S. Delhalle, M. Schnekenburger, F. Morceau, E. Henry, M. Dicato and M. Diederich, *Cancer Lett.*, 2005, **223**, 181.

3 (*a*) P. Anand, C. Sundaram, S. Jhurani, A. B. Kunnumakkara and B. B. Aggarwal, *Cancer Lett.*, 2008, **267**, 133; (*b*) S. Shishodia, G. Sethi and B. B. Aggarwal, in *Natural Products and Molecular Therapy*, eds. G. J. Kotwal and D. K. Lahiri, New York Acad Sciences, New York, 2005, vol. 1056, p. 206.

4 M. M. Yallapu, M. Jaggi and S. C. Chauhan, *Curr. Pharm. Des.*, 2013, **19**, 1994.

5 (*a*) P. Couvreur, C. Dubernet and F. Puisieux, *Eur. J. Pharm. Biopharm.*, 1995, **41**, 2; (*b*) R. S. Mulik, J. Monkkonen, R. O. Juvonen, K. R. Mahadik and A. R. Paradkar, *Int. J. Pharm.*, 2010, **398**, 190; (*c*) C. Oussoren and G. Storm, *Adv. Drug Delivery Rev.*, 2001, **50**, 143.

6 (*a*) M. Vallet-Regi, A. Ramila, R. P. del Real and J. Perez-Pariente, *Chem. Mater.*, 2001, **13**, 308; (*b*) D. Tarn, C. E. Ashley, M. Xue, E. C. Carnes, J. I. Zink and C. J. Brinker, *Acc. Chem. Res.*, 2013, **46**, 792.

7 A. Szegedi, M. Popova, I. Goshev and J. Mihaly, *J. Solid State Chem.*, 2011, **184**, 1201.

8 N. W. Clifford, K. S. Iyer and C. L. Raston, *J. Mater. Chem.*, 2008, **18**, 162.

9 Y. L. Choi, J. Jaworski, M. L. Seo, S. J. Lee and J. H. Jung, *J. Mater. Chem.*, 2011, **21**, 7882.

10 D. Jin, K. W. Park, J. H. Lee, K. Song, J. G. Kim, M. L. Seo and J. H. Jung, *J. Mater. Chem.*, 2011, **21**, 3641.

11 Y. J. Wang, M. H. Pan, A. L. Cheng, L. I. Lin, Y. S. Ho, C. Y. Hsieh and J. K. Lin, *J. Pharm. Biomed. Anal.*, 1997, **15**, 1867.

12 (*a*) T. Niidome, M. Yamagata, Y. Okamoto, Y. Akiyama, H. Takahashi, T. Kawano, Y. Katayama and Y. Niidome, *J. Controlled Release*, 2006, **114**, 343; (*b*) Q. J. He, J. L. Shi, F. Chen, M. Zhu and L. X. Zhang, *Biomaterials*, 2010, **31**, 3335.

13 R. K. Gangwar, G. B. Tomar, V. A. Dhumale, S. Zinjarde, R. B. Sharma and S. Datar, *J. Agr. Food Chem*, 2013, **61**, 9632.

14 H. H. Tonnesen and J. Karlsen, *Z. Lebensm. Unters. For.*, 1985, **180**, 402.

15 (*a*) S. Liu, M. S. Wolfe and R. T. Borchardt, *Antiviral Res.*, 1992, **19**, 247; (*b*) K. Lee, G. Adhikary, S. Balasubramanian,

R. Gopalakrishnan, T. McCormick, G. P. Dimri, R. L. Eckert and E. A. Rorke, *J. Invest. Dermatol.*, 2008, **128**, 9.
16 Z. S. Xu, H. T. Liu, X. Q. Lv, Y. Q. Liu, S. L. Li and H. X. Li, *Oncol. Rep.*, 2011, **25**, 409.
17 C. T. Kresge, M. E. Leonowicz, W. J. Roth, J. C. Vartuli and J. S. Beck, *Nature*, 1992, **359**, 710.
18 T. Limnell, H. A. Santos, E. Makila, T. Heikkila, J. Salonen, D. Y. Murzin, N. Kumar, T. Laaksonen, L. Peltonen and J. Hirvonen, *J. Pharm. Sci.*, 2011, **100**, 3294.
19 (*a*) V. Ambrogi, F. Famiani, L. Perioli, F. Marmottini, I. Di Cunzolo and C. Rossi, *Microporous Mesoporous Mater.*, 2006, **96**, 177; (*b*) M. Vialpando, A. Aerts, J. Persoons, J. Martens and G. Van den Mooter, *J. Pharm. Sci.*, 2011, **100**, 3411.
20 T. M. Kolev, E. A. Velcheva, B. A. Stamboliyska and M. Spiteller, *Int. J. Quantum Chem.*, 2005, **102**, 1069.
21 R. K. Gangwar, V. A. Dhumale, D. Kumari, U. T. Nakate, S. W. Gosavi, R. B. Sharma, S. N. Kale and S. Datar, *Mater. Sci. Eng., C*, 2012, **32**, 2659.
22 W. Ostwald, *Z. Phys. Chem., Stoechiom. Verwandtschaftsl.*, 1900, **34**, 495.
23 J. Lu, M. Liong, Z. X. Li, J. I. Zink and F. Tamanoi, *Small*, 2010, **6**, 1794.
24 R. Guillet-Nicolas, A. Popat, J. L. Bridot, G. Monteith, S. Z. Qiao and F. Kleitz, *Angew. Chem., Int. Ed.*, 2013, **52**, 2318.
25 N. Suwannateep, W. Banlunara, S. P. Wanichwecharungruang, K. Chiablaem, K. Lirdprapamongkol and J. Svasti, *J. Controlled Release*, 2011, **151**, 176.
26 S. Bisht, G. Feldmann, S. Soni, R. Ravi, C. Karikar, A. Maitra and A. Maitra, *J. Nanobiotechnology*, 2007, **5**, 3.
27 W. F. Hua, Y. S. Fu, Y. J. Liao, W. J. Xia, Y. C. Chen, Y. X. Zeng, H. F. Kung and D. Xie, *Eur. J. Pharmacol.*, 2010, **637**, 16.

Electronic Supplementary Material (ESI) for RSC Advances

Mesoporous Silica Nanoparticles Enhance the Cytotoxicity of Curcumin

Siddharth Jambhrunkar,[a] ‡ Surajit Karmakar, [a] ‡ Amirali Popat,[a] Meihua Yu,[a] Chengzhong Yu[a]

[a]Australian Institute for Bioengineering and Nanotechnology, The University of Queensland, Brisbane, QLD 4072, Australia.

‡ These authors contribute equally to this paper

Corresponding author: c.yu@uq.edu.au. Fax: +61 7 3346 3973; Tel: +61 7 3346 3283.

1. Experimental

Chemicals:

Cetyl trimethylammonium bromide (CTAB), Tetraethoxy orthosilicate (TEOS), Sodium lauryl sulphate (SLS) and Curcumin was purchased from Sigma-Aldrich. Reagent grade sodium hydroxide (NaOH) was received from ChemSupply. Methanol AR was purchased from RCI labscan. Human skin cancer SCC-25 cell line was a kind gift of Prof. Nicholas Saunders from the Princess Alexandra Hospital, Brisbane. Dulbecco's Modified Eagle Medium: Nutrient Mixture F-12 (DMEM/F12) media was purchased from Sigma. Fetal calf serum was purchased from Moregate biotech. All primary IgG antibodies were obtained from Cell Signaling Technology (Danvers, MA, USA). Depending on the primary antibody, the secondary antibody used was either horseradish peroxidase (HRP)-conjugated goat anti-mouse IgG or HRP-conjugated goat anti-rabbit IgG (Santa Cruz Biotechnology, Santa Cruz, CA, USA). Clarity Western ECL Substrate reagent was purchased from Bio-Rad (Australia).

Characterization:

X-ray diffractograms (XRD) were recorded on a Rigaku Miniflex X-ray diffractometer with Fe-filtered Co radiation. Transmission electron microscopy (TEM) images were obtained with a JEOL 1010 operated at 100 kV. Nitrogen physisorption measurements were carried out at -196°C by using a Micromeritics Tristar II 3020 system. MCM-41 and MCM-41-CUR samples were degassed respectively at 200 °C and 100 °C overnight on a vacuum line. The pore-size distribution was measured from the desorption branch of the isotherm using BJH model followed by gaussian fitting. Fourier transform infrared (FTIR) spectra were recorded on ThermoNicolet Nexus 6700 FTIR spectrometer equipped with Diamond ATR (attenuated total reflection) Crystal. For each spectrum, 128 scans and 4 cm^{-1} resolution was applied over the range of 400–4000cm^{-1}. Thermogravimetric and Differential Scanning Calorimetry (DSC)

Electronic Supplementary Material (ESI) for RSC Advances

measurements were performed by a Setaram TG92 instrument with a heating rate of 5 °C/min in air flow. Curcumin concentration was determined using UV-VIS spectrophometer (Shimadzu UV-2450). Dynamic light scattering (DLS) studies were carried out on a Malvern NanoZS zetasizer at 25°C in water.

Experimental Section:

MCM-41 was synthesized with slight modifications to the method reported by Yang et al.[1] 1.0 g of CTAB was added to 480 g of deionized water and kept under stirring until clear solution was obtained. To this solution, 3.5 ml of 2M NaOH was added and temperature was raised to 80 °C. Then, 6.7 ml of TEOS was added slowly to this solution as the silica source and kept under stirring for additional 2 h. The resultant product was obtained by filtration and dried at room temperature. The dried product was calcined at 550 °C for 5 h to remove the surfactant template. The calcined product was termed as MCM-41.

Curcumin loading and in vitro release measurements:

Curcumin loading was performed using rotary evaporation technique. 160 mg of MCM-41 was placed in rotary evaporation flask followed by addition of 40 mg of curcumin to it. 10 ml of methanol was added to the flask, sonicated for 2 mins using a bath sonicator and then attached to the rotary evaporator. Methanol was evaporated slowly from the suspension under vacuum and at a water bath temperature of 50 °C with circulating water maintained at 5 °C to obtain curcumin loaded sample which was designated as MCM-41-CUR.

The in vitro release of curcumin from MCM-41-CUR was evaluated using dialysis bag technique.[2] MCM-41-CUR equivalent to 1 mg of curcumin was weighed and suspended in 1 ml of 0.5 % SLS. This suspension was then placed in dialysis bag (Sigma Aldrich) with 10 kDa molecular weight cutoff and was immersed into 9 ml of 0.5 % SLS at 37°C with continuous stirring. At predetermined time intervals, 1 mL of the samples were withdrawn and immediately replaced with an equal volume of dissolution medium to keep the volume constant. Pure curcumin was studied along with MCM-41-CUR to compare the in vitro drug release profile by weighing 1 mg of pure curcumin and suspending it in 0.5 % SLS similar to that of MCM-41-CUR . These samples were then properly diluted and analyzed for curcumin content at 432 nm using UV-VIS spectrophotometer.

In vitro cytotoxicity assay:

SCC-25 cell line was propagated in a monolayer to sub-confluency at 37°C in 75 cm^2 flasks containing 10 ml of DMEM:F12 media, supplemented with heat inactivated 10% fetal calf

Electronic Supplementary Material (ESI) for RSC Advances

serum (FCS), 1% penicillin, 1% glutamine and 1% streptomycin and hydrocortisone (0.4µg/ml) in a fully-humidified incubator containing 5% CO_2 and 95% air.

The sensitivity of human skin cancer SCC-25 cells to the curcumin nano-formulation was determined by the MTT colorimetric assay. Cells (1×10^4 per well) were seeded in a flat-bottomed 96-well plate and incubated at 37°C and in 5% CO_2. Cells were exposed to silica nanoparticles alone or loaded with curcumin at the concentrations of 15, 30, and 45µg/ml in a dose and time dependent manner for 24, 48 and 72 h. Cells were then treated with MTT reagent (10µl/well volume from 5mg/ml solution in PBS) for 4 h at 37°C. Then DMSO (100µl) was added to each well to dissolve the formazan crystals. The optical density (OD) was recorded at 570 nm in a microplate reader and percentage of residual cell viability was determined. All experiments were performed in triplicate.

Protein expression and Western blotting studies:

Briefly, 3×10^5/mL cells in 6-well plates were treated with MCM-41 and MCM-41-CUR for 48 h. The cells were then washed twice in PBS and lysed in 20 mM Tris (pH 7.5) containing 150 mM NaCl, 1 mM EGTA, 1 mM EDTA, 1% Triton X-100, 2.5 mM sodium pyrophosphate, 1 mM glycerophosphate, 1 mM sodium vanadate, 1 µg of leupeptin, and 1 mM phenylmethylsulfonyl fluoride. Following sonication, cell extracts were centrifuged at 12,000 rpm for 10 min at 4 °C. Protein concentrations were measured using a BCA assay. Protein samples (30 µg), diluted with SDS sample buffer, were electrophoresed on a 10% polyacrylamide gel and electro-blotted on a polyvinylidene difuoride (PVDF) membrane for immunoblot analysis. After blocking in 5% non-fat dry milk, the membrane were probed overnight at 4 °C with primary antibodies and immunoreactivity were detected using anti-mouse or anti-rabbit IgG conjugated peroxidase, then visualized using the Clarity™ Western ECL Substrate kit and the ChemiDoc MP system (Bio-Rad, Australia) according to the manufacturer's instructions.

Silica ICP-OES study:

This study was carried out to measure the silica nanoparticles endocytosis performance in human skin cancer SCC-25 cells (5×10^4 cells per well of 6 wells plate) from both MCM-41 and MCM-41-CUR. The SCC-25 cells were treated similar condition as mentioned in MTT assay and cells from each treatment were washed twice with cold phosphate-buffered saline (PBS, pH 7.4). The cells from both groups were collected separately after 8h following trypsinization and then washed twice with PBS and centrifuged at 5000 rpm for 10 min. Cell lysate were prepared in 200µl ice-cold (4°C) 1x cell lysis buffer (20 mM Tris-HCl (pH 7.5), 150 mM NaCl, 1 mM Na_2EDTA, 1 mM EGTA, 1% Triton, 2.5 mM sodium pyrophosphate, 1 mM beta-

Electronic Supplementary Material (ESI) for RSC Advances

glycerophosphate, 1 mM Na_3VO_4, 1 µg/ml leupeptin) following sonication. Cell lysates were then centrifuged for 10 minutes at 14,000 rpm at 4°C and pellet fractions were collected and dissolved in 200µl of 1M NaOH solution. The collected samples (n=3) were then diluted in PBS and sent to the Agricultural Biotechnology Center at University of Queensland for ICP analysis of Si and expressed in milligram per litre unit.

Electronic Supplementary Material (ESI) for RSC Advances

2. Results

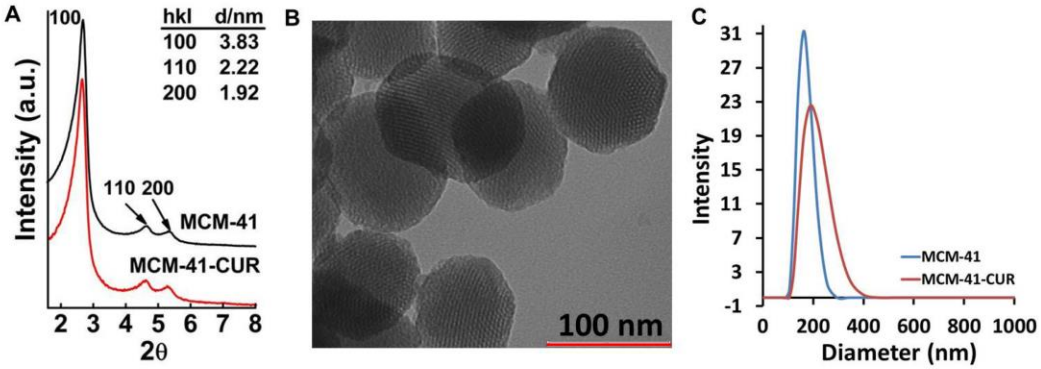

Fig S1. XRD patterns of MCM-41 and MCM-41-CUR (A), TEM image of MCM-41 (B) and DLS size measurements of MCM-41 and MCM-41-CUR (C).

Electronic Supplementary Material (ESI) for RSC Advances

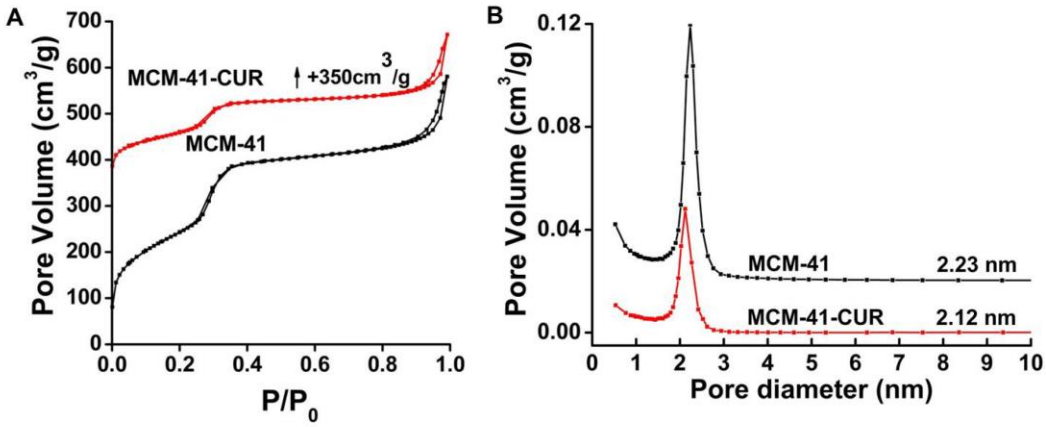

Fig S2. N_2 adsorption - desorption isotherms (A) and BJH pore size distribution plots (B) of MCM-41 and MCM-41-CUR.

Electronic Supplementary Material (ESI) for RSC Advances

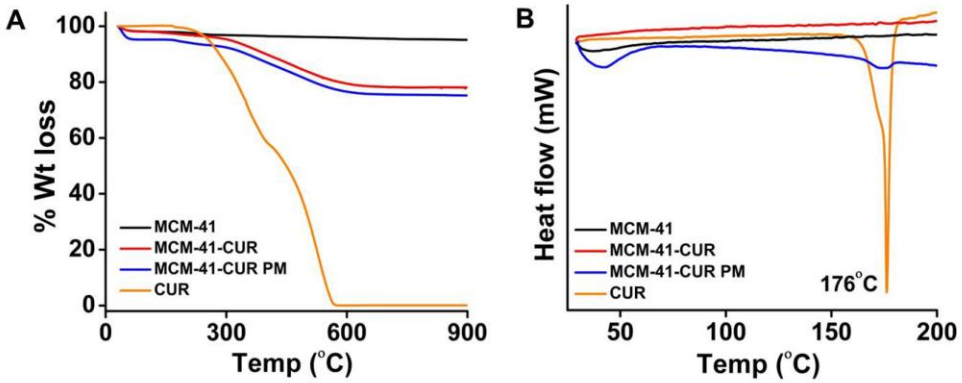

Fig S3. TGA (A) and DSC (B) curves of MCM-41, MCM-41-CUR, MCM-41-CUR PM and Curcumin.

Electronic Supplementary Material (ESI) for RSC Advances

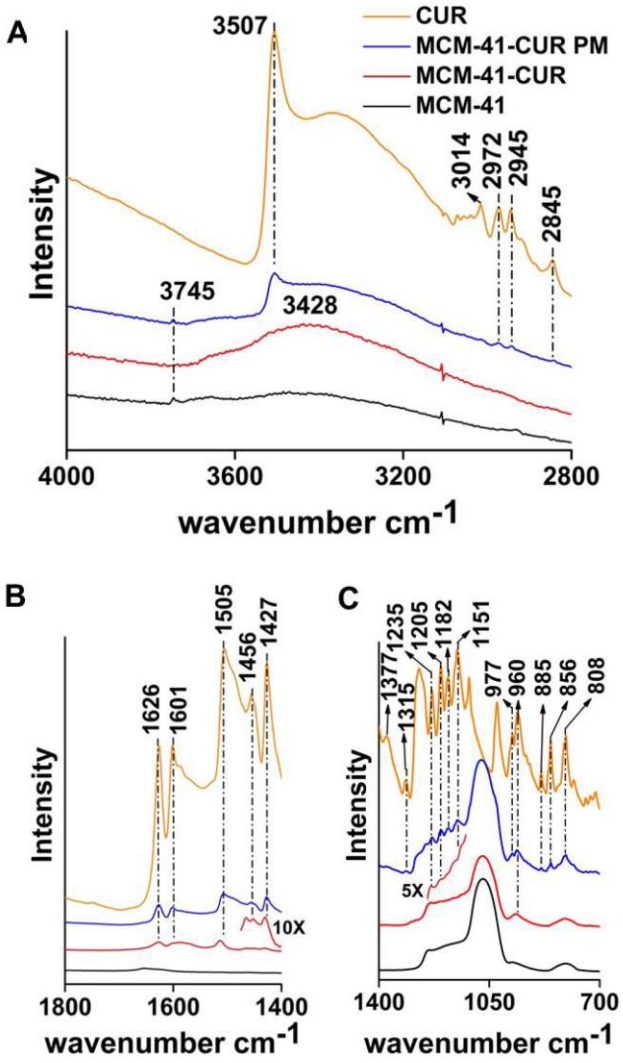

Fig S4. FTIR spectra of MCM-41, MCM-41-CUR, MCM-41-CUR PM and Curcumin.

FTIR spectra of CUR displays several peaks at 3507 cm^{-1} (free –OH group vibration), 3014 cm^{-1} (C-H stretching of aromatic ring), 2845 cm^{-1} (C-H stretching of methyl group), 1626 cm^{-1} (C=O stretching), 1505 cm^{-1} (C=O and C=C vibration), 1456 cm^{-1} (CH_2 bending) and 1377 cm^{-1} (CH_3 bending). A band of peaks is observed at 1000-1300 cm^{-1} in CUR which can be typically attributed to symmetric and asymmetric configurations of C-O-C chains. MCM-41-CUR reveals peak of both CUR and MCM-41. The band at 960 cm^{-1} (Figure S3C) is the characteristic peak for $\rho(CH_3)$, which overlaps with the band of silanols after the encapsulation of curcumin in pores of MCM-41.

Electronic Supplementary Material (ESI) for RSC Advances

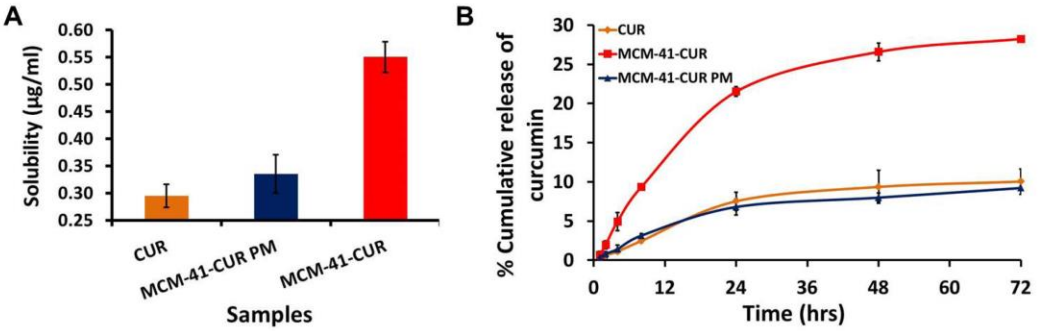

Fig.S5 Aqueous equilibrium solubility (A) and In vitro drug release (B) of Curcumin, MCM-41-CUR and MCM-41-CUR PM in 0.5% SLS.

Electronic Supplementary Material (ESI) for RSC Advances

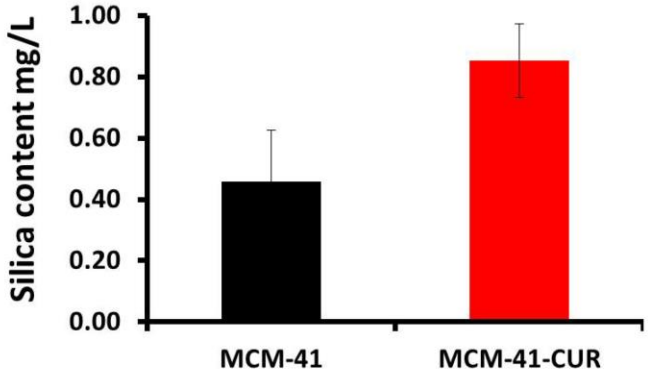

Fig.S6 Silica content analyzed by ICP-OES for MCM-41 and MCM-41-CUR endocytosed in SCC-25 cell line after 8h

Electronic Supplementary Material (ESI) for RSC Advances

Table S1. Physicochemical properties of calcined MCM-41 and curcumin loaded MCM-41

Sample	*a* (nm)	*P* (nm)	S_{BET} (m^2/g)	V_p (cm^3/g)	*Z.P.*
MCM-41	4.42	2.23	976	0.9	-21.03 ± 0.57
MCM-41-CUR	4.47	2.12	480	0.5	-20.53 ± 1.10

Note: *a*=cell dimension; S_{BET} = BET surface area; V_p = pore volume; *P* = pore size; Z.P. = Zeta potential.

Table S2. In vitro cytotoxicity of pure curcumin, MCM-41-CUR and MCM-41-CUR PM performed in SCC-25 cell line in triplicate after 24, 48 and 72h expressing % cell viability with standard deviation

Time	Sample	% Cell viability ± Standard deviation			
		CTL	15 ppm	30 ppm	45 ppm
24 h	CUR	100 ± 0.05	56.42 ± 0.03	50.96 ± 0.02	45.89 ± 0.04
	MCM-41-CUR	100 ± 0.06	52.13 ± 0.04	45.16 ± 0.01	37.17 ± 0.06
	MCM-41-CUR PM	100 ± 0.05	73.53 ± 0.01	75.94 ± 0.04	67.15 ± 0.08
	MCM-41	100 ± 0.05	97.41 ± 0.05	99.21 ± 0.01	97.37 ± 0.08
48 h	CUR	100 ± 0.06	58.41 ± 0.05	48.61 ± 0.03	43.11 ± 0.10
	MCM-41-CUR	100 ± 0.08	36.92 ± 0.03	20.09 ± 0.09	11.06 ± 0.07
	MCM-41-CUR PM	100 ± 0.14	79.33 ± 0.02	81.22 ± 0.02	76.04 ± 0.09
	MCM-41	100 ± 0.05	99.88 ± 0.02	96.26 ± 0.05	90.39 ± 0.05
72 h	CUR	100 ± 0.05	61.23 ± 0.05	51.88 ± 0.02	41.00 ± 0.03
	MCM-41-CUR	100 ± 0.08	15.94 ± 0.12	5.56 ± 0.01	2.66 ± 0.01
	MCM-41-CUR PM	100 ± 0.03	68.04 ± 0.02	62.33 ± 0.01	57.68 ± 0.04
	MCM-41	100 ± 0.12	96.73 ± 0.06	98.08 ± 0.04	96.42 ± 0.10

References

1. S. Yang, L. Z. Zhao, C. Z. Yu, X. F. Zhou, J. W. Tang, P. Yuan, D. Y. Chen and D. Y. Zhao, *J Am Chem Soc*, 2006, **128**, 10460-10466.
2. J. F. Shao, D. H. Zheng, Z. F. Jiang, H. E. Xu, Y. Hu, X. L. Li and X. W. Lu, *Acta Bioch Bioph Sin*, 2011, **43**, 267-274.

Chapter 6

Effect of Surface Functionality of Silica Nanoparticles on Cellular Uptake and Cytotoxicity

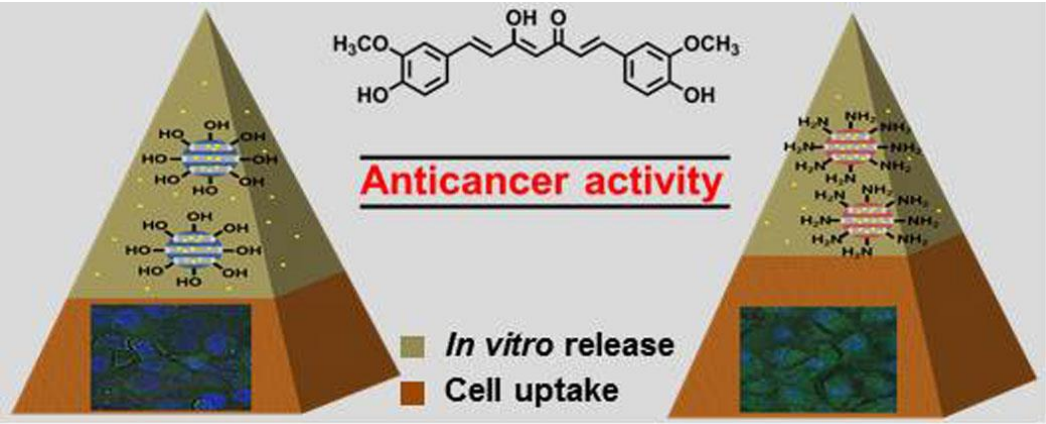

MCM-41 type mesoporous silica nanoparticles (MSNs) with different surface functional groups were synthesized as nanocarriers for curcumin (CUR). The effect of surface functionality (surface charge and hydrophobicity) on the delivery efficiency and anticancer activity in a human squamous cell carcinoma cell line (SCC25) was systematically studied. It was found that MSNs with hydrophobic surface did not enhanced curcumin's cytotoxicity. Curcumin's cytotoxicity was enhanced using MSNs with different surface charge and was comparable.

Chapter 6 is published in Molecular Pharmaceutics, 2014, (DOI: 10.1021/mp500385n)

Effect of Surface Functionality of Silica Nanoparticles on Cellular Uptake and Cytotoxicity

*Siddharth Jambhrunkar[a], Zhi Qu[a], Amirali Popat[b,c], Jie Yang[a], Owen Noonan[a], Luiz Acauan[a], Yusilawati Ahmad Nor[a], Chengzhong Yu[a], Surajit Karmakar[a]**

[a]Australian Institute for Bioengineering and Nano-technology, The University of Queensland, Brisbane, QLD 4072, Australia.

[b]The School of Pharmacy, The University of Queensland, Brisbane, QLD 4072, Australia.

[c]Mucosal Diseases Group, Mater Research Institute – The University of Queensland, Translational Research Institute, 37 Kent St, Woolloongabba, QLD 4102.

Keywords: mesoporous silica, curcumin, surface charge, hydrophobicity, in vitro release, cell cycle, cell apoptosis

ABSTRACT

Mesoporous silica nanoparticles (MCM-41) with different surface chemistry were used as carrier system to study its influence on drug delivery and anticancer activity of curcumin (CUR). CUR was encapsulated in pristine MCM-41 (hydrophilic and negatively charged), amino functionalized MCM-41 (MCM-41-NH_2 which is hydrophilic and positively charged) and methyl functionalized MCM-41 (MCM-41-CH_3 which is hydrophobic and negatively charged) and evaluated for *in vitro* release and cell cytotoxicity in human squamous cell carcinoma cell line (SCC25). Various techniques were employed to evaluate the performance of these materials

on cellular uptake and anticancer activity in SCC25 cell line. Both positively and negatively charged surface demonstrated enhanced drug release and anticancer activity compared to pure curcumin. Positively charged nanoparticles showed higher cell uptake compared to negatively charged nanoparticles owing to its electrostatic interaction with cells. However, hydrophobic surface modified nanoparticles (MCM-41-CH_3) showed no improvement in drug release and anticancer activity due to its poor wetting effect. Cell cycle analysis and cell apoptosis studies revealed different pathway mechanisms followed by the positively and negatively charged nanoparticles but exhibiting similar anticancer activity in SCC25 cells.

1. INTRODUCTION

Cancer is a complex, multifactorial disease that results from strong interplay between genetic, environmental, viral, social and behavioral factors where majority of the therapeutic modality become increasingly ineffective. A recent report projects 1% annual increase in cancer occurrence and mortality, leading to about 26.8 and 17.1 million new cancer cases and cancer related deaths respectively every year by 2030.[1] Hence, development of more effective therapy to combat cancers is urgently needed. The challenges in cancer chemotherapy are associated with adverse toxicity leading to damage of normal cells and tissues; and resistance mediated inactivation of drugs.[2] A growing urge to develop multi-targeted anti-cancer drug molecules from natural products derived phytochemicals have become a focus of modern research due to their minimal side effects and potent chemo-preventive properties.

Curcumin, a natural phytochemical was reported to inhibit the proliferation of multiple cancer cells including breast, colon, pancreas, gastric, liver, blood, lung, prostate, bladder, cervix, ovary, head and neck, brain, multiple myeloma, leukemia, and lymphoma by arresting them in various

phases of the cell cycle and by inducing apoptosis.[3,4] The anti-cancer properties of curcumin are mediated through regulation of various transcription factors, growth factors, inflammatory cytokines, protein kinases, and other enzymes. Curcumin induced therapeutic efficacy against cancers, inhibition of angiogenesis and metastasis in animal models are reported and its anti-cancer potential has been studied in clinical trials.[5] Curcumin being a potent anti-cancer molecule targets many signaling pathways however; its therapeutic efficacy is hindered by non-specific delivery, suboptimal tissue distribution, and rapid metabolism culminating suboptimal bioavailability due to poor aqueous solubility.[6,7]

Curcumin delivery systems such as surfactant complexes, liposomes, hydrogels, and polymeric nanoparticles have been developed to alleviate these issues with limited success due to their synthesis complexity and poor biological stability.[8-10] Mesoporous silica nanoparticles (MSNs) with rigid inorganic frameworks have attracted increasing attention as drug delivery carriers[11,12] owing to their unique properties.[13] Earlier, curcumin was either encapsulated in cetyltrimethylammonium bromide (CTAB) micelle followed by silica coating[14] or encapsulated in modified silica particles as model drug to evaluate its pH dependent *in vitro* release performance[15,16] or conjugated with solid silica to demonstrate its cytotoxic activity.[17] However, the surfactant used in the study (CTAB) is reported to be toxic to the cells[18,19] or ammonia which was used as the reagent can lead to curcumin instability as alkaline condition degrades curcumin[20] or the release medium selected could degrade curcumin.[21] In our previous studies we have demonstrated enhanced curcumin release and cell cytotoxicity by encapsulating it in MSNs.[22] Surface charge and hydrophobicity of MSNs are important parameters which are reported to modulate the drug release and its activity.[23,24] It is well reported that the positively charged particles demonstrate higher endocytosis in cancer cells due to electrostatic attraction as

these cells are negatively charged. There are few studies which report the hydrophobicity helps in controlling drug release.[25] We would like to study the influence of surface functionalisation of MSNs on cellular response when encapsulated with curcumin.

In this work, we report the influence of surface charge and hydrophobicity on curcumin's release and cell cytotoxicity by encapsulating CUR in pristine MCM-41 (hydrophilic and negatively charged), amino functionalized MCM-41 (MCM-41-NH_2 which is hydrophilic and positively charged) and methyl functionalized MCM-41 (MCM-41-CH_3 which is hydrophobic and negatively charged). It is observed that, MCM-41-CUR displays higher drug release compared to MCM-41-NH_2-CUR and MCM-41-CH_3-CUR (Scheme 1). Moreover, the cellular uptake was found to be higher for MCM-41-NH_2-CUR compared to MCM-41-CUR. Cell inhibitory studies demonstrated similar cytotoxic activity by MCM-41-CUR and MCM-41-NH_2-CUR. Flow cytometry and cell apoptosis studies conducted to understand the mechanism followed by these nanoparticles suggests different mechanisms followed by them but still displaying similar anticancer activity which were comparable to the organic CUR-DMSO solution.

2. MATERIALS AND METHODS

2.1 Materials

Cetyl trimethylammonium bromide (CTAB), tetraethoxy orthosilicate (TEOS), (3-Aminopropyl) triethoxysilane (APTES), chlorotrimethylsilane (TMCS), sodium lauryl sulphate (SLS) and Curcumin (CUR) were purchased from Sigma-Aldrich. Reagent grade sodium hydroxide (NaOH) was received from ChemSupply. Methanol AR and Toluene was purchased from RCI labscan and Merck respectively. Human squamous cell carcinoma SCC25 cell line was a kind gift of Prof. Nicholas Saunders from the Princess Alexandra Hospital, Brisbane. Dulbecco's

Modified Eagle Medium: Nutrient Mixture F-12 (DMEM/F12) media was purchased from Sigma. Fetal calf serum was purchased from Moregate biotech. Paraformaldehyde and antifade fluorescent mounting medium with 4'-6-diamidino-2-phenylindole (DAPI), Thiazolyl Blue Tetrazolium Bromide (MTT) cell viability dye, Propidium iodide (PI), Ribonuclease A were purchased from Sigma-Aldrich. Annexin V-FITC kit was from BD Biosciences.

2.2. Characterization

X-ray diffractograms (XRD) were recorded on a Rigaku Miniflex X-ray diffractometer with Fe-filtered Co radiation (λ = 1.79 Å). Transmission electron microscopy (TEM) images were obtained with a JEOL 1010 operated at 100 kV. Nitrogen physisorption measurements were carried out at -196 °C by using a Micromeritics Tristar II 3020 system. MCM-41, MCM-41-NH_2 and MCM-41-CH_3 sample were degassed at 100 °C whereas MCM-41-CUR, MCM-41-NH_2-CUR and MCM-41-CH_3-CUR samples were degassed at 50 °C overnight on a vacuum line. The pore-size distribution was measured from the adsorption branch of the isotherm using BJH model. Fourier transform infrared (FTIR) spectra were recorded on ThermoNicolet Nexus 6700 FTIR spectrometer equipped with Diamond ATR (attenuated total reflection) Crystal. For each spectrum, 128 scans and 4 cm^{-1} resolution was applied over the range of 400–4000cm^{-1}. Raman scattering studies were carried out using a laser excitation wavelength of 780 nm using the Nicolet Almega Visible Raman spectrometer. For each spectrum, 32 scans and 4 cm^{-1} resolution was applied over the range of 400–4000cm^{-1}. Zeta potential was measured on a Malvern Zetasizer Nano-ZS. The thermogravimetric (TGA) and Differential Scanning Calorimetry (DSC) measurements were performed by a Setaram TG92 instrument with a heating rate of 2 °C/min in

air flow. Curcumin concentration was determined using UV-VIS spectrophometer (Shimadzu UV-2450).

2.3. Synthesis of MCM-41

MCM-41 synthesis was performed according to the previously reported method by Yang et al. with slight modification.[26] Briefly, 1.0 g of CTAB was dissolved in 480 g of deionized water at room temperature and kept under stirring until clear solution. 3.5 mL of NaOH (2 M) was added to this solution and temperature increased to 80 °C. Once the solution reaches 80 °C, 6.7 mL of TEOS was added into the mixture as the silica source under continuous stirring for an additional 2 h. The resultant product was obtained by filtration and dried at room temperature. The as-synthesized MCM-41 was divided into three parts. One part was calcined at 550 °C for 5 h to remove the surfactant template and denoted as MCM-41. Second part was calcined in a process similar to the first one and subjected to methyl modification process and denoted as MCM-41-CH_3. The remaining as-synthesized MCM-41 was utilized for amino modification and the surfactant template was removed by solvent extraction process. This material was denoted as MCM-41-NH_2. Two different method of surfactant removal were employed to obtain materials with similar pore size after the functionalization process.

2.4. Synthesis of methyl modified MCM-41

Methyl modification on MCM-41 was performed according to published report.[27] 0.4 g of calcined MCM-41 was added to 20 mL of TMCS solution in toluene with a concentration of 5 wt% under stirring at 70 °C. This suspension was stirred for additional 24 h at 70 °C. The methyl

functionalized MCM-41 was then centrifuged and washed with toluene and ethanol. The material was then dried at 50 °C overnight before subjected to further studies.

2.5. Synthesis of amino modified MCM-41

Amino modification was performed according to published report with slight changes.[28] 0.4 g of as-synthesized MCM-41 was added to 25 mL of methanol under stirring at RT followed by the addition of 1.5 mL of APTES. The suspension was stirred overnight at RT. The amino functionalized MCM-41 with surfactant template still present in it was then retrieved by centrifugation and washed with methanol twice. The material was then dried at 50 °C overnight before subjected to solvent extraction process for surfactant template removal.

Surfactant template was removed by a reported method by Lu et. al.[29] with some modification. 0.3 g of material was added to 32 mL of methanol under stirring and the temperature was increased to 60 °C. To this suspension, 2.0 mL of conc. HCl was added and kept under continuous stirring for 36 h. Later the suspension was centrifuged and washed with methanol twice to ensure complete surfactant removal. The final product was dried at 50 °C overnight to be used for further studies.

2.6. Curcumin loading

Curcumin loading was performed using rotary evaporation technique.[22] 160 mg of MCM-41 was placed in rotary evaporation flask and 40 mg of Curcumin was added to it followed by the addition of 10 mL of methanol. This mixture was sonicated for 2 mins and the solvent was slowly evaporated using rotary evaporator at 50 °C with circulating water temperature maintained at 5 °C to obtain curcumin loaded MCM-41. Evaporation process was continued till

all the solvent is removed and dried powder can be observed in the flask. Dried Curcumin loaded MCM-41 sample (MCM-41-CUR) was collected from the flask and used for further studies. Similar procedure was followed for MCM-41-NH_2 and MCM-41-CH_3 materials. Dried curcumin loaded MCM-41-NH_2 and MCM-41-CH_3 materials are denoted as MCM-41-NH_2-CUR and MCM-41-CH_3-CUR respectively.

2.7. *In vitro* release studies

The *in vitro* release of curcumin from MCM-41-CUR, MCM-41-NH_2-CUR and MCM-41-CH_3-CUR was evaluated using dialysis bag technique.[30,31] MCM-41-CUR equivalent to 1 mg of CUR was weighed and suspended in 1 mL of 0.5 % SLS. This suspension was then placed in dialysis bag with 10 kDa molecular weight cutoff and was immersed into 9 mL of 0.5 % SLS at 37 °C with continuous stirring. At predetermined time intervals, 1 mL of the samples were withdrawn and immediately replaced with an equal volume of dissolution medium to maintain the sink condition. These samples were then properly diluted and analyzed for curcumin content at 432 nm using UV-VIS spectrophotometer. Similar process was performed for MCM-41-NH_2-CUR and MCM-41-CH_3-CUR materials to evaluate their drug release and compared with pure CUR (1 mg).

2.8. *In vitro* cytotoxicity assay

The human squamous cell carcinoma SCC25 cell line was propagated in a monolayer to sub-confluency at 37°C in 75 cm^2 flasks containing 10 mL of DMEM:F12 media, supplemented with heat inactivated 10% fetal calf serum (FCS), 1% penicillin, 1% glutamine and 1% streptomycin and hydrocortisone (0.4µg/mL) in a fully-humidified incubator containing 5% CO_2 and 95% air.

The sensitivity of SCC25 cells to the curcumin nano-formulation was determined by the MTT colorimetric assay. Cells (1×10^4 per well) were seeded in a flat-bottomed 96-well plate and incubated at 37 °C and in 5% CO_2. Cells were exposed to blank MSNs or encapsulated with curcumin at the concentrations of 15, 30, and 45 μg/mL in a dose and time dependent manner for 24, 48 and 72 h. Cells were then treated with MTT reagent (10 μL/ well volume from 5 mg/ mL solution in PBS) for 4 h at 37 °C. Then DMSO (100 μL) was added to each well to dissolve the formazan crystals. The optical density (OD) was recorded at 570 nm in a microplate reader and percentage of residual cell viability was determined. All experiments were performed in triplicate.

2.9. Measuring curcumin delivery *in vitro* by confocal microscopy

The autofluorescence of curcumin (Ex = 480 nm – 530 nm) was used to measure the curcumin uptake by SCC25 cells by confocal microscopy. Briefly, SCC25 cells were seeded onto glass coverslips (Nalge NUNC International, Rochester, New York) at a density of 2×10^5 cells per well and cultured overnight. The next day, the culturing media was removed, and replaced with serum free medium containing CUR in DMSO, CUR in DMEM, MCM-41, MCM-41-NH_2, MCM-41-CUR or MCM-41-NH_2-CUR at a final curcumin concentration of 15 μg/ mL. After incubation at 37 °C for 4 hours, the media were removed from the cells, washed with PBS, fixed with 4% w/w paraformaldehyde in PBS and imaged at 630X magnification using a Zeiss LSM 710 META confocal microscope (Carl Zeiss, Thornwood, New York).

2.10. Silica ICP-OES study

This study was carried out to measure the silica nanoparticles endocytosis performance in human squamous cell carcinoma SCC25 cells (5×10^4 cells per well of 6 wells plate) for MCM-41-CUR and MCM-41-NH_2-CUR. The SCC25 cells were treated similar condition as mentioned in MTT assay and cells from each treatment were washed twice with cold phosphate-buffered saline (PBS, pH 7.4). The cells from both groups were collected separately after 4 and 24 h following trypsinization and then washed twice with PBS and centrifuged at 5000 rpm for 10 min. Cell lysate were prepared in 200µL ice-cold (4 °C) 1X cell lysis buffer (20 mM Tris-HCl (pH 7.5), 150 mM NaCl, 1 mM Na_2EDTA, 1 mM EGTA, 1% Triton, 2.5 mM sodium pyrophosphate, 1 mM beta-glycerophosphate, 1 mM Na_3VO_4, 1 µg/mL leupeptin) followed by sonication. Cell lysates were then centrifuged for 10 minutes at 14,000 rpm at 4 °C and pellet fractions were collected and dissolved in 200µL of 1M NaOH solution. The collected samples (n=3) were then diluted in PBS and sent to the Agricultural Biotechnology Center at University of Queensland for ICP analysis of Si and expressed in mg/L unit.

2.11. Cell Cycle analysis

For the analysis of cell cycle, SCC25 cells treated with CUR in DMSO, CUR in DMEM, MCM-41-CUR, MCM-41-NH_2-CUR (15 µg/mL) were fixed in chilled 70% ethanol and were labeled with PI (50 µg/mL) and RNase (100 µg/mL) for 30 min before the analysis by flow cytometry (BD LSR II Analyser) with Multi-cycle system software package. For each measurement, at least 10,000 cells were counted. Cell cycle analysis was performed for 24 h to evaluate the activity based on different cell cycle phase.

2.12. Annexin V / PI staining

SCC25 cells were treated with CUR in DMSO, CUR in DMEM, MCM-41-CUR, MCM-41-NH_2-CUR (15 μg/mL) for 24 h and were harvested and washed with PBS after the treatment. The cells were first incubated with 100 μL of binding buffer and stained with 5 μL Annexin V-FITC and 5 μL of propidium iodide (PI) from kit according to vendor's instruction (BD Bioscience, Australia) at room temperature for 15 min in the dark. The cells were then analysed by flow cytometry (BD LSR II Analyser) and 10,000 cells were counted. Data were analysed and plotted for Annexin V-FITC and PI in a two-way dot plot. Live, early apoptotic and late apoptotic/necrotic cells are designed as annexin-/ PI-, annexin+/ PI-, and annexin+/ PI+, respectively.

2.13. ROS assay

For cellular ROS measurement, SCC25 cells was seeded on 96 well/plates overnight and next day incubated with the 10-μM carboxy-2',7'-dichloro-dihydro-fluorescein diacetate (DCFH-DA) probe at 37 °C for 30 min. At the end of this period, medium was removed and replaced with fresh serum free medium and cells were treated with CUR in DMSO, MCM-41-CUR and MCM-41-NH_2-CUR at concentration of 15 μg/mL. After initial incubation at CO_2 incubator at 37 °C, fluorescence was measured on a microplate reader (Molecular Devices Spectra MAX) for 0.2-6 h for each time period at 485 nm (excitation) and 527 nm (emission) wavelengths. All assays were performed in triplicate.

3. RESULTS

3.1. Material characterization

The X-ray diffraction (XRD) patterns of MCM-41 (Fig. 1A) show three well resolved diffraction peaks at 2θ of 2.44, 4.27 and 4.93° with a reciprocal d-spacing ratio close to 1: √3: 2, which can be indexed as 100, 110 and 200 reflections of an ordered two dimensional (2D) hexagonal mesostructure with a pore symmetry of p6mm. The positions of three diffraction peaks for MCM-41-CH_3 are similar to that of MCM-41 demonstrating retention of ordered structure after surface functionalization. However, we can observe a shift for the three diffraction peaks in MCM-41-NH_2 compared to that of MCM-41 and MCM-41-CH_3. The diffraction peak positions of MCM-41 materials after curcumin encapsulation was unaltered to that of MCM-41 materials before curcumin encapsulation demonstrating the retention of the ordered structure.

To confirm the crystalline nature of curcumin encapsulated in MCM-41 materials, wide angle XRD (WXRD) study was performed. WXRD patterns (Fig. 1B) were obtained for MCM-41 materials with and without curcumin loading along with the physical mixtures of curcumin and respective MCM-41 materials. Pure curcumin is a crystalline compound showing sharp diffractions in the 2θ range of 10-40°. The amorphous nature of MCM-41, MCM-41-NH_2 and MCM-41-CH_3 materials is evidenced from the broad peak in the range of 2θ 20-30°.[32,33] The physical mixture of three MCM-41 materials and curcumin (MCM-41-CUR PM, MCM-41-NH_2-CUR PM and MCM-41-CH_3-CUR PM) show diffraction peaks corresponding to pure curcumin. However, for curcumin encapsulated MCM-41 materials obtained using rotary evaporation

technique (MCM-41-CUR, MCM-41-NH_2-CUR and MCM-41-CH_3-CUR), no obvious diffraction peaks originating from CUR can be observed.

Typical TEM images of MCM-41, MCM-41-NH_2 and MCM-41-CH_3 are shown in Fig. 2. Because three materials were prepared from the same mother solution, they show similar morphologies as nanoparticles with ~ 100 nm in size. For each particle shown in Figs. 2a-c, parallel channel-like or hexagonally arrayed porous structures can be seen, in accordance with a hexagonal mesostructure. The TEM results also suggest that surface functionalization of MCM-41 in our experiments did not affect the hexagonal structure, consistent with the XRD characterisations.

The nitrogen adsorption/ desorption isotherm of MCM-41, MCM-41-NH_2 and MCM-41-CH_3 correspond to a typical type IV isotherm and show a steep capillary condensation step at a relative pressure (P/P0) range of 0.2-0.4 (Fig. 3A), characteristic of a mesoporous material. From the pore size distribution curves (Fig. 3B), it is shown that MCM-41 material has a pore size of 2.17 nm. MCM-41-NH_2 has a pore size of 2.10 nm, suggesting that the modified amino grafting method helps in achieving pore size similar to MCM-41. MCM-41-CH_3 exhibits a pore size centered at 1.80 nm, suggesting slight decrease in the pore size. After encapsulating curcumin, the pore size of MCM-41-CUR, MCM-41-NH_2-CUR and MCM-41-CH_3-CUR have been decreased to 2.10, 1.91, and 1.73 nm, respectively. The drug encapsulation also results in decrease in surface area and pore volume. For example, the surface area and surface volume for MCM-41-CUR decreases to 450 m^2/g and 0.44 cm^3/g compared to MCM-41 from 995 m^2/g and 0.79 cm^3/g respectively. Similar trend was observed for MCM-41-NH_2-CUR and MCM-41-CH_3-CUR materials as well. All the textural parameters are summarized in Table 1 for comparison.

The surface modification of MCM-41 materials was checked by measuring zeta potential (Z.P.) As shown from Table 1, MCM-41 shows a Z.P. of -36.4 ± 1.42 mV, while MCM-41-NH_2 and MCM-41-CH_3 display Z.P. of 36.3 ± 2.52 and -18.2 ± 1.40 mV, respectively, confirming the successful surface modification of MCM-41 materials. The surface modification is also evidenced by dispersing the materials in ether – water composition as shown in Fig. 3C. Both MCM-41 and MCM-41-NH_2 materials were totally dispersed in aqueous phase with a hazy appearance while MCM-41-CH_3 material was completely dispersed in organic phase

3.2. Adsorption of curcumin

Modification of MCM-41 materials with amino and methyl groups as well as the encapsulation of curcumin in MCM-41 materials was further confirmed by FTIR analysis as shown in Fig. 4. Pristine MCM-41 material exhibits two peaks at 810 and 1060 cm^{-1} (Fig. 4C) and two bands with low intensity at 3745 cm^{-1} and 1630 cm^{-1} (Figs. 4A and 4B). The silanol peak disappeared when amino and methyl modifications are performed on MCM-41. The amino modification resulted in appearance of peaks at 2929, 1631 and 1518 cm^{-1} whereas the methyl modification results in the peak at 2964 cm^{-1} and band of peaks at 1255, 848 and 758 cm^{-1}. Pure curcumin displays a sharp peak at 3507 cm^{-1} and a broad peak at 3293 cm^{-1}. These peaks are not observed in MCM-41-CUR. Instead a new broad peak centered at 3428 cm^{-1} (Fig.4A) can be seen in MCM-41-CUR. Additionally, other typical peaks displayed by pure curcumin can be observed in MCM-41-CUR (Figs. 4B and 4C). Similar results were observed for MCM-41-NH_2 and MCM-41-CH_3 samples. The peak at 1506 cm^{-1} seen in the case of curcumin undergoes a shift to 1513 cm^{-1} in the case of MCM-41-CUR, MCM-41-NH_2-CUR and MCM-41-CH_3-CUR. The peaks due to δ(CCH) of the phenol and skeletal δ(CCH) at 1145 cm^{-1} due to in-plane bending vibrations and the peak at

1023 cm^{-1} due to the in-plane bending vibrations of aromatic keto group δ(CCH) and out of plane vibrations of CH_3, i.e., δ(CH3) of curcumin are masked by the asymmetric Si-O-Si stretching vibrations of MCM-41 materials. The peak at 1272 cm^{-1} due to aromatic keto in-plane vibrations δ(CCH), δ(CCC) and keto-enol δ(COH) are found to have merged with Si-O-Si stretching vibrations of MCM-41 materials. In short all the major peaks of curcumin shown in fig. 4C are hidden by the IR vibrations of MCM-41 materials without curcumin encapsulation in the similar regions. Although we can observe very weak signals in the range of 1400-1500 cm^{-1} in the curcumin encapsulated MCM-41 materials which coincide with the peaks of pure CUR, it does not explains the curcumin encapsulation in MCM-41 materials conclusively. Hence, we did the Raman spectra for curcumin encapsulated MCM-41 materials.

Raman spectral studies revealed that the absence of ν(C=O) peaks in the region of 1650-1800 cm^{-1} for pure curcumin indicating its existence in enol form rather than its diketone form (Fig. 5).[34] A peak shift was observed from 1633 cm^{-1} for pure curcumin to 1640 cm^{-1} in MCM-41-CUR. Similar results were observed for MCM-41-NH_2-CUR and MCM-41-CH_3-CUR

TGA analysis was used to evaluate the curcumin encapsulation in different samples under study (Fig. 6A). Curcumin concentration loaded in MCM-41-CUR, MCM-41-NH_2-CUR and MCM-41-CH_3-CUR materials by rotary evaporation technique was found to be 20.02 %, 16.95 % and 19.98% respectively indicating high efficiency of rotary evaporation process in accordance with previous reports.[22,35] For comparison, physical mixtures of curcumin and MCM-41, MCM-41-NH_2 and MCM-41-CH_3 materials were prepared. MCM-41-CUR PM, MCM-41-NH_2-CUR PM and MCM-41-CH_3-CUR PM samples showed weight loss of 22.67%, 18.95% and 20.90% respectively (Fig. 7A). The hydrophobic modification inhibits the aqueous wetting of MCM-41-

CH_3 by methyl groups present on the material which is evident by the % wt. loss at 100°C as seen from Fig. 6A and 7A. The moisture loss for MCM-41 and MCM-41-NH_2 is 3 and 9 % whereas 1 % for MCM-41-CH_3 material thus demonstrating the effect of hydrophobicity on moisture uptake.

Differential Scanning Calorimetry (DSC) analysis was performed to determine the crystallinity of curcumin in MCM-41-CUR, MCM-41-NH_2-CUR and MCM-41-CH_3-CUR samples (Fig. 6B). Pure curcumin (CUR) displays a sharp melting point peak at 176°C. A weak signal can be observed for MCM-41-CUR PM, MCM-41-NH_2-CUR PM and MCM-41-CH_3-CUR PM samples (Fig. 7B). However, this peak cannot be observed in MCM-41-CUR, MCM-41-NH_2-CUR and MCM-41-CH_3-CUR samples (Fig. 6B)

3.3. *In vitro* release

To compare the effect of surface charge and hydrophobicity in curcumin encapsulated MCM-41 materials, curcumin release was studied in 0.5% SLS (under sink conditions) as the dissolution medium. After 1 h, the release of curcumin from MCM-41-CUR, MCM-41-NH_2-CUR and MCM-41-CH_3-CUR was found to be 0.67%, 0.38% and 0.76% respectively compared to 0.97% from pure Curcumin (Fig. 8). The drug release profile increased slowly for MCM-41-CUR (28.0%), MCM-41-NH_2-CUR (22.63%) and MCM-41-CH_3-CUR (19.35%) after 72 h compared to pure curcumin (11.19%). MCM-41-CUR showed higher curcumin release compared to MCM-41-NH_2-CUR, MCM-41-CH_3-CUR and pure curcumin at all time points.

3.4. *In vitro* cytotoxicity of curcumin

To determine the efficacy of curcumin encapsulated MSNs on cancer cell viability, MTT assay was conducted on human squamous cell carcinoma SCC25 cell line. SCC25 cells were treated for 24, 48 and 72 h with 0, 15, 30 and 45 μg/mL concentrations of free curcumin (curcumin in DMEM and curcumin in DMSO) and equivalent doses of MCM-41-CUR and MCM-41-NH_2-CUR and MCM-41-CH_3-CUR dispersed in DMEM. Respective blank MSNs without curcumin loading were also evaluated as control groups (Fig. 9).

As shown in Fig. 9, CUR-DMEM shows dose and time dependent toxicity until 48 h with no further improvement on exposing them for longer duration (72 h). The maximum cell viability demonstrated by CUR-DMEM was 50 % at 48 h at the dose of 45 ppm. On the contrary, CUR-DMSO showed a strong inhibitory effect on cell viability within 24 h which was further increased at 48 h and 72 h demonstrating the anticancer potency of curcumin. MCM-41-CUR showed a dose dependent decrease in cell viability within 24 h which was maintained up to 72 h. Similarly, MCM-41-NH_2-CUR induced a dose dependent inhibition on SCC25 cell viability within 24 h which were further potentiated at 48 h and 72 h. On the other hand, MCM-41-CH_3-CUR induced minimal cytotoxicity and hence, we have omitted MCM-41-CH_3-CUR group from all further biological studies. Interestingly, the cell inhibitory potential of MCM-41-CUR (at 72 h) and MCM-41-NH_2-CUR (at 48 h and 72 h) are very well comparable to that of CUR-DMSO which is far more potent than CUR-DMEM response. These observations show the advantages of nanoparticles mediated delivery of curcumin in aqueous based formulation to exert desirable therapeutic effect and to avoid organic solvent toxicity. None of the blank MCM-41

nanoparticles showed reduction in cell viability up to 72 h indicating their biocompatibility and bioinertness.

3.5. Cellular uptake studies

Cell uptake efficiency for curcumin by CUR-DMEM, CUR-DMSO, MCM-41-CUR and MCM-41-NH_2-CUR in SCC25 cells was studied by confocal microscopy. The curcumin uptake by SCC25 cells from all four formulations – CUR-DMEM, CUR-DMSO, MCM-41-CUR or MCM-41-NH_2-CUR, showed a marked difference in curcumin levels compared with untreated control group (Fig. 10). Cells incubated with CUR-DMEM for 4 hours had very nominal and undetectable curcumin level. MCM-41-NH_2-CUR showed highest accumulation in cell cytosol whereas CUR-DMSO and MCM-41-CUR both showed relatively reduced level of curcumin accumulation in cytosol. CUR-DMSO had organic solvent, DMSO which is able to dissolve curcumin completely and thus is well accumulated inside SCC25 cells. MCM-41-NH_2-CUR showed superior curcumin uptake compared to MCM-41-CUR.

To further support the cell uptake studies, silica content was measured by silica inductively coupled plasma atomic emission spectroscopy (ICP-OES) study. MCM-41-CUR and MCM-41-NH_2-CUR were incubated with SCC25 cells for 4 and 24 h and measured for their silica content. Positively charged MCM-41-NH_2-CUR showed higher Si content at 4 h compared to the negatively charged MCM-41-CUR (Fig. 11). However, with further incubation (24 h) the Si content reduced for MCM-41-NH_2-CUR while it was unchanged for MCM-41-CUR

3.6. Cell cycle and apoptosis studies

To determine the impact of four curcumin formulations – CUR-DMEM, CUR-DMSO, MCM-41-CUR and MCM-41-NH_2-CUR on the cell cycle, SCC25 cells were treated with 15 μg/mL equivalent curcumin concentrations for 24 h. PI stained cells were analysed by flow cytometry analysis to determine alterations in distribution of cells in different phases of cell cycle (Fig. 12). Results from flow cytometry analysis in SCC25 cells showed that treatment with CUR-DMEM, blank MCM-41 and blank MCM-41-NH_2 did not alter the cell cycle compared with the untreated control group. In contrast, CUR-DMSO, MCM-41-CUR and MCM-41-NH_2-CUR treatment caused marked increase in S and G2/M-phases of cell cycle leading to cell death (Fig. 12). The G0/G1 phase significantly decreased from 65% for untreated control group to 36%, 30% and 28% for CUR-DMSO, MCM-41-CUR and MCM-41-NH_2-CUR respectively. Furthermore, a concomitant increased in S and G2/M phases was observed for CUR-DMSO (S= 35% and G2/M= 28%), MCM-41-CUR (S= 49% and G2/M= 22%) and MCM-41-NH_2-CUR (S= 33% and G2/M= 39%) when compared with untreated control group (S= 27% and G2/M= 8%).

To further investigate the link between cell cycle arrest and the mode of cell death, AnnexinV-FITC/PI staining assay was used to confirm SCC25 cell death by apoptosis (Fig. 13). SCC25 cells were treated with 15 μg/mL equivalent curcumin concentrations from four formulations along with respective control blank nanoparticles for 24 h. Treatment with CUR-DMEM, MCM-41 and MCM-41-NH_2 blank particles did not alter the apoptotic cell death and were comparable to untreated control cells. These results are similar to the *in vitro* cytotoxicity studies confirming the bio-inertness and biocompatibility of MSNs. On the contrary, CUR-DMSO, MCM-41-CUR and MCM-41-NH_2-CUR significantly induced apoptosis in SCC25 cells compared with

untreated control cells. CUR-DMSO treated cells showed 9% and 90% of early apoptotic (AnnexinV-FITC+/PI−) and late apoptotic/early necrotic (AnnexinV-FITC+/PI+) populations respectively, compared to MCM-41-CUR (11% and 88%) and MCM-41-NH_2-CUR (15% and 82%) treated cells at 15 μg/mL dose for 24 h. These results indicate that both MCM-41-CUR and MCM-41-NH_2-CUR had similar cell apoptosis which is on par compared with CUR-DMSO.

3.7. ROS assay

Curcumin is known to induce apoptosis by increasing the generation of ROS.[36] Thus, we studied the effect of all the three formulations (CUR-DMSO, MCM-41-CUR and MCM-41-NH_2-CUR) on generation of ROS at a single dose (15μg/mL) in a time dependent manner (Fig. 14). We have excluded CUR-DMEM due to lack of efficacy for inducing apoptosis. It was observed that, at equivalent dose, the ROS generation levels are MCM-41-NH_2-CUR> MCM-41-CUR> CUR-DMSO. This ROS helps to induce mitochondrial damage leading to apoptosis. In our study, CUR-DMSO, MCM-41-CUR and MCM-41-NH_2-CUR treatment caused ROS generation mediated mitochondrial damage as revealed from reduction in MTT value and the AnnexinV-FITC assay further confirm apoptosis in SCC25 cells.

4. DISCUSSION

In the current investigation, the effect of surface functionalization on anticancer activity was studied by encapsulating curcumin in MCM-41 type MSNs in SCC25 cell line. Positively charged, negatively charged and hydrophobic MSNs were synthesized to study this work. These nanoparticles were characterized using various techniques such as XRD, WXRD, nitrogen physiosorption, FTIR, Raman spectroscopy and further evaluated for their performance by

studying their *in vitro* release, *in vitro* cytotoxicity, cell uptake, silica content, flow cytometry and cell apoptosis. The XRD pattern revealed three well resolved diffraction peaks for MCM-41, MCM-41-NH_2 and MCM-41-CH_3 (Fig. 1A). The diffraction peak positions for MCM-41-NH_2 are observed to shift at a lower 2θ. This shift at lower 2θ is due to the solvent extraction method employed for the surfactant template removal resulting in decreased silanol condensation compared to that of calcination process used for the synthesis of MCM-41 and MCM-41-CH_3.[27] WXRD study (Fig. 1B) conducted to confirm the crystalline nature of curcumin showed that MCM-41-CUR PM, MCM-41-NH_2-CUR PM and MCM-41-CH_3-CUR PM display diffraction peaks corresponding to pure curcumin indicating the crystalline nature of CUR in them. However, we cannot observe such peaks for MCM-41-CUR, MCM-41-NH_2-CUR and MCM-41-CH_3-CUR materials suggesting that CUR is entrapped inside the nanopores with an amorphous nature.[32,33] Nitrogen physiosorption studies (Fig. 3A, B) reveal the surface parameters of the MSNs synthesized with different surface chemistry and after encapsulating curcumin in them. The modified method for grafting amino groups on MCM-41 helps in attaining similar pore size as MCM-41. A small amount of the silica source (APTES) can replace the surfactants during the post-modification process starting from the as-synthesized MCM-41 resulting in decreased pore size.[28] If the post-modification of amino groups starts from MCM-41 after removing the surfactants, the pores will be blocked (data not shown).[37] The change in pore size of MCM-41-CH_3 is due to the presence of small amount of methyl groups in pore channels during the modification process. Our observation is consistent with previous reports on the hydrophobic modification of mesoporous materials after removing the surfactants, where the pore size is reduced by 0.25 – 0.65 nm.[27,38] On encapsulating curcumin in these materials we can observe change in pore size, surface area and pore volume indicating successful loading of CUR inside

the nanopores. The successful surface modification on MCM-41 materials was confirmed by dispersing them in ether – water composition which showed that MCM-41 and MCM-41-NH_2 materials were totally dispersed in aqueous phase indicating their hydrophilic nature. On the other hand MCM-41-CH_3 material was dispersed completely in organic phase displaying its hydrophobic nature.

The peaks displayed by MCM-41 in FTIR analysis at 810, 1060, 1630 and 3745 cm^{-1} (Fig. 4A-C) can be indexed to symmetric and asymmetric Si–O–Si stretching (νs(Si-O-Si), νa(Si-O-Si)), bending mode of physiosorbed water and to the isolated silanol (ν(O-H)) respectively.[39,40] The peaks observed on amino modification at 2929, 1631 and 1518 cm^{-1} can be attributed to C–H stretching, N–H bending and N–H stretching vibrations of aminopropyl group anchored on the surface of MCM-41.[13,41,42] The peaks observed after methyl modification at 2964 cm^{-1} which can be attributed to C–H vibration and band of peaks at 1255, 848 and 758 cm^{-1} attributed to Si-CH_3 of methyl group from TMCS.[38,43] The sharp peak displayed by pure curcumin at 3507 cm^{-1} and a broad peak at 3293 cm^{-1} is attributed to –OH group vibrations without and with intermolecular hydrogen bonding, respectively.[44] A new broad peak observed in MCM-41-CUR after encapsulating curcumin is due to intermolecular hydrogen bonding between isolated silanol and enolic hydroxyl group.[17] The shift in the peak from 1506 cm^{-1} due to the ν(C=O), δ(CCC) and δ(CC=O) to 1513 cm^{-1} in case of MCM-41-CUR, MCM-41-NH_2-CUR and MCM-41-CH_3-CUR could be taken as an evidence of complex formation.[34] To confirm the encapsulation of curcumin in MCM-41, Raman spectroscopy was performed (Fig. 5). Pure curcumin displays a sharp peak 1633 cm^{-1} corresponding to ν(C=C) and ν(C=O) which is shifted to 1640 cm^{-1} in MCM-41-CUR indicating strong interaction between enolic -OH of curcumin and silanol group of MCM-

41. The similar trend was observed for MCM-41-NH_2-CUR and MCM-41-CH_3-CUR wherein the enolic -OH of curcumin interacts with the silanol groups loacted on the interior surface of MCM-41-NH_2 and MCM-41-CH_3 materials. The successful encapsulation of curcumin in MCM-41 materials is provided by the symmetric aromatic ring stretching vibrations ν(C-C ring) of curcumin at 1605 cm^{-1}. The ratio of intensity of 1633 cm^{-1} peak to that of 1605 cm^{-1} peak is 0.70 for pure curcumin. However, for MCM-41-CUR, MCM-41-NH_2-CUR and MCM-41-CH_3-CUR the ratio of intensity of 1640 cm^{-1} peak to that of 1605 cm^{-1} peak is 1.05, 1.02 and 1.07 respectively suggesting the aromatic ring is in the pores of MCM-41 materials.[34] Thus Raman spectroscopy provided clear and distinct evidence of the curcumin encapsulation in MCM-41 materials. DSC analysis (Fig. 6B, 7B) conducted for MCM-41-CUR PM, MCM-41-NH_2-CUR PM and MCM-41-CH_3-CUR PM samples displays a weak signal at 176°C which corresponds with the sharp melting point peak for pure curcumin indicating the existence of curcumin's crystalline state in their respective physical mixtures. However, no such peak is observed in case of in MCM-41-CUR, MCM-41-NH_2-CUR and MCM-41-CH_3-CUR samples indicating curcumin's non-crystalline state and its successful loading as nano-sized aggregates in the pore channels of these MCM-41 materials.[45,46]

The *in vitro* release studies (Fig. 8) demonstrate faster release of curcumin from MCM-41-CUR which could be attributed to the presence of curcumin as nano-sized aggregates in the pore channels of MCM-41. The comparative slower release of curcumin from MCM-41-NH_2-CUR could be attributed to the APTES grafting on the surface which may impart relatively slight hydrophobicity owing to the aminopropyl chain of APTES leading to slower influx of dissolution media in the pore channels which would eventually delay the dissolution of

curcumin. Also, APTES grafting would impart some steric hindrance inhibiting the release of curcumin from the pore channels.[47] This finding is in accordance with an earlier report using emodin as the drug molecule.[48] The relatively slower curcumin release from MCM-41-CH_3-CUR can be attributed to the poor wetting of the material owing to the hydrophobic methyl group on its surface reducing the interaction of encapsulated curcumin with the aqueous media.[25] This hydrophobic modification results in very slow dissolution of drug resulting in slower release which is also supported by the TGA curve in Fig. 6A. Thus, surface modification by varying the surface charge and hydrophobicity plays an important role in modulating the curcumin release from MSNs.

The *in vitro* cytotoxicity studies (Fig. 9) for CUR-DMEM displayed moderate cytotoxicity which could be due to reduced solubility of curcumin in aqueous medium (DMEM) as curcumin is hydrophobic and aqueous insoluble.[49] CUR-DMSO showed a strong inhibitory effect however, this DMSO formulation has clinical limitation. The minimal cytotoxicity displayed by MCM-41-CH_3-CUR could be attributed to slow release of CUR from the nanoparticles because of poor wetting effect owing to its hydrophobic nature which is also evident from *in vitro* release study. The plausible reason behind higher cell inhibitory efficacy demonstrated by MCM-41-CUR and MCM-41-NH_2-CUR could be due to enhanced release of curcumin from nanoparticles as supported by the *in vitro* dissolution studies. A comparison of MTT results showed greater cell inhibition by MCM-41-NH_2-CUR than MCM-41-CUR at earlier time point (24 h and 48 h) which could be due to positive charge by -NH_2 modification on the particle surface leading to higher endocytosis as reported by previous studies.[50-53]

Cell uptake studies (Fig. 10) showed higher uptake of curcumin from MCM-41-NH_2-CUR owing to its positive charge which helps in electrostatic interaction with the negatively charged cell membrane leading to higher endocytosis. This result is in line with earlier studies which stated, positively charged nanocarriers mediated transport of CUR for effective anti-cancer therapy into the negatively charged cancer cell via enhanced permeation and retention (EPR) effect.[49] The uptake of curcumin from negatively charged MCM-41-CUR suggests different pathways followed by these MSNs to exhibit their effect. Silica content was measured (Fig. 11) to support the cell uptake studies which showed higher cell uptake of MCM-41-NH_2-CUR at 4 h compared to MCM-41-CUR. However on further incubation at 24 h, the silica content decreased by approximately 40% for MCM-41-NH_2-CUR while it remain unchanged for MCM-41-CUR. This result could be attributed to the lysosomal escape of positively charged nanoparticles after being internalized whereas high colocalization of negatively charged nanoparticles with lysosome similar to earlier report.[54]

Cell cycle analysis (Fig. 12) was conducted on four formulations – CUR-DMEM, CUR-DMSO, MCM-41-CUR and MCM-41-NH_2-CUR to understand their influence on cell cycle by treating with 15 μg/mL equivalent curcumin concentrations for 24 h. The data obtained suggests that CUR-DMSO slightly modulates S-phase but mainly affects the G2/M phase of cell cycle in SCC25 cells. On the other hand, MCM-41-CUR markedly affects both S and G2/M whereas MCM-41-NH_2-CUR nanoparticles mildly impacts S-phase and significantly inhibiting G2/M phase. Our observation is in line with a previous study reporting CUR induces dose dependent S and G2/M cell cycle arrest in human cancer cells.[55,56] The diverse effect of MCM-41-CUR and MCM-41-NH_2-CUR could be attributed to their net negative and positive charges respectively but need further investigation. The predominant features of these current data suggests that, both

MCM-41-CUR and MCM-41-NH_2-CUR nanoformulations are potent to deliver curcumin efficiently inside the cancer cells to execute their anticancer therapeutic effect which cannot be achieved by aqueous CUR-DMEM.

AnnexinV-FITC/PI staining assay (Fig. 13) was used to investigate the link between cell cycle arrest and the mode of cell death for the four formulations – CUR-DMEM, CUR-DMSO, MCM-41-CUR and MCM-41-NH_2-CUR. MCM-41-CUR and MCM-41-NH_2-CUR both displayed similar cell apoptosis which was on par with organic CUR-DMSO. The plausible reason for such similar activity by negatively and positively charged nanoparticles could be attributed to the *in vitro* release profile and cell uptake studies. MCM-41-CUR had low cellular uptake in SCC25 cells but displayed faster *in vitro* release which could lead to higher CUR content in the cells to display its apoptotic activity. In the case of MCM-41-NH_2-CUR, it had higher cellular uptake however the *in vitro* release was comparatively slower resulting in CUR content similar to that of MCM-41-CUR. ROS assay was studied (Fig. 14) to investigate if MCM-41-CUR and MCM-41-NH_2-CUR induces ROS generation by the releases curcumin. There are many reports supporting our data and stating that curcumin can generate ROS to damage mitochondria and apoptosis in a variety of cancer cell lines.[57-59] These data further suggests that organic solvent free nanoparticles can display therapeutic efficacy similar to that of control group (using toxic organic solvent) which could have clinical implications in lab to bed side translational research.

5. CONCLUSION

Silica nanoparticles with different surface charge and hydrophobicity were synthesized and encapsulated with curcumin to evaluate its effect on cellular uptake and anticancer activity. It was observed that the encapsulation of curcumin in hydrophilic nanoparticles enhanced drug

release and cell cytotoxicity compared to the hydrophobic nanoparticles. Confocal miscroscopy and silica content studies showed higher cellular uptake of MCM-41-NH_2-CUR compared to MCM-41-CUR. This is because of the electrostatic interaction between positively charged MCM-41-NH_2-CUR and the negatively charged cancer cells. However, the cell cycle analysis and Annexin V-FITC/ PI assay demonstrated similar anticancer activity by both MCM-41-CUR and MCM-41-NH_2-CUR. The similar anticancer activity displayed by positively and negatively charged MSNs could be attributed to their *in vitro* release behaviour and cellular uptake. Thus, in our study, the surface charge variation resulted in similar anticancer activity for curcumin. Moreover, the findings from this study suggests that organic solvent free nanoparticles as promising carriers for gaining higher therapeutic efficacy which could be useful for clinical implications from lab to bed side translational research.

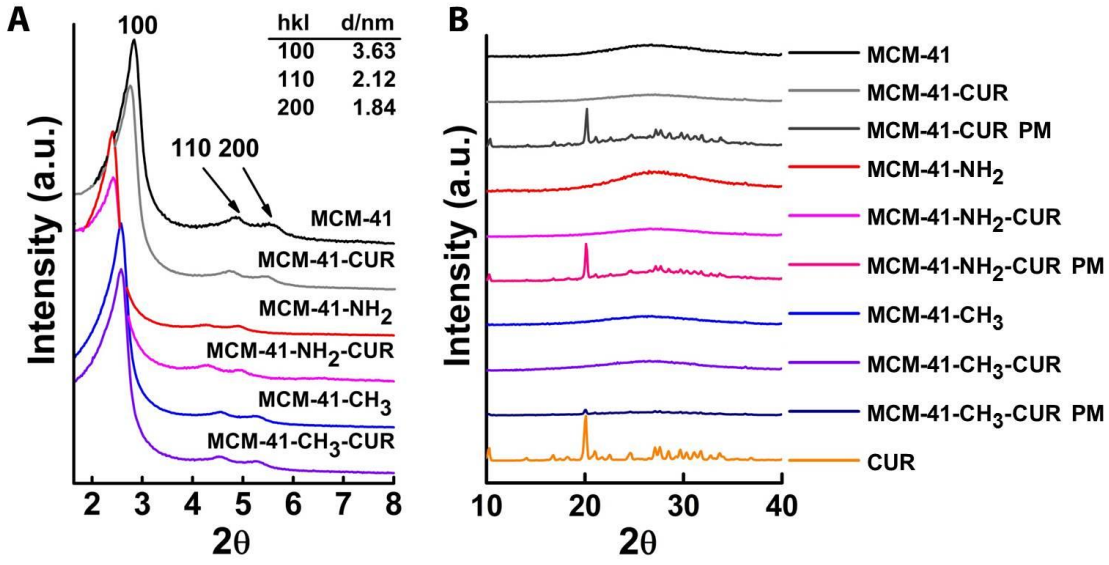

Figure 1. (A) XRD patterns of MCM-41 materials with and without Curcumin loading. (B) WXRD patterns of MCM-41 materials with and without Curcumin loading and physical mixtures of curcumin with unfunctionalized and functionalized MCM-41 materials.

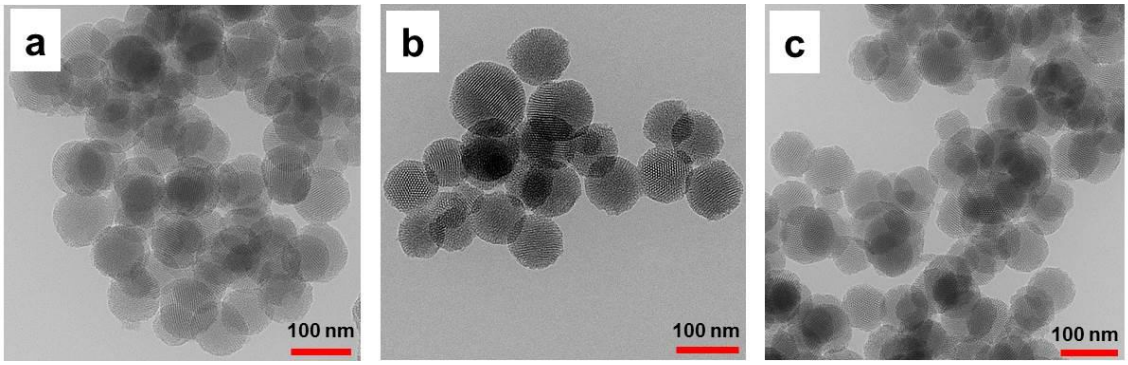

Figure 2. Transmission Electron Microscopy (TEM) image of MCM-41(a), MCM-41-NH_2 (b) and MCM-41-CH_3 (c) materials.

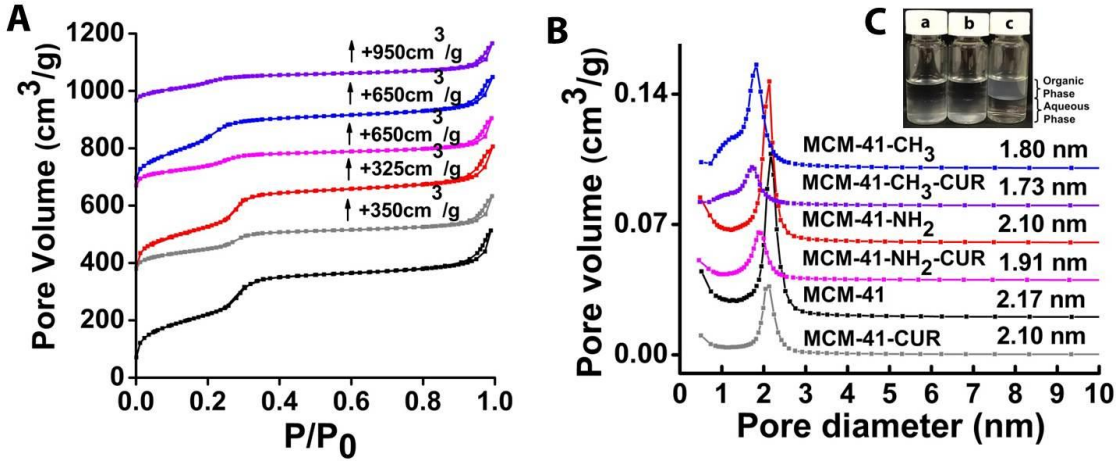

Figure 3. A) N2 adsorption/desorption isotherms and B) BJH pore-size distribution plot for unfunctionalized and functionalized MCM-41 materials with and without Curcumin loading. C) Digital image of a) MCM-41, b) MCM-41-NH_2 and c) MCM-41-CH_3 demonstrating the hydrophobicity of materials by dispersing them in organic (ether) – aqueous (water) composition.

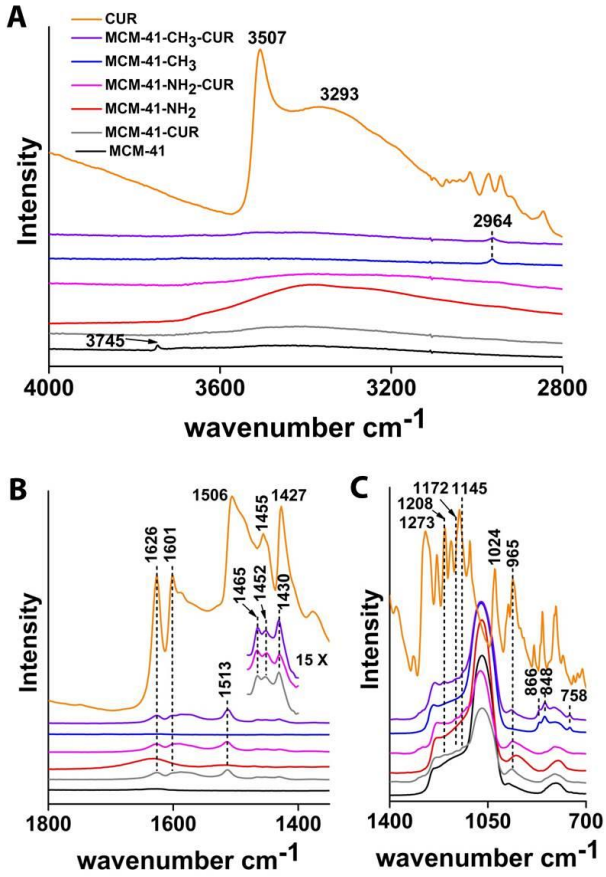

Figure 4. FTIR spectra of unfunctionalized and functionalized MCM-41 materials with and without curcumin loading.

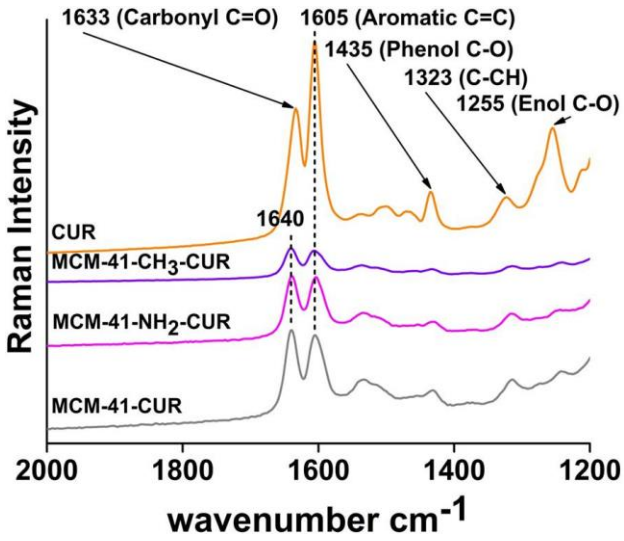

Figure 5. Raman spectra of pure curcumin and functionalized MCM-41 materials encapsulated with curcumin.

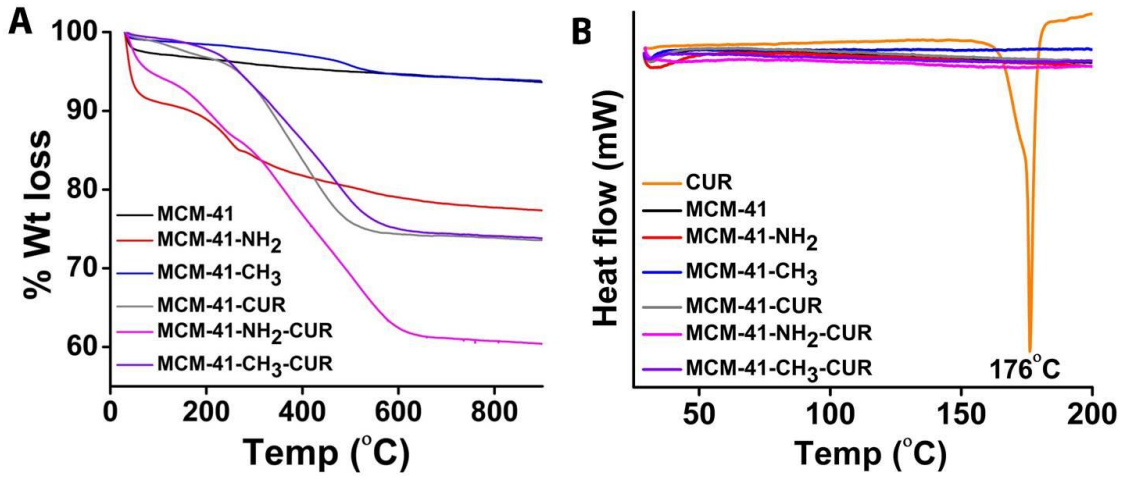

Figure 6. TGA (A) and DSC (B) curves of unfunctionalized and functionalized MCM-41 materials with and without curcumin loading.

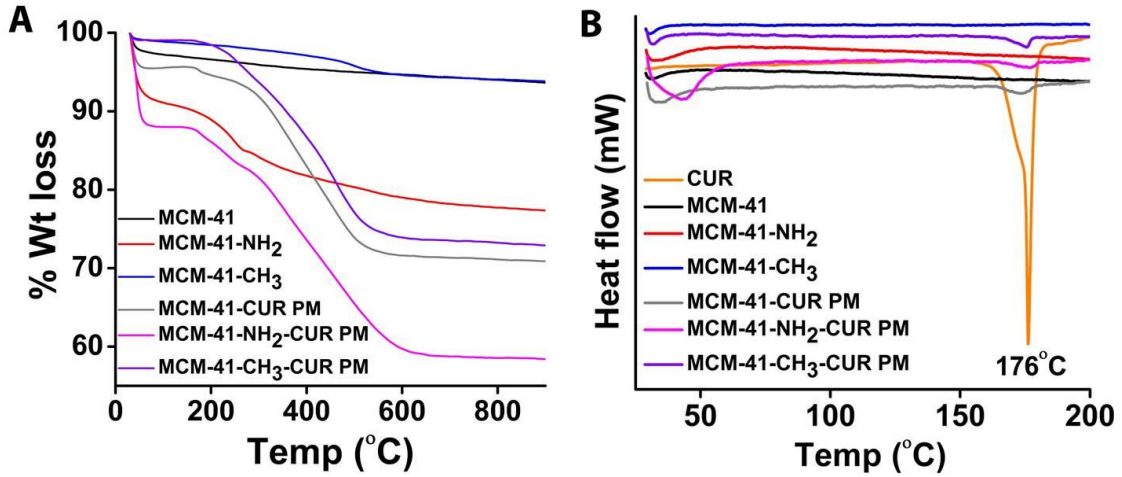

Figure 7. TGA (A) and DSC (B) curves of physical mixtures of curcumin with unfunctionalized and functionalized MCM-41 materials.

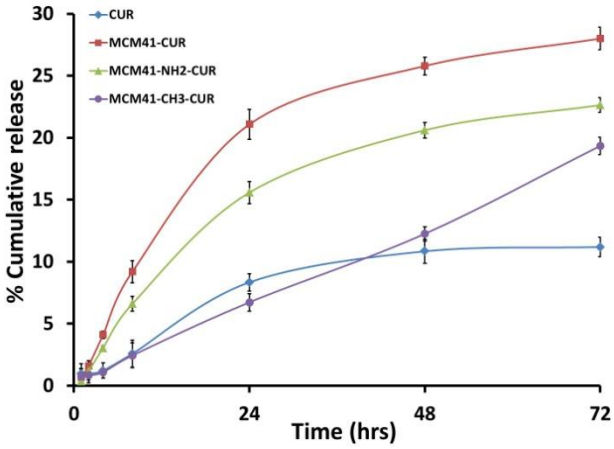

Figure 8. *In vitro* release of pure Curcumin and Curcumin loaded in MCM-41-CUR, MCM-41-NH_2-CUR and MCM-41-CH_3-CUR materials in 0.5% SLS.

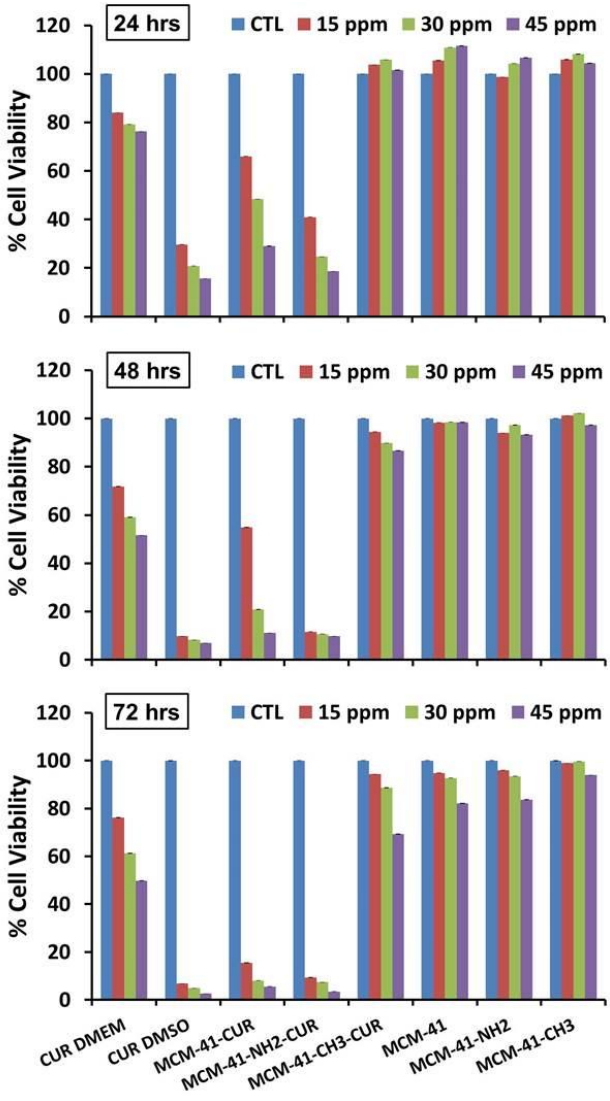

Figure 9. *In vitro* cytotoxicity of pure curcumin, MCM-41-CUR, MCM-41-NH_2-CUR and MCM-41-CH_3-CUR in SCC-25 cell line after 24, 48 and 72h with curcumin equivalent dose of 15 ppm, 30 ppm and 45 ppm respectively.

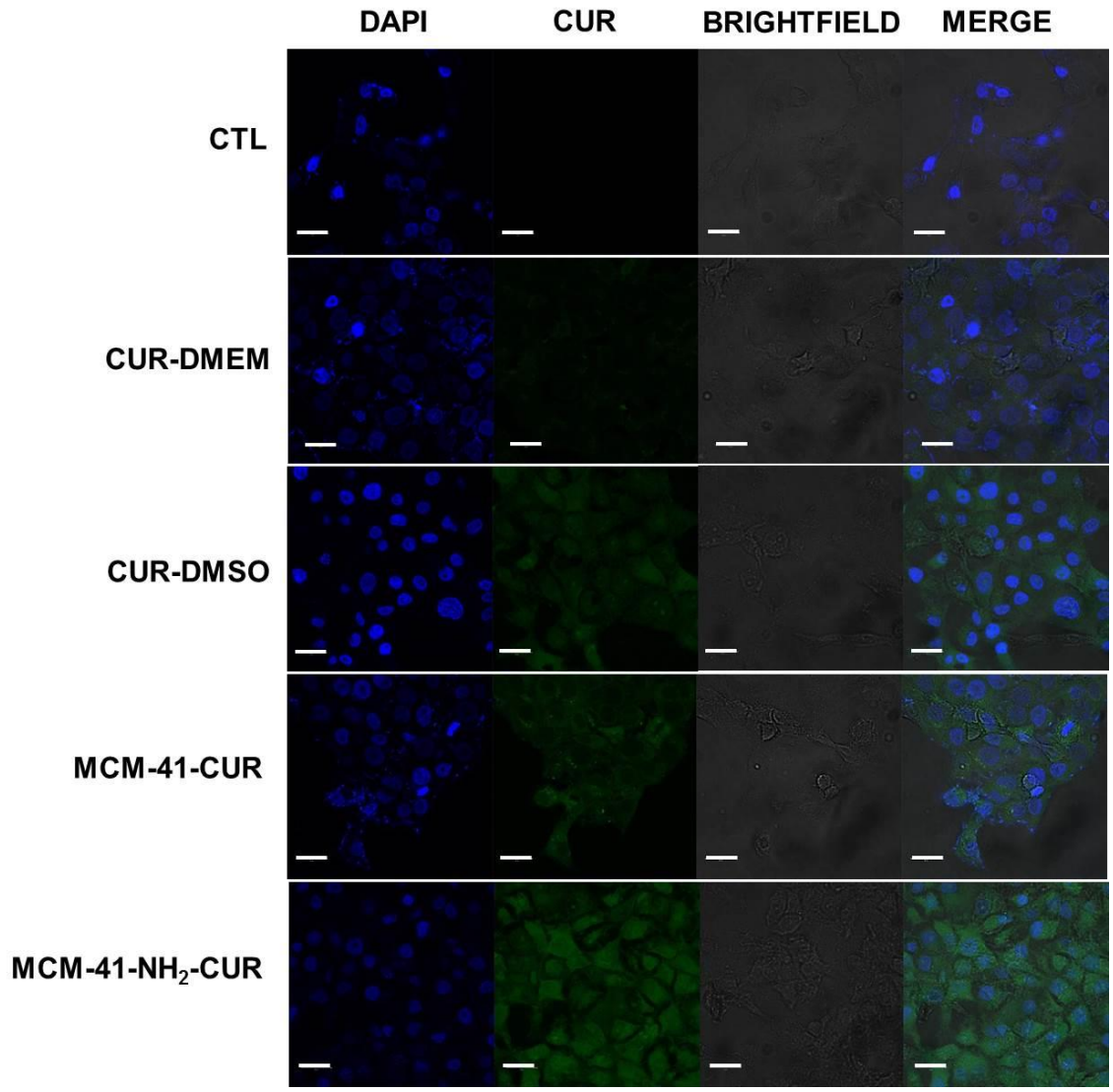

Figure 10. Confocal microscopy images of SCC25 cells without any treatment as control (CTL), CUR-DMEM, CUR-DMSO, MCM-41-CUR and MCM-41-NH_2-CUR. Blue signal denotes the nuclei stained with DAPI and green fluorescence arises from curcumin. Scale bar represents 20 μm.

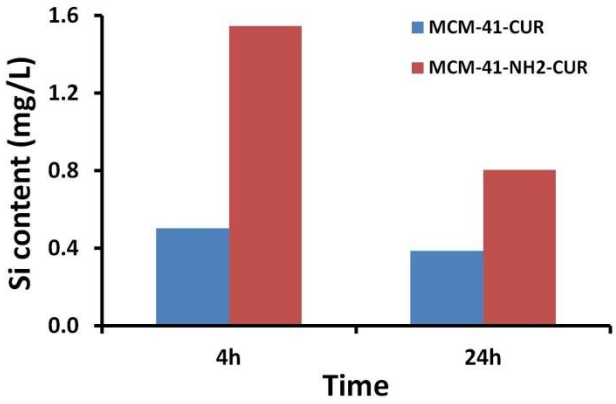

Figure 11. Si concentrations determined by ICP-OES for MCM-41-CUR and MCM-41-NH_2-CUR endocytosed in SCC25 cell line after 4 and 24 h.

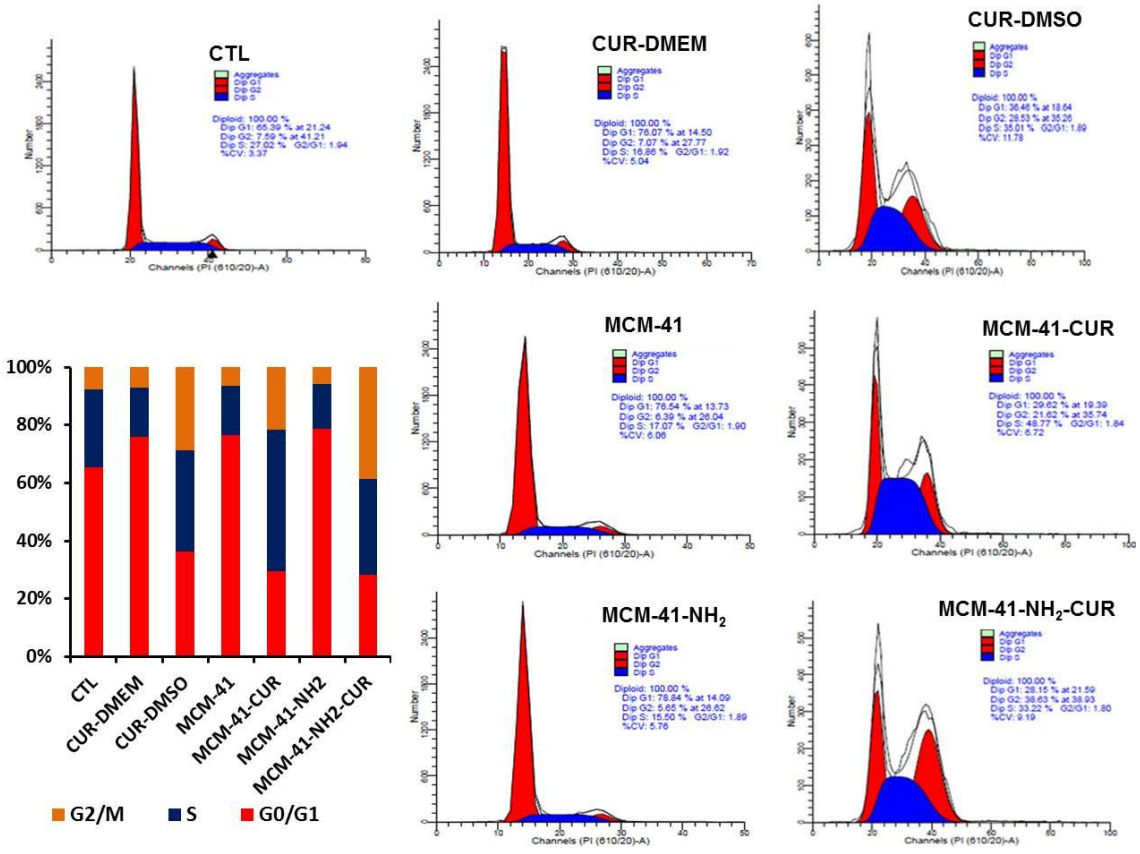

Figure 12. Cell cycle analysis of control (CTL), CUR-DMEM, CUR-DMSO, MCM-41-CUR and MCM-41-NH_2-CUR in SCC25 cells after 24 hrs.

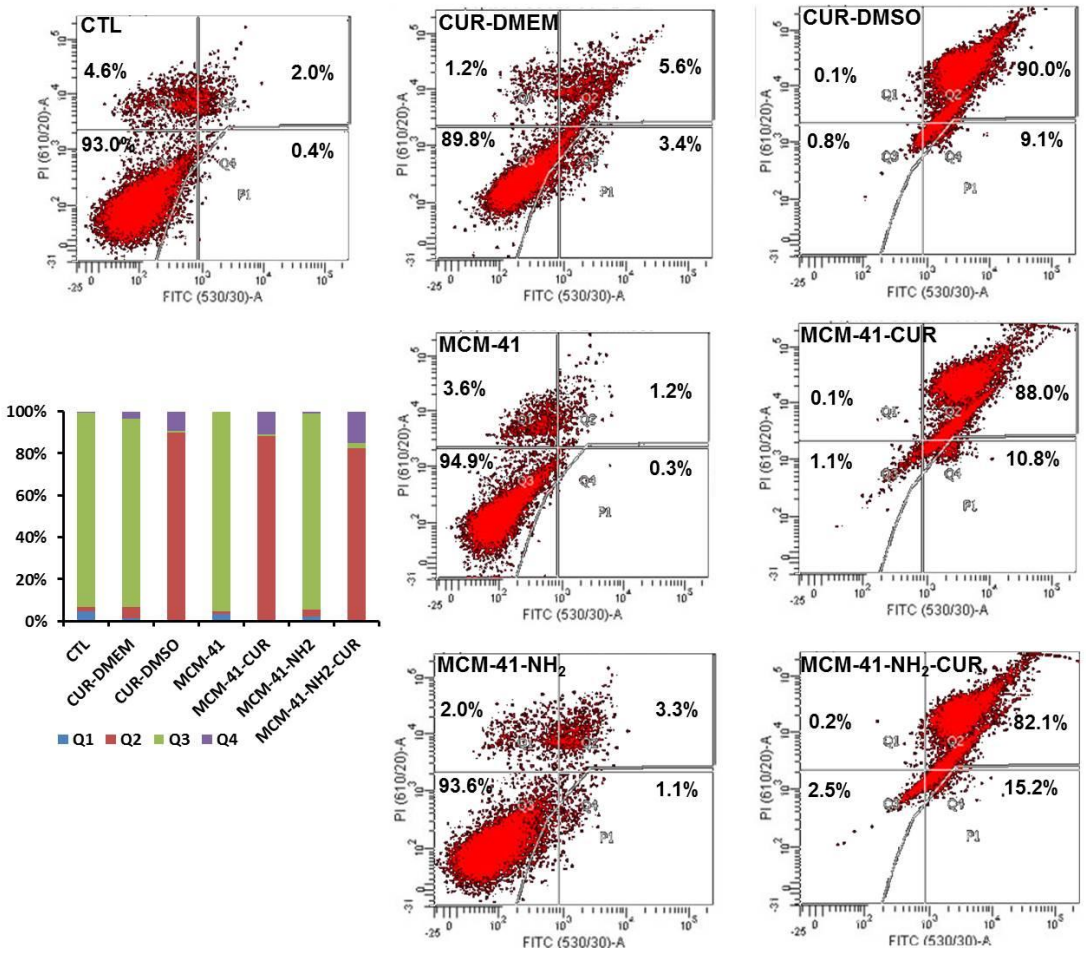

Figure 13. Cell apoptotic studies of control (CTL), CUR-DMEM, CUR-DMSO, MCM-41-CUR and MCM-41-NH_2-CUR with respective control groups in SCC25 cells.

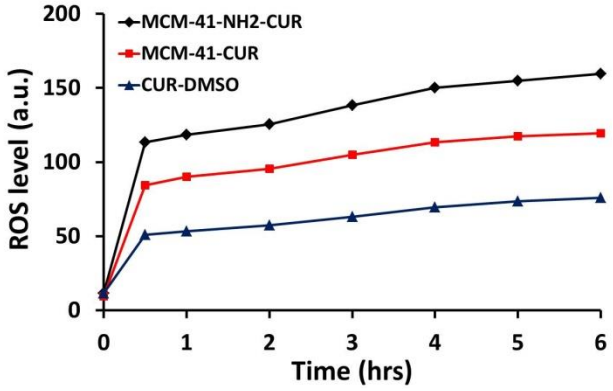

Figure 14. ROS assay of CUR-DMSO, MCM-41-CUR and MCM-41-NH_2-CUR.

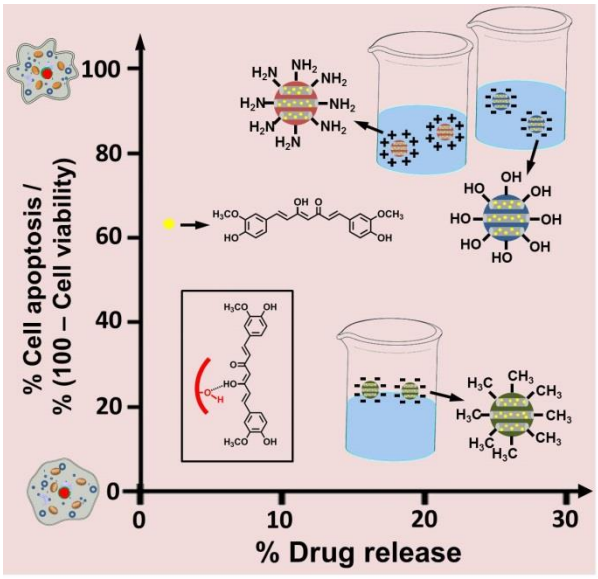

Scheme 1. Schematic representation comparing the in vitro drug release of curcumin from MCM-41-CUR, MCM-41-NH_2-CUR and MCM-41-CH_3-CUR samples and its cell cytotoxicity performance in SCC25 cell line. Inset represents the binding of curcumin to the interior pore wall of MCM-41, MCM-41-NH_2 and MCM-41-CH_3 samples. Free drug is represented in yellow color. Inset shows the binding of CUR in MCM-41.

Table 1. Physicochemical properties of unfunctionalized and functionalized MCM-41 materials with and without curcumin loading

Sample	***a*** **(nm)**	***P*** **(nm)**	S_{BET} **(m^2/g)**	V_p **(cm^3/g)**	***Z.P.*** **(mV)**
MCM-41	4.19	2.17	995	0.79	-36.4 ± 1.42
MCM-41-NH_2	4.92	2.10	932	0.74	36.3 ± 2.52
MCM-41-CH_3	4.61	1.80	835	0.61	-18.2 ± 1.40
MCM-41-CUR	4.30	2.10	450	0.44	-35.27 ± 0.40
MCM-41-NH_2-CUR	4.90	1.91	407	0.39	23.6 ± 0.92
MCM-41-CH_3-CUR	4.61	1.73	343	0.33	-24.3 ± 1.00

Note: *a*=cell dimension; S_{BET} = BET surface area; V_p = pore volume; *P* = pore size; Z.P. = Zeta potential.

AUTHOR INFORMATION

Corresponding Author

*s.karmakar@uq.edu.au, Tel: +61 7 3346 3815, Fax: +61 7 3346 3973.

Present Addresses

†If an author's address is different than the one given in the affiliation line, this information may be included here.

Funding Sources

The authors declare no competing financial interest.

ACKNOWLEDGMENT

We thank the Australian Research Council and Cancer Council of Queensland for financial support. We acknowledge the Australian National Fabrication Facility and the Australian Microscopy and Microanalysis Research Facility at the Centre for Microscopy and Microanalysis, the University of Queensland.

REFERENCES

(1) Halpin HA, M.-S.-V. M., Martin-Moreno JM Chronic Disease Prevention and the New Public Health. *Public Health Rev.* **2010**, *32*, 120-154.

(2) Gottesman, M. M.; Ludwig, J.; Xia, D.; Szakacs, G. Defeating drug resistance in cancer. *Discovery medicine* **2006**, *6*, 18-23.

(3) Anand, P.; Sundaram, C.; Jhurani, S.; Kunnumakkara, A. B.; Aggarwal, B. B. Curcumin and cancer: An "old-age" disease with an "age-old" solution. *Cancer Lett.* **2008**, *267*, 133-164.

(4) Shishodia, S.; Sethi, G.; Aggarwal, B. B. Curcumin: Getting Back to the Roots. *Ann NY Acad Sci* **2005**, *1056*, 206-217.

(5) Goel, A.; Aggarwal, B. B. Curcumin, the Golden Spice From Indian Saffron, Is a Chemosensitizer and Radiosensitizer for Tumors and Chemoprotector and Radioprotector for Normal Organs. *Nutr. Cancer* **2010**, *62*, 919-930.

(6) Anand, P.; Kunnumakkara, A. B.; Newman, R. A.; Aggarwal, B. B. Bioavailability of curcumin: Problems and promises. *Mol. Pharm.* **2007**, *4*, 807-818.

(7) Bansal, S. S.; Goel, M.; Aqil, F.; Vadhanam, M. V.; Gupta, R. C. Advanced Drug Delivery Systems of Curcumin for Cancer Chemoprevention. *Cancer Prev. Res.* **2011**, *4*, 1158-1171.

(8) Couvreur, P.; Dubernet, C.; Puisieux, F. Controlled drug-delivery with nanoparticles - current possibilities and future-trends. *Eur. J Pharm. Biopharm.* **1995**, *41*, 2-13.

(9) Mulik, R. S.; Monkkonen, J.; Juvonen, R. O.; Mahadik, K. R.; Paradkar, A. R. Transferrin mediated solid lipid nanoparticles containing curcumin: Enhanced in vitro anticancer activity by induction of apoptosis. *Int. J Pharm.* **2010**, *398*, 190-203.

(10) Oussoren, C.; Storm, G. Liposomes to target the lymphatics by subcutaneous administration. *Adv. Drug Deliver Rev.* **2001**, *50*, 143-156.

(11) Tarn, D.; Ashley, C. E.; Xue, M.; Carnes, E. C.; Zink, J. I.; Brinker, C. J. Mesoporous Silica Nanoparticle Nanocarriers: Biofunctionality and Biocompatibility. *Accounts Chem. Res.* **2013**, *46*, 792-801.

(12) Vallet-Regi, M.; Ramila, A.; del Real, R. P.; Perez-Pariente, J. A new property of MCM-41: Drug delivery system. *Chem. Mater.* **2001**, *13*, 308-311.

(13) Szegedi, A.; Popova, M.; Goshev, I.; Mihaly, J. Effect of amine functionalization of spherical MCM-41 and SBA-15 on controlled drug release. *J Solid State Chem.* **2011**, *184*, 1201-1207.

(14) Clifford, N. W.; Iyer, K. S.; Raston, C. L. Encapsulation and controlled release of nutraceuticals using mesoporous silica capsules. *J Mater. Chem.* **2008**, *18*, 162-165.

(15) Choi, Y. L.; Jaworski, J.; Seo, M. L.; Lee, S. J.; Jung, J. H. Controlled release using mesoporous silica nanoparticles functionalized with 18-crown-6 derivative. *J Mater. Chem.* **2011**, *21*, 7882-7885.

(16) Jin, D.; Park, K. W.; Lee, J. H.; Song, K.; Kim, J. G.; Seo, M. L.; Jung, J. H. The selective immobilization of curcumin onto the internal surface of mesoporous hollow silica particles by covalent bonding and its controlled release. *J Mater. Chem.* **2011**, *21*, 3641-3645.

(17) Gangwar, R. K.; Dhumale, V. A.; Kumari, D.; Nakate, U. T.; Gosavi, S. W.; Sharma, R. B.; Kale, S. N.; Datar, S. Conjugation of curcumin with PVP capped gold nanoparticles for improving bioavailability. *Mater. Sci. Eng. C Mater. Biol. Appl.* **2012**, *32*, 2659-2663.

(18) He, Q. J.; Shi, J. L.; Chen, F.; Zhu, M.; Zhang, L. X. An anticancer drug delivery system based on surfactant-templated mesoporous silica nanoparticles. *Biomaterials* **2010**, *31*, 3335-3346.

(19) Niidome, T.; Yamagata, M.; Okamoto, Y.; Akiyama, Y.; Takahashi, H.; Kawano, T.; Katayama, Y.; Niidome, Y. PEG-modified gold nanorods with a stealth character for in vivo applications. *J Control Release* **2006**, *114*, 343-347.

(20) Tonnesen, H. H.; Karlsen, J. Studies on curcumin and curcuminoids .6. Kinetics of curcumin degradation in aqueous-solution. *Z Lebensm Unters For.* **1985**, *180*, 402-404.

(21) Wang, Y. J.; Pan, M. H.; Cheng, A. L.; Lin, L. I.; Ho, Y. S.; Hsieh, C. Y.; Lin, J. K. Stability of curcumin in buffer solutions and characterization of its degradation products. *J Pharmaceut. Biomed.* **1997**, *15*, 1867-1876.

(22) Jambhrunkar, S.; Karmakar, S.; Popat, A.; Yu, M.; Yu, C. Mesoporous silica nanoparticles enhance the cytotoxicity of curcumin. *Rsc Advances* **2014**, *4*, 709-712.

(23) Lu, J.; Li, Z. X.; Zink, J. I.; Tamanoi, F. In vivo tumor suppression efficacy of mesoporous silica nanoparticles-based drug-delivery system: enhanced efficacy by folate modification. *Nanomedicine: NBM* **2012**, *8*, 212-220.

(24) Szegedi, A.; Popova, M.; Goshev, I.; Klebert, S.; Mihaly, J. Controlled drug release on amine functionalized spherical MCM-41. *J Solid State Chem.* **2012**, *194*, 257-263.

(25) Tang, Q. L.; Xu, Y.; Wu, D.; Sun, Y. H.; Wang, J.; Xu, J.; Deng, F. Studies on a new carrier of trimethylsilyl-modified mesoporous material for controlled drug delivery. *J Control Release* **2006**, *114*, 41-46.

(26) Yang, S.; Zhao, L. Z.; Yu, C. Z.; Zhou, X. F.; Tang, J. W.; Yuan, P.; Chen, D. Y.; Zhao, D. Y. On the origin of helical mesostructures. *J Am. Chem. Soc.* **2006**, *128*, 10460-10466.

(27) Zhao, X. S.; Lu, G. Q. Modification of MCM-41 by surface silylation with trimethylchlorosilane and adsorption study. *J Phys. Chem. B* **1998**, *102*, 1556-1561.

(28) Kecht, J.; Schlossbauer, A.; Bein, T. Selective Functionalization of the Outer and Inner Surfaces in Mesoporous Silica Nanoparticles. *Chem. Mater.* **2008**, *20*, 7207-7214.

(29) Lu, J.; Liong, M.; Zink, J. I.; Tamanoi, F. Mesoporous silica nanoparticles as a delivery system for hydrophobic anticancer drugs. *Small* **2007**, *3*, 1341-1346.

(30) Chen, Y.; Wu, Q. Q.; Zhang, Z. H.; Yuan, L.; Liu, X.; Zhou, L. Preparation of Curcumin-Loaded Liposomes and Evaluation of Their Skin Permeation and Pharmacodynamics. *Molecules* **2012**, *17*, 5972-5987.

(31) Shao, J. F.; Zheng, D. H.; Jiang, Z. F.; Xu, H. E.; Hu, Y.; Li, X. L.; Lu, X. W. Curcumin delivery by methoxy polyethylene glycol-poly(caprolactone) nanoparticles inhibits the growth of C6 glioma cells. *Acta Bioch Bioph Sin* **2011**, *43*, 267-274.

(32) Yang, J.; Zhou, L.; Zhao, L.; Zhang, H.; Yin, J.; Wei, G.; Qian, K.; Wang, Y.; Yu, C. A designed nanoporous material for phosphate removal with high efficiency. *J Mater. Chem.* **2011**, *21*, 2489-2494.

(33) Yang, C. M.; Liu, P. H.; Ho, Y. F.; Chiu, C. Y.; Chao, K. J. Highly dispersed metal nanoparticles in functionalized SBA-15. *Chem. Mater.* **2003**, *15*, 275-280.

(34) Mohan, P. R. K.; Sreelakshmi, G.; Muraleedharan, C. V.; Joseph, R. Water soluble complexes of curcumin with cyclodextrins: Characterization by FT-Raman spectroscopy. *Vib. Spectrosc.* **2012**, *62*, 77-84.

(35) Limnell, T.; Santos, H. A.; Makila, E.; Heikkila, T.; Salonen, J.; Murzin, D. Y.; Kumar, N.; Laaksonen, T.; Peltonen, L.; Hirvonen, J. Drug Delivery Formulations of Ordered and Nonordered Mesoporous Silica: Comparison of Three Drug Loading Methods. *J. Pharm. Sci.* **2011**, *100*, 3294-3306.

(36) Khan, M. A.; Gahlot, S.; Majumdar, S. Oxidative Stress Induced by Curcumin Promotes the Death of Cutaneous T-cell Lymphoma (HuT-78) by Disrupting the Function of Several Molecular Targets. *Mol. Cancer Ther.* **2012**, *11*, 1873-1883.

(37) Mello, M. R.; Phanon, D.; Silveira, G. Q.; Llewellyn, P. L.; Ronconi, C. M. Amine-modified MCM-41 mesoporous silica for carbon dioxide capture. *Microporous Mesoporous Mat.* **2011**, *143*, 174-179.

(38) Park, D. H.; Nishiyama, N.; Egashira, Y.; Ueyama, K. Enhancement of hydrothermal stability and hydrophobicity of a silica MCM-48 membrane by silylation. *Ind. Eng. Chem. Res.* **2001**, *40*, 6105-6110.

(39) Pan, D. H.; Zhao, L. Z.; Qian, K.; Tan, L.; Zhou, L.; Zhang, J.; Huang, X. D.; Fan, Y.; Liu, H. Y.; Yu, C. Z.; Bao, X. J. A silanol protection mechanism: Understanding the decomposition behavior of surfactants in mesostructured solids. *J. Mater. Res.* **2011**, *26*, 804-814.

(40) Jambhrunkar, S.; Yu, M. H.; Yang, J.; Zhang, J.; Shrotri, A.; Endo-Munoz, L.; Moreau, J.; Lu, G. Q.; Yu, C. Z. Stepwise Pore Size Reduction of Ordered Nanoporous Silica Materials at Angstrom Precision. *J. Am. Chem. Soc.* **2013**, *135*, 8444-8447.

(41) Nieto, A.; Balas, F.; Colilla, M.; Manzano, M.; Vallet-Regi, M. Functionalization degree of SBA-15 as key factor to modulate sodium alendronate dosage. *Micropor. Mesopor. Mat.* **2008**, *116*, 4-13.

(42) Punyacharoennon, P.; Charuchinda, S.; Srikulkit, K. Grafting and Phosphonic Acid Functionalization of Hyperbranched Polyamidoamine Polymer onto Ultrafine Silica. *J. Appl. Polym. Sci.* **2008**, *110*, 3336-3347.

(43) Yang, J.; Chen, J. R.; Song, J. H. Studies of the surface wettability and hydrothermal stability of methyl-modified silica films by FT-IR and Raman spectra. *Vib. Spectrosc.* **2009**, *50*, 178-184.

(44) Kolev, T. M.; Velcheva, E. A.; Stamboliyska, B. A.; Spiteller, M. DFT and experimental studies of the structure and vibrational spectra of curcumin. *Int. J Quantum Che.* **2005**, *102*, 1069-1079.

(45) Ambrogi, V.; Famiani, F.; Perioli, L.; Marmottini, F.; Di Cunzolo, I.; Rossi, C. Effect of MCM-41 on the dissolution rate of the poorly soluble plant growth regulator, the indole-3-butyric acid. *Micropor Mesopor Mat.* **2006**, *96*, 177-183.

(46) Vialpando, M.; Aerts, A.; Persoons, J.; Martens, J.; Van den Mooter, G. Evaluation of Ordered Mesoporous Silica as a Carrier for Poorly Soluble Drugs: Influence of Pressure on the Structure and Drug Release. *J. Pharm. Sci.* **2011**, *100*, 3411-3420.

(47) Jal, P. K.; Patel, S.; Mishra, B. Chemical modification of silica surface by immobilization of functional groups for extractive concentration of metal ions. *Talanta* **2004**, *62*, 1005-1028.

(48) Xu, Y.; Wang, C.; Zhou, G.; Wu, Y.; Chen, J. Improving the controlled release of water-insoluble emodin from amino-functionalized mesoporous silica. *Appl. Surf. Sci.* **2012**, *258*, 6366-6372.

(49) Ranjan, A. P.; Mukerjee, A.; Helson, L.; Vishwanatha, J. K. Scale up, optimization and stability analysis of Curcumin C3 complex-loaded nanoparticles for cancer therapy. *J Nanobiotechnology* **2012**, *10*.

(50) Frohlich, E. The role of surface charge in cellular uptake and cytotoxicity of medical nanoparticles. *Int. J. Nanomed.* **2012**, *7*, 5577-5591.

(51) Naha, P. C.; Davoren, M.; Lyng, F. M.; Byrne, H. J. Reactive oxygen species (ROS) induced cytokine production and cytotoxicity of PAMAM dendrimers in J774A.1 cells. *Toxicol. Appl. Pharmacol.* **2010**, *246*, 91-99.

(52) McNerny, D. Q.; Leroueil, P. R.; Baker, J. R. Understanding specific and nonspecific toxicities: a requirement for the development of dendrimer-based pharmaceuticals. *Wiley Interdiscip. Rev.-Nanomed. Nanobiotechnol.* **2010**, *2*, 249-259.

(53) Chen, L. A.; McCrate, J. M.; Lee, J. C. M.; Li, H. The role of surface charge on the uptake and biocompatibility of hydroxyapatite nanoparticles with osteoblast cells. *Nanotechnology* **2011**, *22*, 10.

(54) Yue, Z.-G.; Wei, W.; Lv, P.-P.; Yue, H.; Wang, L.-Y.; Su, Z.-G.; Ma, G.-H. Surface Charge Affects Cellular Uptake and Intracellular Trafficking of Chitosan-Based Nanoparticles. **2011**, *12*, 2440-2446.

(55) Liu, E.; Wu, J.; Cao, W.; Zhang, J.; Liu, W.; Jiang, X.; Zhang, X. Curcumin induces G2/M cell cycle arrest in a p53-dependent manner and upregulates ING4 expression in human glioma. *J Neuro-Oncol.* **2007**, *85*, 263-270.

(56) Lee, D. S.; Lee, M. K.; Kim, J. H. Curcumin Induces Cell Cycle Arrest and Apoptosis in Human Osteosarcoma (HOS) Cells. *Anticancer Res.* **2009**, *29*, 5039-5044.

(57) Chen, Q.; Wang, Y.; Xu, K.; Lu, G.; Ying, Z.; Wu, L.; Zhan, J.; Fang, R.; Wu, Y.; Zhou, J. Curcumin induces apoptosis in human lung adenocarcinoma A549 cells through a reactive oxygen species-dependent mitochondrial signaling pathway. *Oncology Rep.* **2010**, *23*, 397-403.

(58) Sanchez, Y.; Simon, G. P.; Calvino, E.; de Blas, E.; Aller, P. Curcumin Stimulates Reactive Oxygen Species Production and Potentiates Apoptosis Induction by the Antitumor Drugs Arsenic Trioxide and Lonidamine in Human Myeloid Leukemia Cell Lines. *J Pharmacol. Exp. Ther.* **2010**, *335*, 114-123.

(59) Su, C.-C.; Lin, J.-G.; Li, T.-M.; Chung, J.-G.; Yang, J.-S.; Ip, S.-W.; Lin, W.-C.; Chen, G.-W. Curcumin-induced apoptosis of human colon cancer colo 205 cells through the production of ROS, Ca2+ and the activation of caspase-3. *Anticancer Res.* **2006**, *26*, 4379-4389.

Chapter 7

Modulating in vitro Release and Solubility of Griseofulvin Using Functionalised Mesoporous Silica Nanoparticles

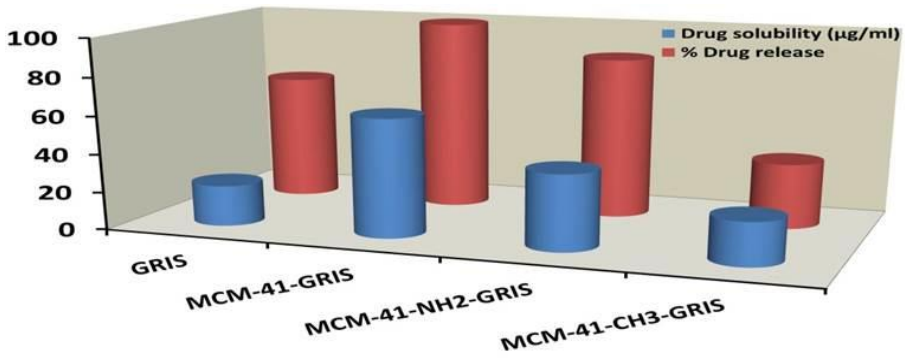

Mesoporous silica nanoparticles (MCM-41) were used as a carrier system to study the influence of surface charge and hydrophobicity on solubility and *in-vitro* drug release behavior of Griseofulvin, a potent antifungal drug with low water solubility. Surface charge modification showed enhancement in both solubility and drug release of griseofulvin compared to the hydrophobic modification due to the poor wetting effect by the hydrophobic groups grafted on MCM-41 nanoparticles. Thus, the surface functionalization on MCM-41 is found to have significant effect on griseofulvin's *in vitro* release and solubility

Chapter 7 is included as it appears in Journal of Colloid and Interface Science, 2014,434, 218-225.

Contents lists available at ScienceDirect

Journal of Colloid and Interface Science

www.elsevier.com/locate/jcis

Modulating *in vitro* release and solubility of griseofulvin using functionalized mesoporous silica nanoparticles

Siddharth Jambhrunkar [a], Zhi Qu [a], Amirali Popat [b,c], Surajit Karmakar [a], Chun Xu [a], Chengzhong Yu [a,*]

[a] *Australian Institute for Bioengineering and Nanotechnology, The University of Queensland, Brisbane, QLD 4072, Australia*
[b] *The School of Pharmacy, The University of Queensland, Brisbane, QLD 4072, Australia*
[c] *Mucosal Diseases Group, Mater Research Institute – The University of Queensland, Translational Research Institute, 37 Kent St, Woolloongabba, QLD 4102, Australia*

ARTICLE INFO

Article history:
Received 25 May 2014
Accepted 9 August 2014
Available online 20 August 2014

Keywords:
Mesoporous silica
Surface charge
Hydrophobicity
Griseofulvin
Drug release
Solubility

ABSTRACT

Mesoporous silica nanoparticles (MCM-41) were used as a carrier system to study the influence of surface charge and hydrophobicity on solubility and *in-vitro* drug release behavior of Griseofulvin, a potent antifungal drug with low water solubility. Bare MCM-41 with a pure silica composition, MCM-41 after amino functionalization (MCM-41-NH_2) and methyl functionalization (MCM-41-CH_3) were used in this study followed by encapsulation of griseofulvin. Various characterization techniques have been employed to confirm the successful drug loading inside the nanopores. The surface functionalization on MCM-41 is found to have significant effect on griseofulvin's *in vitro* release and solubility. Both negatively and positively charged surface showed enhancement in solubility and drug release of griseofulvin. However, the hydrophobic modification led to a retarded drug release, which is caused by the poor wetting effect in the case of MCM-41-CH_3 nanoparticles.

1. Introduction

Relatively higher proportions of newly emerging drug molecules from high throughput screening are hydrophobic (poor aqueous solubility), posing a major obstacle in clinical applications [1,2]. Solubility enhancement is traditionally achieved by various processes such as salt formation, co-solvents, complexation, and solid dispersion to name a few. These techniques, however, suffer from uncontrolled precipitation, solvent toxicity and stability concerns [3–6]. The main emphasis for solubility enhancement till date in the pharmaceutical fraternity relies on particle size reduction, as reflected by Ostwald–Freundlich equation [7]. Particle size reduction techniques such as comminution, micronization and spray drying are conceived to be efficient, reproducible and economically viable. However, this process leads to induction of physical stress on drug particles, tendency to agglomerate on standing and is inapt for thermolabile drugs. The development of effective carrier systems provides another pathway to enhance the drug solubility as well as to control the release profile. Several delivery systems such as surfactant complexes, liposomes, hydrogels, and polymeric nanoparticles have been developed but suffer from synthesis complexity and poor biological stability [8–10].

Mesoporous silica nanoparticles (MSNs) such as MCM-41 [11] and SBA-15 [12], with unique features of ordered structure, high surface area, large pore volume, tunable pore size, ease of surface functionalization [13] and biocompatibility have attracted increased attention in drug delivery field since the last decade [14]. The influence of pore size of MSNs has been studied for drug, peptide, protein and enzyme immobilization [15–18]. MSNs provide an adjustable pore size at nanoscale for the confinement of drug molecules and hence the size of drug particles can be reduced at nanoscale leading to solubility enhancement [19–21]. MSNs surface functionalisation also plays an important role in drug encapsulation and release [22,23]. Surface functionalized MSNs with 3-aminopropyl triethoxysilane help in achieving high drug loading and slower drug release [13,22,24]. MSNs modified by 2-cyanopropyltriethoxysilane and mercaptopropyltrimethoxysilane improved drug efficacy by achieving high cell specificity when tested in cell lines [25,26]. MSNs were modified to obtain hydrophobic surface using 1, 1, 1, 3, 3, 3-hexamethyldisilazane, and ibuprofen release test showed that the drug release was inversely proportional to the degree of hydrophobicity [27]. Despite numerous studies highlighting the significance and advantage of MSNs for enhancing drug solubility and the effect of surface functionalization of MSNs on drug release, there is no study to compare the influence of surface charge and hydrophobicity on both drug solubility and drug release.

* Corresponding author. Fax: +61 7 3346 3973.
E-mail address: c.yu@uq.edu.au (C. Yu).

http://dx.doi.org/10.1016/j.jcis.2014.08.019
0021-9797/

Griseofulvin (GRIS), a potent antifungal drug, belongs to BCS class II and is slightly soluble in water [28]. Several studies have been reported addressing the solubility and/or dissolution enhancement of griseofulvin using processes such as solid dispersions [19,29], complexation with cyclodextrin [30], microemulsions [31] and deformable membrane vesicles [28]. In a recent study, an inclusion complex of griseofulvin – β-cyclodextrin was formed and grafted on the silica surface to study the adsorption kinetics, confirming the successful encapsulation of griseofulvin in β-cyclodextrin [32]. However, the drug release or solubility behavior was not reported. To date the encapsulation of GRIS inside MSNs has not been reported.

In this study, we report the influence of surface charge and hydrophobicity of MSNs on solubility and drug release behavior of griseofulvin in a series of MCM-41 materials (Fig. 1), including bare MCM-41, amino functionalized MCM-41 (MCM-41-NH_2) and methyl functionalized MCM-41 (MCM-41-CH_3). The surface modified MSNs were synthesized to obtain similar pore size to avoid the influence of pore size in further evaluations. Griseofulvin was encapsulated in the pore channels of MSNs by a simple rotavap technique. We studied the influence of surface chemistry on drug solubility and drug release by comparing negatively and positively charged MCM-41 with hydrophobic MCM-41-CH_3. To the best of our knowledge this is the first report to study the influence of surface modification of MSNs on griseofulvin's *in vitro* release and solubility.

2. Experimental

2.1. Materials

Cetyl trimethylammonium bromide (CTAB), tetraethoxy orthosilicate (TEOS), (3-aminopropyl)triethoxysilane (APTES), chlorotrimethylsilane (TMCS), sodium lauryl sulfate (SLS) and griseofulvin (GRIS) were purchased from Sigma–Aldrich. Reagent grade sodium hydroxide (NaOH) was received from ChemSupply. Methanol AR and Toluene were purchased from RCI labscan and Merck, respectively.

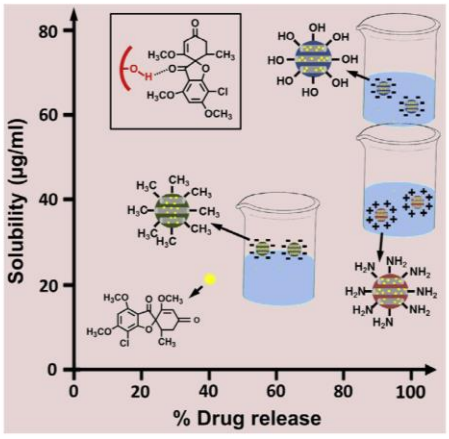

Fig. 1. A schematic representation comparing the solubility and *in vitro* drug release of griseofulvin from MCM-41-GRIS, MCM-41-NH_2-GRIS and MCM-41-CH_3-GRIS samples. Inset represents the binding of griseofulvin to the interior pore wall of MCM-41, MCM-41-NH_2 and MCM-41-CH_3 samples. Free drug is represented in yellow color. Inset shows the binding of GRIS in MCM-41. (For interpretation of the references to color in this figure legend, the reader is referred to the web version of this article.)

2.2. Characterization

X-ray diffractograms (XRD) and wide angle XRD (WXRD) were recorded on a Rigaku Miniflex X-ray diffractometer with Fe-filtered Co radiation (λ = 1.79 Å). Transmission Electron Microscopy (TEM) images were obtained with a JEOL 1010 microscope operated at 100 kV. Scanning electron microscopy (SEM) characterization was performed using Hitachi SU3500 operated at 5 kV and working distance of 5.5 cm. Nitrogen physisorption measurements were carried out at −196 °C by using a Micromeritics Tristar II 3020 system. MCM-41, MCM-41-NH_2 and MCM-41-CH_3 samples were degassed at 100 °C whereas griseofulvin encapsulated MCM-41 (MCM-41-GRIS), MCM-41-NH_2 (MCM-41-NH_2-GRIS) and MCM-41-CH_3 (MCM-41-CH_3-GRIS) samples were degassed at 50 °C overnight on a vacuum line. The pore-size distribution was measured from the adsorption branch of the isotherm using BJH model. Fourier transform infrared (FTIR) spectra were recorded on ThermoNicolet Nexus 6700 FTIR spectrometer equipped with Diamond ATR (attenuated total reflection) Crystal. For each spectrum, 128 scans and 4 cm^{-1} resolution was applied over the range of 400–4000 cm^{-1}. Particle size and zeta potential were measured on a Malvern Zetasizer Nano-ZS. The thermogravimetric analysis (TGA) was performed by a Setaram TG92 instrument with a heating rate of 5 °C/min in air flow. Griseofulvin concentration was determined using UV–VIS spectrophotometer (Shimadzu UV-2450).

2.3. Synthesis of MCM-41

MCM-41 synthesis was performed with slight modification to a previously reported method by Yang et al. [33]. Briefly, 1.0 g of CTAB was dissolved in 480 g of deionized water under stirring at room temperature followed by addition of 3.5 mL of NaOH (2 M) and increasing the temperature to 80 °C. Then, 6.7 mL of TEOS was added into the mixture as a silica source at 80 °C under continuous stirring for an additional 2 h. The resultant product was collected by filtration and dried at room temperature. The as-synthesized MCM-41 was divided into three parts. One-third of the material was subjected to solvent extraction process for the removal of surfactant template and labeled as MCM-41. Another one-third of the material was solvent extracted and used for the preparation of methyl modified MCM-41. The remaining as-synthesized material was utilized for the synthesis of amino modified MCM-41.

Surfactant template was removed by a reported method by Lu et. al. [34] with some modification. 0.3 g of as-synthesized material was added to 32 mL of methanol under stirring and the temperature was increased to 60 °C. To this suspension, 2.0 mL of conc. HCl was added and kept under continuous stirring for 36 h. Later the suspension was centrifuged and washed with methanol twice to ensure complete surfactant removal. The final product was dried at 50 °C overnight to be used for further studies.

2.4. Synthesis of amino modified MCM-41-NH_2

Amino modification was performed according to a published report with slight changes [35]. Typically, 0.4 g of as-synthesized MCM-41 was added to 25 mL of methanol under stirring at RT followed by the addition of 1.5 mL of APTES. The suspension was stirred overnight at RT. The amino functionalized MCM-41 with surfactant template still present in it was then retrieved by centrifugation and washed with methanol twice. The material was then dried at 50 °C overnight before subjected to solvent extraction process for surfactant template removal as described earlier.

2.5. Synthesis of methyl modified MCM-41

Methyl modification was performed according to a published report [36]. Generally, 0.4 g of MCM-41 after solvent extraction was added to 20 mL of TMCS solution in toluene with a concentration of 5 wt% under stirring at 70 °C. The suspension was stirred for additional 24 h at 70 °C. The methyl functionalized MCM-41 was then centrifuged and washed with toluene and ethanol. The material was then dried at 50 °C overnight for further studies.

2.6. Griseofulvin loading and in vitro release measurements

Griseofulvin loading was performed using rotary evaporation technique. 160 mg of MCM-41 was placed in a rotary evaporation flask and 40 mg of griseofulvin was added to it followed by the addition of 10 mL of dichloromethane to achieve 20% w/w drug loading theoretically. This mixture was sonicated for 2 min and the solvent was slowly evaporated using rotary evaporator at 50 °C with circulating water temperature maintained at 5 °C to obtain griseofulvin loaded MCM-41. Evaporation process was continued till all the solvent is removed and dried powder could be observed in the flask. Dried griseofulvin loaded MCM-41 sample (MCM-41-GRIS) was collected from the flask and used for further studies. Similar procedure was followed for MCM-41-NH_2 and MCM-41-CH_3 materials. Dried griseofulvin loaded MCM-41-NH_2 and MCM-41-CH_3 materials are denoted as MCM-41-NH_2-GRIS and MCM-41-CH_3-GRIS, respectively.

2.7. In vitro release and solubility studies

The *in vitro* release of griseofulvin from MCM-41-GRIS, MCM-41-NH_2-GRIS and MCM-41-CH_3-GRIS was evaluated using dialysis bag technique [18,37,38]. MCM-41-GRIS, MCM-41-NH_2-GRIS and MCM-41-CH_3-GRIS equivalent to 1 mg of griseofulvin was weighed and suspended in 1 mL of 0.5% SLS. This suspension was then placed in dialysis bag with 10 kDa molecular weight cutoff and was immersed into 9 mL of 0.5% SLS at 37 °C with continuous stirring. At pre-determined time intervals, 1 mL of the samples was withdrawn and immediately replaced with an equal volume of dissolution medium to maintain the sink condition. The samples withdrawn at pre-determined time intervals were then properly diluted and analyzed for griseofulvin content using UV–VIS spectrophotometer at 296 nm.

Griseofulvin solubility studies were conducted by adding an excessive quantity of griseofulvin and MCM-41-GRIS, MCM-41-NH_2-GRIS and MCM-41-CH_3-GRIS material to 2 mL of water. The mixture was kept for shaking for 48 h at 37 °C. The suspension was then centrifuged and the supernatant was analyzed for griseofulvin content using a UV–VIS spectrophotometer at 296 nm.

3. Results and discussion

3.1. Material characterization

The XRD patterns of MCM-41 material (Fig. 2A) show three well resolved diffraction peaks at 2θ of 2.44, 4.27 and 4.93° with a reciprocal d-spacing ratio close to $1:\sqrt{3}:2$, which can be indexed as 100, 110 and 200 reflections of an ordered two dimensional (2D) hexagonal mesostructure with a pore symmetry of *p6mm*. The positions of three diffraction peaks for MCM-41-NH_2 and MCM-41-CH_3 are similar to that of MCM-41 demonstrating retention of ordered structure after surface functionalization. After encapsulation of griseofulvin in MCM-41, MCM-41-NH_2 and MCM-41-CH_3, no shift was observed for the three diffraction peaks, indicating the drug loading process does not alter the ordered mesostructure.

To study the nature of griseofulvin encapsulated in MCM-41 materials, WXRD study was performed. The WXRD patterns (Fig. 2B) were obtained for MCM-41 materials with and without griseofulvin loading along with the physical mixtures of griseofulvin and respective MCM-41 materials. Pure griseofulvin is a crystalline compound showing sharp diffractions in the 2θ range of 10–40°. The amorphous nature of MCM-41, MCM-41-NH_2 and MCM-41-CH_3 material is evidenced from the broad peak in the 2θ range of 20–30° [39,40]. The physical mixture of three MCM-41 materials and griseofulvin (MCM-41-GRIS PM, MCM-41-NH_2-GRIS PM and MCM-41-CH_3-GRIS PM) show diffraction peaks corresponding to pure griseofulvin. However, for MCM-41-GRIS, MCM-41-NH_2-GRIS and MCM-41-CH_3-GRIS using the rotavap technique to encapsulate griseofulvin, no obvious diffraction peaks originating from GRIS can be observed, suggesting that GRIS is entrapped inside the nanopores with an amorphous nature [39,40].

Typical TEM images of MCM-41, MCM-41-NH_2 and MCM-41-CH_3 are shown in Fig. 3. Because three materials were prepared from the same mother solution, they show similar morphologies as nanoparticles with 100–200 nm in sizes. For each particle shown in Fig. 3a–c, parallel channel-like or hexagonally arrayed porous structures can be seen, in accordance with a hexagonal mesostructure. The TEM results also suggest that surface functionalization of MCM-41 in our experiments did not affect the hexagonal structure, consistent with the XRD characterizations. Dynamic light scattering (DLS) measurements (Fig. 3d) reveal a mean size of 190 nm for all the MSN materials – MCM-41 (PDI = 0.182), MCM-41-NH_2 (PDI = 0.165) and MCM-41-CH_3 (PDI = 0.223), similar to the TEM results.

The nitrogen adsorption/desorption isotherms of MCM-41, MCM-41-NH_2 and MCM-41-CH_3 exhibit a typical type IV isotherm with a steep capillary condensation step at a relative pressure (P/P_0) range of 0.2–0.4 (Fig. 4A), characteristic of MCM-41 type mesoporous materials. From the pore size distribution curves (Fig. 4B), it is shown that MCM-41 material has a pore size of 2.57 nm. MCM-41-NH_2 has a pore size of 1.99 nm, suggesting that a small amount of the silica source (APTES) can replace the surfactants during the post-modification process starting from the as-synthesized MCM-41 [35]. If the post-modification of amino groups starts from MCM-41 after removing the surfactants, the pores will be blocked (data not shown) [41]. MCM-41-CH_3 exhibits a pore size centered at 2.13 nm, suggesting slight decrease in the pore size due to the presence of small amount of methyl groups in pore channels during the modification process. Our observation is consistent with previous reports on the hydrophobic modification of mesoporous materials after removing the surfactants, where the pore size is reduced by 0.25–0.65 nm [36,42].

After griseofulvin encapsulation in MCM-41, MCM-41-NH_2 and MCM-41-CH_3 materials, the pore size of MCM-41-GRIS, MCM-41-NH_2-GRIS and MCM-41-CH_3-GRIS have been decreased to 1.87, 1.68, and 2.02 nm, respectively. The drug encapsulation also results in decrease in surface area and pore volume. For example, the surface area and surface volume for MCM-41-GRIS decreases to 562 m^2/g and 0.45 cm^3/g compared to MCM-41 from 900 m^2/g and 0.86 cm^3/g respectively. Similar trend was observed for MCM-41-NH_2-GRIS and MCM-41-CH_3-GRIS materials as well. All the textural parameters for MSNs are summarized in Table 1 for comparison.

The surface modification of MCM-41 materials was further analyzed by measuring zeta potential (Z.P.). As shown from Table 1, MCM-41 shows a Z.P. of -33.5 ± 0.42 mV, while MCM-41-NH_2 and MCM-41-CH_3 display Z.P. of 33.2 ± 0.20 and -12.7 ± 0.60 mV, respectively, confirming the successful surface modification of MCM-41 materials. The surface modification is also evidenced by dispersing the materials in ether – water composition as shown in Fig. 4C. Both MCM-41 and MCM-41-NH_2 materials were totally

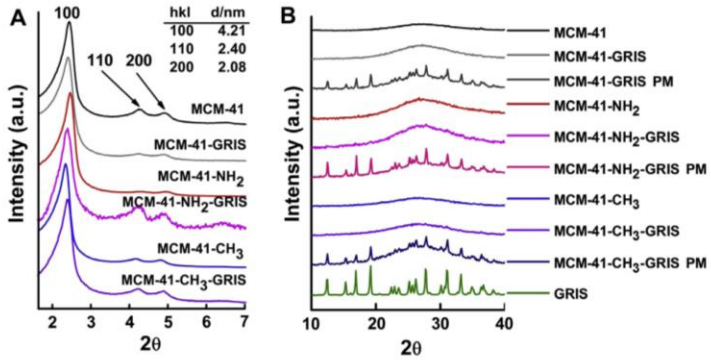

Fig. 2. (A) XRD patterns of MCM-41 materials with and without griseofulvin loading. (B) WXRD patterns of MCM-41 materials with and without griseofulvin loading and physical mixtures of griseofulvin with unfunctionalized and functionalized MCM-41 materials.

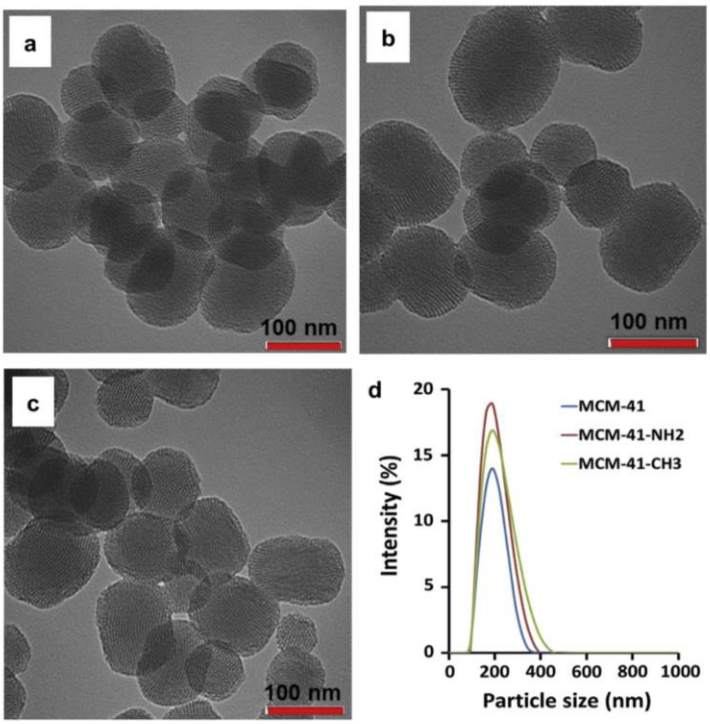

Fig. 3. Transmission Electron Microscopy (TEM) image of MCM-41 (a), MCM-41-NH_2 (b) and MCM-41-CH_3 (c) materials. DLS size measurements of MCM-41, MCM-41-NH_2 and MCM-41-CH_3 materials (d).

dispersed in aqueous phase with a hazy appearance, showing a hydrophilic nature. On the other hand, MCM-41-CH_3 material was completely dispersed in organic phase displaying its hydrophobic nature.

3.2. Adsorption of griseofulvin

The modification of MCM-41 materials with amino and methyl groups as well as the encapsulation of griseofulvin in MCM-41 materials was confirmed by FTIR analysis as shown in Fig. 5. Bare MCM-41 material exhibits two peaks at 803 and 1060 cm^{-1} (Fig. 5C), which can be indexed to symmetric and asymmetric Si–O–Si stretching (ν_s(Si–O–Si) and ν_a(Si–O–Si)), respectively. Two bands with low intensity are observed at 3740 cm^{-1} and 1630 cm^{-1} which can be indexed to the isolated silanol (ν(O–H)) and bending mode of physisorbed water respectively (Fig. 5A and B) [21,43]. The silanol peak disappeared when amino and methyl modifications are performed on MCM-41. The amino modification resulted in appearance of peaks at 2929, 1626 and 1518 cm^{-1} which can be attributed to C–H stretching, N–H bending and N–H stretching vibrations of aminopropyl group anchored on the surface of MCM-41 [13,44,45]. The methyl modification results in the peak at 2962 cm^{-1} which can be attributed to C–H vibration and band of peaks at 1255, 848 and 758 cm^{-1} attributed to

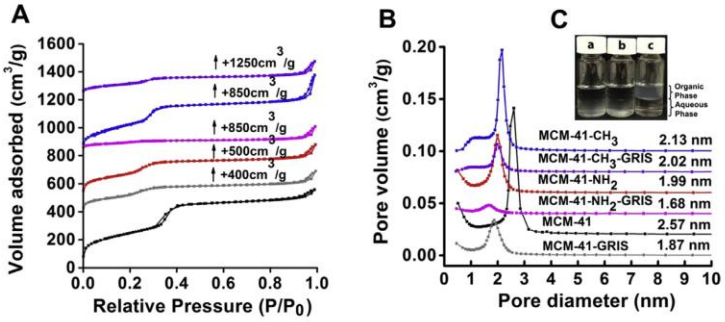

Fig. 4. (A) N_2 adsorption/desorption isotherms and (B) BJH pore-size distribution plot for unfunctionalized and functionalized MCM-41 materials with and without griseofulvin loading. (C) Digital image of (a) MCM-41, (b) MCM-41-NH_2 and (c) MCM-41-CH_3 demonstrating the hydrophobicity of materials by dispersing them in organic (ether)–aqueous (water) composition.

Table 1
Physicochemical properties of unfunctionalized and functionalized MCM-41 materials with and without griseofulvin loading.

Sample	*a* (nm)	*P* (nm)	S_{BET} (m^2/g)	V_p (cm^3/g)	Z.P. (mV)
MCM-41	4.86	2.57	900	0.86	−33.5 ± 0.42
MCM-41-NH_2	4.82	1.99	785	0.68	33.2 ± 0.20
MCM-41-CH_3	5.07	2.13	904	0.81	−12.7 ± 0.60
MCM-41-GRIS	4.94	1.87	562	0.45	−34.2 ± 0.34
MCM-41-NH_2-GRIS	4.95	1.68	179	0.24	34.5 ± 0.62
MCM-41-CH_3-GRIS	4.95	2.02	328	0.35	−12.4 ± 1.30

Note: *a* = cell dimension; S_{BET} = BET surface area; V_p = pore volume; *P* = pore size; Z.P. = Zeta potential.

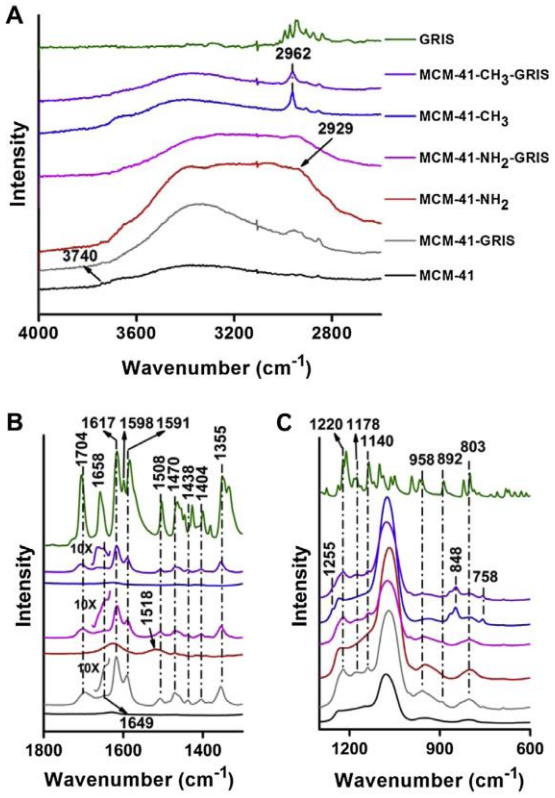

Fig. 5. FTIR spectra of unfunctionalized and functionalized MCM-41 materials with and without griseofulvin loading.

Si-CH_3 of methyl group from TMCS [42,46]. Pure griseofulvin displays two distinct peaks at 1704 and 1658 cm^{-1} which is attributed to the stretching of carbonyl group of benzofuran and cyclohexenone respectively present in its structure [19,29]. The peak at 1704 cm^{-1} appears as broadened peak in MCM-41-GRIS. Similarly the peak at 1658 cm^{-1} peak was broadened and shifted to 1649 cm^{-1} in MCM-41-GRIS. The broadening of these two peaks can be attributed to the hydrogen bonding between isolated silanols located in the interior surface of MCM-41 and carbonyl group of benzofuran and cyclohexenone of griseofulvin [19,29]. Moreover, peaks in the range of 1617–890 cm^{-1} in griseofulvin can also be seen in MCM-41-GRIS indicating the encapsulation of griseofulvin. Similar results were observed for MCM-41-NH_2-GRIS and MCM-41-CH_3-GRIS samples confirming the successful adsorption of griseofulvin.

TGA analysis was used to evaluate the griseofulvin loading amount in different samples under study (Fig. 6A). Griseofulvin encapsulated in MCM-41, MCM-41-NH_2 and MCM-41-CH_3 materials by rotary evaporation technique was found to be 19.92%, 15.76% and 19.90% respectively, indicating a high loading efficiency (80–95%) of the process, in accordance with previous reports [21,47]. For comparison, physical mixtures of griseofulvin and MCM-41 (MCM-41-GRIS PM), MCM-41-NH_2 (MCM-41-NH_2-GRIS PM) and MCM-41-CH_3 (MCM-41-CH_3-GRIS PM) materials were prepared. MCM-41-GRIS PM, MCM-41-NH_2-GRIS PM and MCM-41-CH_3-GRIS PM samples showed weight loss of 19.89%, 20.16% and 21.05% respectively (Fig. 7A). The hydrophobic modification inhibits the aqueous wetting of MCM-41-CH_3 by methyl groups present on the material which is evident by the wt.% loss at 100 °C as seen from Figs. 6A and 7A. The moisture loss for MCM-41 and MCM-41-NH_2 is 7 and 11% whereas 3% for MCM-41-CH_3 material thus demonstrating the effect of hydrophobicity on moisture uptake.

Differential scanning calorimetry (DSC) analysis was performed to further confirm the crystallinity of griseofulvin in MCM-41-GRIS, MCM-41-NH_2-GRIS and MCM-41-CH_3-GRIS

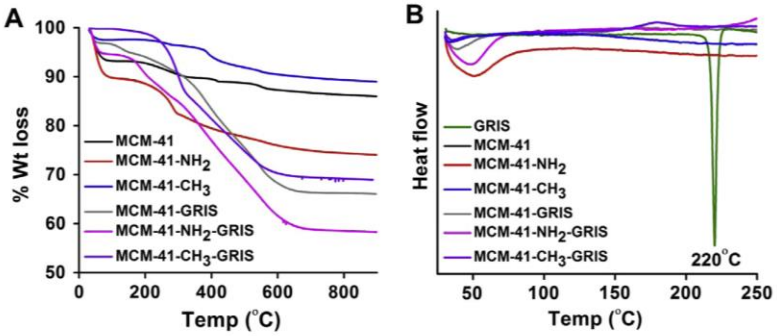

Fig. 6. (A) TGA curves and (B) DSC curves of unfunctionalized and functionalized MCM-41 materials with and without griseofulvin loading.

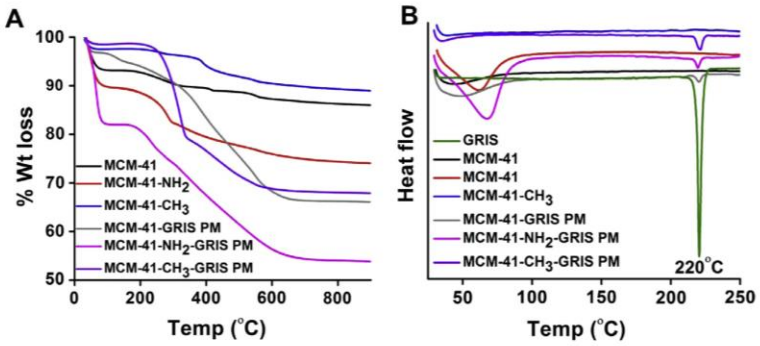

Fig. 7. TGA (A) and DSC (B) curves of physical mixtures of griseofulvin with unfunctionalized and functionalized MCM-41 materials.

materials (Fig. 6B). Pure griseofulvin clearly displays a sharp melting point peak at 220 °C. A weak signal can be observed for MCM-41-GRIS PM, MCM-41-NH_2-GRIS PM and MCM-41-CH_3-GRIS PM samples indicating the existence of griseofulvin's crystalline state in their respective physical mixtures (Fig. 7B). However, this peak cannot be seen in MCM-41-GRIS, MCM-41-NH_2-GRIS and MCM-41-CH_3-GRIS samples (Fig. 6B), indicating griseofulvin's non-crystalline state and its successful loading as nano-sized aggregates in the pore channels of these MCM-41 materials [20,48].

SEM images of GRIS, MCM-41, MCM-41-GRIS and MCM-41-GRIS PM samples were collected to provide further information on the drug loading (Fig. 8). GRIS shows a particulate morphology with irregular shapes and sizes (Fig. 8A). For MCM-41, spherical nanoparticles are observed with size of 100-200 nm (Fig. 8B), in accordance with TEM observations and previous reports [18]. In the case of MCM-41-GRIS, the morphology is similar to that of MCM-41 (Fig. 8C); no irregular shaped particles are observed. However, both spherical MCM-41 and irregular GRIS particles are observed in MCM-41-GRIS PM (Fig. 8D). The above studies, including WXRD, FTIR, DSC and SEM characterizations, support the conclusion that GRIS is successfully encapsulated in the nanopores of MCM-41.

3.3. In vitro release and solubility studies

To compare the effect of surface charge and hydrophobicity in griseofulvin encapsulated MCM-41 materials, griseofulvin release was studied in 0.5% SLS (under sink conditions) as the dissolution medium. After 1 h, the release of griseofulvin from MCM-41-GRIS, MCM-41-NH_2-GRIS and MCM-41-CH_3-GRIS was found to be 13.40%, 7.60% and 2.69% respectively compared to 7.37% from pure griseofulvin (Fig. 9). Until 8 h, the griseofulvin release from MCM-41-NH_2-GRIS (26.15%) was similar to that of pure griseofulvin (26.62%) while from that of MCM-41-GRIS and MCM-41-CH_3-GRIS was 45.19% and 8.85% respectively. Griseofulvin was completely released from MCM-41-GRIS after 48 h. After 8 h, griseofulvin's release from MCM-41-NH_2-GRIS was relatively faster compared to pure griseofulvin and took 96 h for its complete release. The slower release from MCM-41-CH_3-GRIS was attributed to the hydrophobic effect derived from methyl functionalization of TMCS on the surface [27]. At the end of 96 h, MCM-41-CH_3-GRIS released 60% of griseofulvin whereas for pure griseofulvin 88% was dissolved.

Encapsulation of griseofulvin in negatively charged MCM-41 resulted in faster release while positively charged MCM-41-NH_2 leads to relatively slower release. The faster release from MCM-41-GRIS could be attributed to the presence of griseofulvin as nano-sized aggregates in the pore channels of MCM-41 [18,48]. The comparative slower release of griseofulvin from MCM-41-NH_2-GRIS could be attributed to the APTES grafting on the surface which may impart relatively slight hydrophobicity owing to the aminopropyl chain of APTES compared to MCM-41 leading to slower influx of dissolution media in the pore channels which would eventually delay the dissolution of griseofulvin. Also, APTES grafting would impart some steric hindrance inhibiting the release of griseofulvin from the pore channels [49]. Moreover, the positively charged amino groups may interact with negatively charged carbonyl groups, resulting in slower release from MCM-41-NH_2 compared to MCM-41. This finding is in accordance

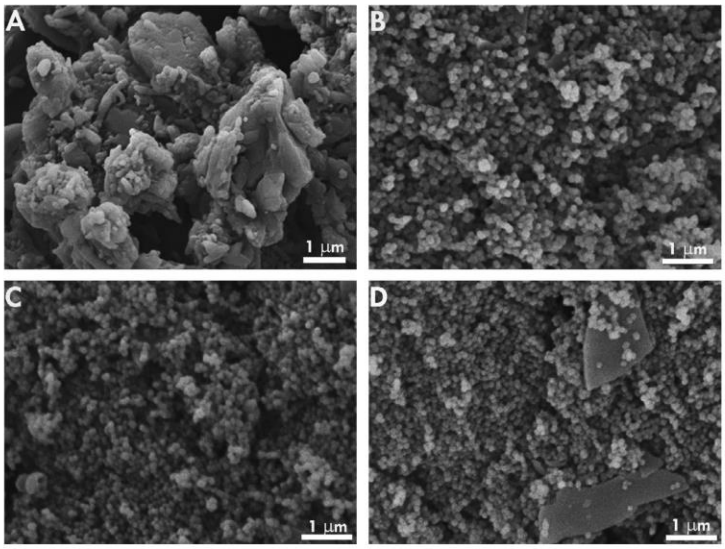

Fig. 8. SEM images of pure griseofulvin (A), MCM-41 (B), MCM-41-GRIS (C) and MCM-41-GRIS PM (D).

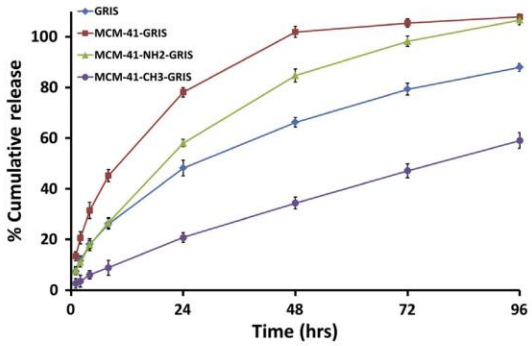

Fig. 9. *In vitro* release of pure griseofulvin and griseofulvin loaded in MCM-41-GRIS, MCM-41-NH_2-GRIS and MCM-41-CH_3-GRIS materials in 0.5% SLS.

with an earlier report using emodin as the drug molecule [50]. Thus, the surface charge clearly demonstrates its role in modulating the drug release.

Hydrophobic modification of MCM-41 using methyl group results in poor influx of dissolution media in the pore channels leading to very slow dissolution of drug resulting in its slow release [27] which is also supported by the TGA curves in Figs. 6A and 7A. The presence of hydrophobic methyl groups reduces interaction of encapsulated griseofulvin with the aqueous media. On the other hand, the hydrophilic MCM-41 results in faster drug release of almost 2 order due to the easier influx of dissolution media in pore channels. Thus, hydrophobicity of MCM-41 materials controls the drug release can be attributed to the wetting effect with dissolution media. The enhanced release of griseofulvin from MCM-41-GRIS could be attributed to the presence of nano-sized aggregates of griseofulvin and absence of steric hindrance or hydrophobic moiety on its surface. The surface modified MSNs were prepared with similar pore size to avoid the pore size effect in drug release and solubility studies and it was found that, the surface charge and hydrophobicity plays a critical role in controlling griseofulvin's release from MSNs.

The effect of *in vitro* release on MSNs particle size was studied by measuring their size using DLS. It was observed that the particle size of MSNs was slightly altered after *in vitro* release studies wherein particle size of MCM-41 (190 nm, PDI = 0.182), MCM-41-NH_2 (190 nm, PDI = 0.165) and MCM-41-CH_3 (190 nm, PDI = 0.223) changed to 190, 220 and 220 nm with PDI of 0.179, 0.198 and 0.232 respectively (Fig. 10).

Griseofulvin solubility was determined by preparing saturated solution of GRIS, MCM-41-GRIS, MCM-41-NH_2-GRIS and MCM-41-CH_3-GRIS in water to reach equilibrium concentration. Griseofulvin solubility was increased approximately 3 folds in MCM-41-GRIS (62.3 μg mL^{-1}) compared to GRIS (21.5 μg mL^{-1}, Fig. 11) which is in accordance with previous studies using Indole-3-butyric acid and curcumin loaded in MCM-41 [18,20]. The enhanced solubility of griseofulvin in MCM-41-GRIS is attributed to its encapsulation in nanopores based on Ostwald–Freundlich equation where solubility enhancement is related to particle size [7]. The solubility was enhanced approximately 2 folds for MCM-41-NH_2-GRIS (39.8 μg mL^{-1}) compared to GRIS. The relatively low solubility of griseofulvin in MCM-41-NH_2-GRIS compared to MCM-41-GRIS could be attributed to the steric hindrance offered by the aminopropyl group grafted on its surface inhibiting the release of GRIS from the pore channels leading to comparatively decreased solubility [49]. However, the solubility of MCM-41-NH_2-GRIS is higher compared to pure GRIS as GRIS is a

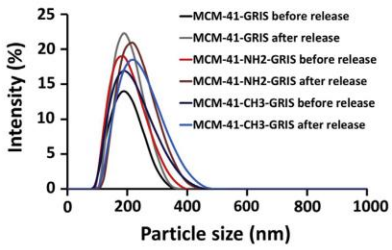

Fig. 10. Effect of *in vitro* dissolution on particle size of MCM-41-GRIS, MCM-41-NH_2-GRIS and MCM-41-CH_3-GRIS materials before and after release.

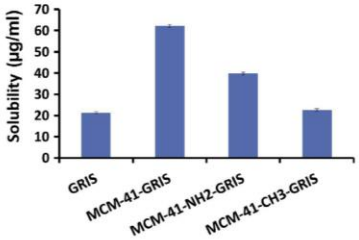

Fig. 11. Saturated aqueous solubility of pure griseofulvin and griseofulvin encapsulated in MCM-41-GRIS, MCM-41-NH_2-GRIS and MCM-41-CH_3-GRIS samples.

hydrophobic drug with low solubility and is present in crystalline state whereas for MCM-41-GRIS, MCM-41-NH_2-GRIS and MCM-41-CH_3-GRIS, GRIS is present in amorphous state as observed from Figs. 2B, 5 and 6B. Hydrophobic MCM-41-CH_3-GRIS (22.6 µg mL^{-1}) displayed solubility similar to that of pure griseofulvin due to the methyl groups present on its surface leading to poor wetting of silica material and hence very slow influx of solvent in pore channels leading to low solubility. Thus, the surface functionalization in the form of surface charge and hydrophobicity leads to variation in the solubility profile of griseofulvin.

4. Conclusion

MSNs were synthesized with different surface charge and hydrophobicity while retaining similar particle and pore size to study their influence on solubility and *in vitro* release of encapsulated griseofulvin. It was found that hydrophilic nanoparticles (MCM-41 and MCM-41-NH_2) enhanced the solubility and drug release compared to hydrophobic nanoparticles (MCM-41-CH_3) owing to their better wetting capability. Within hydrophilic nanoparticles, negatively charged particles (MCM-41) demonstrated 1.5 times higher solubility compared to positively charged nanoparticles (MCM-41-NH_2). Thus, both the solubility and release of griseofulvin can be modulated by carefully selecting the surface functionalization on MSNs. The findings from this study may provide new insight on rationally designed MSNs for applications in drug delivery.

Acknowledgments

We acknowledge the support from the Australian Research Council, the Australian National Fabrication Facility and the Australian Microscopy and Microanalysis Research Facility at the Centre for Microscopy and Microanalysis, The University of Queensland, Australia. We thank Ms Ying Yu from Centre of Microscopy and Microanalysis, The University of Queensland for SEM images.

References

[1] C. Lipinski, Am. Pharm. Rev. 5 (2002) 82–85.
[2] R.C. Nagarwal et al., Curr. Drug Delivery 8 (2011) 398–406.
[3] E.D. Gamsiz et al., Ann. Biomed. Eng. 39 (2011) 455–468.
[4] S. Muela et al., Int. J. Pharm. 384 (2010) 93–99.
[5] C.-M. Hsu et al., Carbohyd. Polym. 98 (2013) 1422–1429.
[6] J.M. Pereira et al., Mol. Pharmacol. 10 (2013) 4640–4653.
[7] W. Ostwald, Z Phys. Che-Stoch Ve 34 (1900) 495–503.
[8] P. Couvreur et al., Eur. J. Pharm. Biopharm. 41 (1995) 2–13.
[9] R.S. Mulik et al., Int. J. Pharm. 398 (2010) 190–203.
[10] C. Oussoren et al., Adv. Drug Deliver Rev. 50 (2001) 143–156.
[11] C.T. Kresge et al., Nature 359 (1992) 710–712.
[12] D.Y. Zhao et al., J. Am. Chem. Soc. 120 (1998) 6024–6036.
[13] A. Szegedi et al., J. Solid State Chem. 184 (2011) 1201–1207.
[14] M. Vallet-Regi et al., Chem. Mat. 13 (2001) 308–311.
[15] J. He et al., RSC Adv. 4 (2014) 13304–13312.
[16] B. Karimi et al., RSC Adv. 4 (2014) 4387–4394.
[17] J.L. Gu et al., J. Colloid Interface Sci. 407 (2013) 236–242.
[18] S. Jambhrunkar et al., RSC Adv. 4 (2014) 709–712.
[19] H. Al-Obaidi et al., AAPS Pharmscitech 10 (2009) 1172–1177.
[20] V. Ambrogi et al., Microporous Mesoporous Mater 96 (2006) 177–183.
[21] S. Jambhrunkar et al., J. Am. Chem. Soc. 135 (2013) 8444–8447.
[22] A. Szegedi et al., J. Solid State Chem 194 (2012) 257–263.
[23] J. Lu et al., Nanomedicine: NBM 8 (2012) 212–220.
[24] N.H.N. Kamarudin et al., Micropor. Mesopor. Mat. 180 (2013) 235–241.
[25] M. Xie et al., Colloid Surface B 110 (2013) 138–147.
[26] A. Wani et al., Pharm. Res. 29 (2012) 2407–2418.
[27] Q.L. Tang et al., J. Control Release 114 (2006) 41–46.
[28] N. Aggarwal et al., Int. J. Pharm. 437 (2012) 277–287.
[29] H. Al-Obaidi et al., Int. J. Pharm. 443 (2013) 95–102.
[30] M.D. Veiga et al., J. Pharm. Sci. 87 (1998) 891–900.
[31] N. Aggarwal et al., Colloid Surf. B 105 (2013) 158–166.
[32] S. Hbaieb et al., Int. J. Pharm. 439 (2012) 234–245.
[33] S. Yang et al., J. Am. Chem. Soc. 128 (2006) 10460–10466.
[34] J. Lu et al., Small 3 (2007) 1341–1346.
[35] J. Kecht et al., Chem. Mater. 20 (2008) 7207–7214.
[36] X.S. Zhao et al., J. Phys. Chem. B 102 (1998) 1556–1561.
[37] Y. Chen et al., Molecules 17 (2012) 5972–5987.
[38] J.F. Shao et al., Acta Biochem. Biophys. Sin. 43 (2011) 267–274.
[39] J. Yang et al., J. Mater. Chem. 21 (2011) 2489–2494.
[40] C.M. Yang et al., Chem. Mater. 15 (2003) 275–280.
[41] M.R. Mello et al., Microporous Mesoporous Mater 143 (2011) 174–179.
[42] D.H. Park et al., Ind. Eng. Chem. Res. 40 (2001) 6105–6110.
[43] D.H. Pan et al., J. Mater. Res. 26 (2011) 804–814.
[44] A. Nieto et al., Microporous Mesoporous Mater 116 (2008) 4–13.
[45] P. Punyacharoennon et al., J. Appl. Polym. Sci. 110 (2008) 3336–3347.
[46] J. Yang et al., Vib. Spectrosc. 50 (2009) 178–184.
[47] T. Limnell et al., J. Pharm. Sci. 100 (2011) 3294–3306.
[48] M. Vialpando et al., J. Pharm. Sci. 100 (2011) 3411–3420.
[49] P.K. Jal et al., Talanta 62 (2004) 1005–1028.
[50] Y. Xu et al., Appl. Surf. Sci. 258 (2012) 6366–6372.

Chapter 8

Conclusions and Future Directions

8.1 Conclusions

Hydrophobic drugs pose a major disadvantage of low aqueous solubility which lowers its bioavailability and delays their clinical applications. Hence, enhancing the solubility of such hydrophobic drugs is of great importance. Reducing the drug particle size to nanoscale is the preferred approach to enhance the solubility. However, with the existing strategies, it is difficult to reduce the drug particle size below 20 nm, a regime where drastic increase in the solubility is expected based on Ostwald-Freundlich equation. Mesoporous Silica Nanoparticles (MSNs) have been looked at to provide solution in solubility enhancement. However, one needs to control the pore size of MSNs precisely at angstrom scale so that they can find an optimized pore size for a given drug molecule which would display highest solubility.

The first major contribution of this work is successful development of a novel Vacuum-assisted Vapour Deposition (VVD) method to control the pore size of MSNs at angstrom scale. The pore size was controlled in the range of 2 – 4 Å and 4 – 6 Å using tetraethoxyorthosilicate and tetramethoxyorthosilicate as silica precursors respectively. The advantage of VVD method is that, it can control the pore size of MSNs in a stepwise manner with the same angstrom precision. This fine pore size control was not achievable with earlier methods reported in the literature. The series of pore size reduced MSNs were characterised using X-ray diffraction (XRD), Nitrogen adsorption/desorption isotherms and Fourier Transformed Infrared Spectroscopy (FTIR) to evaluate its structural characteristics after conducting VVD process for 3 cycles. It was found that, the ordered structure of MSNs is retained even after 3 VVD cycles demonstrating the advantage of this novel method. A pore size – solubility correlation was established by encapsulating a hydrophobic anticancer drug, Curcumin in the series of pore size reduced MSNs. An optimized pore size was found out which displayed highest solubility. This novel VVD method provides a general strategy to find an optimized pore size for a given drug molecule which would help in enhancing their solubility.

Effective cancer treatment requires the anticancer drug to reach its target and kill the cancer cells. However, the anticancer drugs are hydrophobic with low aqueous solubility and hence we need to increase the drug solubility. Also, we need an appropriate drug carrier system to deliver the anticancer drug to its target. The second major contribution of this work is to enhance the cytotoxicity of curcumin by encapsulating it in MSN. Curcumin was encapsulated in MSNs which helped in increasing the solubility, drug release and cytotoxicity compared to the pure drug. The cytotoxicity studies were performed in skin cancer cell line, SCC-25 as cancer model. It was clearly demonstrated that the curcumin encapsulated MSNs enhanced the cytotoxicity compared to the pure drug. Thus, MSNs performed dual role of enhancing the drug solubility and as drug carrier system to cancer cells.

Among the several properties of MSNs, ease of surface functionalization is one of the most important criteria which have enticed researchers for its diverse applications. More specifically, it plays a vital role in the field of pharmaceutical drug delivery to enhance the properties such as cellular uptake, targetability and stimuli responsive drug release to name a few by encapsulating drug molecules in MSNs. However, the effect of surface functionalization needs to be carefully studied to identify if it significantly enhances the applicability. The third major contribution of this work is to investigating the influence of surface functionalization on drug solubility, drug release and cytotoxicity. Effect of surface charge and hydrophobicity was studied by comparing MSNs with positive charge (hydrophilic nature), negative charge (hydrophilic nature) and negative charge (hydrophobic nature) using two model hydrophobic drug molecules – Curcumin and Griseofulvin. It was found that the negatively charged hydrophilic MSNs improved the drug solubility and drug release for both the drugs compared to the others. Hydrophobic MSNs displayed the slowest drug release profile. Cytotoxicity studies conducted using MTT assay showed that negatively and positively charged MSNs both had similar cytotoxicity. On further investigation performed using cell cycle analysis and cell apoptosis, it was observed that, the negatively charged (hydrophilic nature) MSNs show slightly better performance compared to the positively charged (hydrophilic nature). Thus, the general understanding of designing positively charged drug carrier system does not hold true and it should be treated on a case-by-case basis.

8.2 Recommendations

In recent years, a lot of attention is given to modify and design the applicability of MSNs especially in drug delivery. The field of drug delivery faces critical issues of enhancing solubility of

hydrophobic drugs and designing an ideal carrier system which can reach its target site. This thesis focuses on the efficiency of inorganic MSNs to resolve these issues. We have demonstrated the potential of MSNs to enhance solubility and cytotoxicity of the anticancer drug. However, there are few aspects which further need to be explored.

In this thesis we determined an optimized MSN pore size for curcumin as drug molecule. The VVD process should be applied to few other hydrophobic drug molecules to showcase its advantage and making it a more general approach to enhance solubility.

Apart from anticancer drug molecules, biomolecules such as siRNA are reported to be more effective in treating cancers. Based on the VVD process, an optimized MSN pore size should be determined for a given biomolecules and its efficiency needs to be evaluated. This would further expand the applicability of MSNs.

The cytotoxicity enhancement study demonstrated negatively charged MSNs to show slightly better cytotoxicity compared to positively charged MSNs. However, this study was performed using SCC-25 cancer cell line. It is recommended to perform *in-vivo* experiments using mice as animal model. The pharmacokinetics study should be conducted to evaluate the performance of both positively and negatively charged MSNs compared to pure drug. Also, tumor inhibition efficacy of anticancer drug encapsulated MSNs should be tested on mice models by comparing it with pure drug or commercial product.

In order to prove the completeness of the study, it would be highly recommended if the anticancer drug encapsulated MSNs can be formulated as a tablet or capsule dosage form.

In summary, we successfully developed VVD method for controlling the MSN pore size at angstrom scale and demonstrated its application for solubility enhancement. Further we studied the influence of surface functionalization and have some important findings which would give new approach in designing carrier systems. This work could be of interest for vast audience of chemists and material scientists in various fields of catalysis, nanomedicine and biomedical engineering.